UNIVERSITY OF OSLO
Department of informatics

Single- and dual-axis lateral capacitive accelerometers based on CMOS-MEMS technology

Master thesis

Jia Yu Chen

April 30, 2010

Abstract

In order to have a compatible device in a sensor node in wireless sensor network, the sensors have to be made in micro-size, low cost, low power consumption and high performance. By using CMOS-MEMS technology, the micro sensors can be implemented with promising results.

One of the central micro inertial sensors is an accelerometer which has the capability of sensing position change, vibration and shock of a device. A single-axis lateral capacitive accelerometer and a dual-axis in-plane capacitive accelerometer are made in this thesis. An alternative design of the single-axis accelerometer is discussed. The system designs are made through mathematical analysis in MatLab, 3D FEM simulation in CoventorWare and final layout in Cadence. The main issue is making compliant springs, large proof mass, considerable number of comb fingers, for fabricating micro sensors with high sensitivity and good noise performance.

The single-axis lateral capacitive accelerometer has sensor sensitivity of 9.3mV/G, mechanical noise floor of 19 $\mu G/\sqrt{Hz}$, linear measuring range of $\pm$26G. The dual-axis in-plane capacitive accelerometer has sensor sensitivity of 9.3mV/G in one direction and 11.1mV/G in the cross direction.

The chip is fabricated in a 0.25μm BiCMOS process from STMicroelectronics. The post process is done at Carnegie Mellon University (CMU), USA and SINTEF MiNaLab, Norway.

Acknowledgements

Thanks to my supervisor Oddvar Søråsen, for his many inspirations, patient guidance and encouragement.

Thanks to my wife and parents, for their ceaseless love and support.

Thanks to my friends, for their company and support through the time of my study at University of Oslo, especially Fan Zhang, for his suggestion and revision of my thesis.

Lastly, a grateful heart to my Lord, without blessing and help from him, I could not have been persisting to the present.

"In him we have redemption through his blood, the forgiveness of sins, in accordance with the riches of God's grace that he lavished on us with all wisdom and understanding."

Ephesians 1:7-8

Contents

Chapter 1

Introduction

1.1 MEMS technology

MEMS stand for Micro-Electro-Mechanical Systems. In Europe, it is also called Micro Systems Technology (MST). In a nutshell, MEMS means that very small systems can be built with components operating both electronically and mechanically. The systems are usually made at micro scale, with even decreasing feature sizes. Nanoelectromechanical systems (NEMS) can be the next miniaturization step from MEMS devices. Figure 1.1 shows a MEMS gear-train comparing to a spider mite.

The first idea about micro systems was presented by Richard Feynman at his famous lecture "There's Plenty of Room at the Bottom" in 1959. The MEMS technology is in rapid development and has expanded into many fields in the last decades. The MEMS concept is not just mechanical at present; it has grown to encompass many other types of small units, including thermal, magnetic, fluidic, and optical devices and systems [1]. Today MEMS is applied in automotive industry, oil industry, navigation, biomedical devices, optics, computer industry and wireless communication (e.g. WSN described in section 1.3) etc. Pressure sensors, accelerometers, displays, optical switches and microphones are examples of MEMS devices which have been made to date. The manufacturing method to make MEMS is referred to as micromachining process that will be presented in section 2.1.

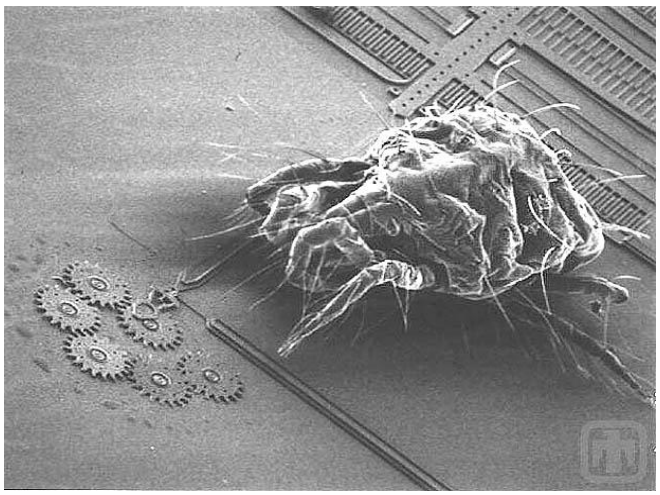

Figure 1.1: SEM image of a spider mite on a polysilicon MEMS gear-train [2]

1.2 Combination of CMOS & MEMS

MEMS technology can primarily be used to realize two types of units: sensors and actuators. The sensors, usually in micro size, can be of many different types, e.g. for detection of physical phenomena such as vibration or any other kind of motion, sound, temperature, pressure etc. They have capability of transforming these physical phenomena to electrical signals. Pressure sensors, accelerometers and gyroscopes are typical examples of MEMS sensors. Several micro sensors and accelerometers based on CMOS-MEMS technologies (typical processing methods to combine CMOS & MEMS) are presented in chapter 2. More details about CMOS-MEMS technologies can also be found in chapter 2.

The actuators are movable mechanical structures which can be implemented with different physical mechanisms and can also be controlled by electrical circuits (IC). The actuation can influence the micro system itself or the environment around it. Micro motors, varactors, micro mirrors and switches are examples of MEMS actuators.

MEMS are the "connection bridge" between electrical circuits and the real world. In an integrated micro system with both MEMS and ICs, the mechanical systems are the "eyes, ears and hands" for contacting the environment, and the microelectronic circuit is the "brain" which controls and enhances the functionality of the MEMS components. Monolithic integration of MEMS with electronics can primarily be motivated by the following four points, as Gary K. Fedder from Carnegie Mellon University has presented in [3].

1. Lowering manufacturing cost by batch processing.
2. Solving interconnect bottlenecks by performing on-chip signal processing to perform data reduction.
3. Miniaturizing total systems is important for many applications in the future.
4. Improving performance through reduction and repeatability of the capacitive parasitic.

Due to the benefits presented above, small size, multi-function and low cost are the ultimate goals of commodity MEMS devices. One way of making combined systems is to implement the mechanical parts in an ordinary CMOS process together with traditional electronics [4]. In fact, the crossover of the conventional IC industry and the fast-growing MEMS technology has led to many newborn technologies in the past years [5]. The new technologies give wider design space to make integrated systems based on CMOS circuits and MEMS components. Today, the primary technologies (processing approaches) to achieve the integration of MEMS with electronics are pre-, intermediate/mixed- and post-CMOS MEMS processes. These approaches will be presented in detail in chapter 2.

1.3 CMOS-MEMS sensor nodes in wireless sensor network

A wireless sensor network (WSN) consists of densely distributed nodes linked by self-organized wireless communication systems [6]. A typical WSN architecture is shown in figure 1.2. Each sensor node may transfer data to its neighboring nodes through wireless communication. The sensor nodes also have the capability to process data locally. The processed data is transferred to the base station/the users. These sensor nodes are used in many application areas, such as environment monitoring, object tracking, process control, home automation, and facilities for oil/gas production etc.

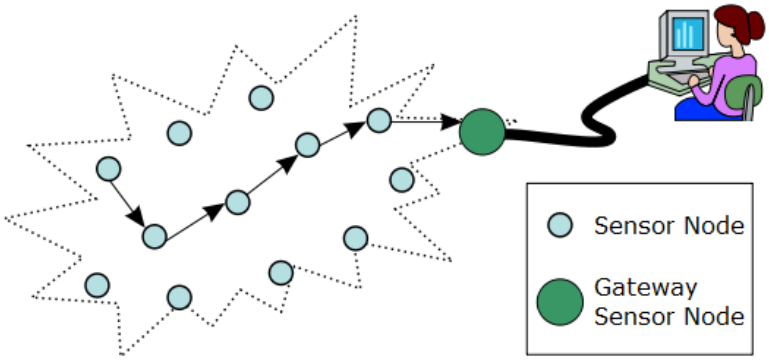

Figure 1.2: Typical multihop wireless sensor network architecture [7]

A sensor node in WSN is typically equipped with one or more application-specific sensors, a microcontroller (e.g. CPU), a radio transceiver or other kinds of wireless communication devices and a limited energy source with limited capacity (e.g. battery). A typical architecture in a sensor node is shown in figure 1.3.

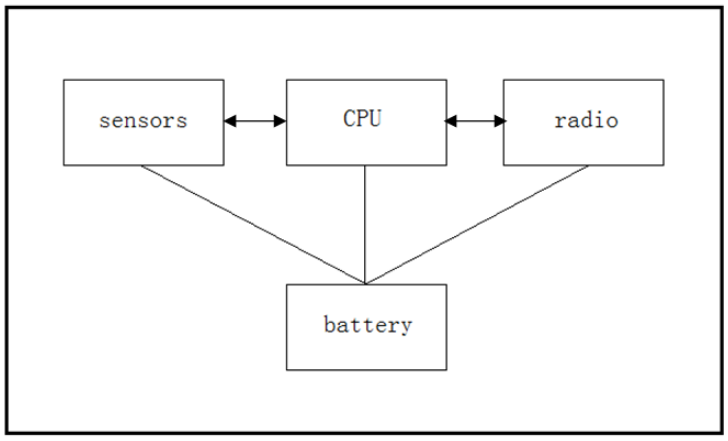

Figure 1.3: Sensor node's internal architecture

The sensors are usually implemented in MEMS for detection of physical phenomena. The microcontroller has the capability to handle data which are collected by the sensors or received from the radio, and it is able to send out processed signals through the radio

transceiver. All these three main components are powered by a limited battery capacity. For example, if the sensor nodes are exploited to measure the air humidity deep in the desert, there is no large power supply available for the nodes. In most settings, the network must operate for long periods of time and the nodes are wireless, so the available energy resources—whether batteries, energy harvesting units, or both—limit their overall operation [8]. Therefore, low power consumption for the sensor nodes is especially important due to limited energy availability. Besides, small size and low cost of the sensor nodes are also required, and hence the individual devices in a wireless sensor network (WSN) are inherently resource constrained: They have limited processing speed, storage capacity, and communication bandwidth [9].

In the project above this thesis, a specific, compact micro-sensor has to be designed for the sensor node which is used in a commercial T-motes network [40]. The sensor is based on MEMS and controlled by a CMOS circuit. The combination of MEMS and CMOS is a new and promising technique which makes possible that the micromechanical and electrical systems can be integrated on the same chip (SoC). In order to be adapted in the sensor nodes in WSN, the main challenges for such systems are miniaturization ("smart dust" [41]) and low power consumption.

1.4 Purpose of the design

The Nanoelectronics group at University of Oslo (UoO) has succeeded in integrating MEMS and CMOS circuitry with good results [4]. Several approaches of combining MEMS and CMOS technologies will be presented in this theis. By cooperation with Carnegie Mellon University (CMU) in USA and SINTEF Mikronanoteknologilab (MiNaLab), post processing of CMOS circuits is performed. Some circuits have been designed and fabricated by using CMOS-MEMS technology at UoO [10].

This thesis will start with discussing which types of micro sensors can be realized by using CMOS-MEMS technique. As it will be presented in chapter 2, one of the central micro sensors is an accelerometer. Accelerometers are already applied in many areas such as for air bags in cars, navigation (e.g. GPS), consumer electronics (e.g. iPhone) etc. Accelerometers can be made in many different ways. One of the common ways is capacitive accelerometer which can give high sensitivity. In this thesis, a single-axis lateral capacitive accelerometer (design A) is designed with high sensitivity, and an alternative design of capacitive accelerometer (design B) is discussed. A dual-axis in-plane capacitive accelerometer is also designed by integrating two single-axis accelerometers in cross directions.

The design of the accelerometers includes mathematical modeling in MatLab, simulation and analysis using CoventorWare, and the layout of structures in Cadence. The designed chip is fabricated in a $0.25\,\mu$m CMOS/BiCMOS process from STMicroelectronics through the broker service Circuit Multi Projet (CMP), France. Post processing is done at Carnegie Mellon University.

1.5 Thesis disposition

- **Chapter 2: CMOS & MEMS technologies used for monolithic integrated systems** – The basic concept of micromachining and the primary processing approaches in integrating CMOS and MEMS are illustrated. Several CMOS-MEMS processes and the chosen process to make accelerometers in this thesis are explained. In the end of the chapter, a self-made CMOS-MEMS design flow is illustrated.
- **Chapter 3: Design of the integrated accelerometers –** Different mechanisms used for the MEMS accelerometers and theirs applications are presented. The operating principle of a single-axis capacitive accelerometer is illustrated followed by a short overview of the systems.
- **Chapter 4: Mechanical structures, design and modeling –** One of the most important mechanical components is the springs within a capacitive accelerometer. The spring design is emphasized in this chapter. Spring constant for the springs is analyzed by both mathematical and simulation models. The mechanical sensitivity for the single-axis lateral capacitive accelerometer is found and some important factors such as mechanical noise, damping and Q-factor are discussed. Lateral and out-of-plane curl due to CMOS-MEMS process is explained in the end of this chapter.
- **Chapter 5: Capacitive sensing and self-test actuator, design and modeling –** Full differential topology is applied in the accelerometers that will be presented. An equation for calculating the sensor sensitivity of a capacitive accelerometer is obtained. Comb fingers design is the centre part in this chapter. Mathematical and simulation models are made to analyze the sensing and parasitic capacitances in the accelerometer. The capacitive actuation is explained and a self-test actuator is made. The layout of the single-axis lateral capacitive accelerometer can be found in the end of this chapter.
- **Chapter 6: Alternative design of a single-axis lateral capacitive accelerometer –** Another capacitive accelerometer design (design B) based on modification of the previous accelerometer (design A) is analyzed and compared to the equivalent design from NTHU. The conclusion is made in this chapter.
- **Chapter 7: Dual-axis in-plane capacitive accelerometer –** The design based on integrating two single-axis lateral capacitive accelerometers is presented. The analysis of the critical factors in the design is made and the layout of the system can be found.
- **Chapter 8: Summary and discussion –** A short summary is made with achieved results followed by comparison with the other works. Proposed improvements of the systems in this thesis are suggested.
- **Chapter 9: Conclusion –** The work of the thesis is concluded with possible work in future.

Chapter 2

CMOS & MEMS technologies used for monolithic integrated systems

2.1 Micromachining

The process of making micromechanical structures is called micromachining. Traditional MEMS processes have roots in IC manufacturing. The MEMS technology is in rapid development and many different fabrication approaches have been developed to date. Typically, the MEMS processes are divided into surface micromachining and bulk micromachining.

Surface micromachining is to deposit different layers (structural and sacrificial layers) on a substrate wafer and etch away the sacrificial layers to release the structures. This process is similar to IC fabrication, expect for the sacrificial layers. Surface micromachining can make thin and small structures. In combination with CMOS processes, it can be used for making mechanical and electrical systems on a same chip.

Defining structures by selectively etching the substrate wafer, is bulk micromachining. This processing method is able to make thick and large structure that is useful to make a large mass. A heavy mass is beneficial in accelerometers for the reason of increasing sensitivity and accuracy of the devices. This is described in chapter 3.

The etching processes within bulk machining consist of wet etching and dry etching. Wet etching is done by using different etchants to remove the unwanted materials. This etching method includes both isotropic (uniform etching in all directions) and anisotropic (stronger etching in one direction than the others). The sidewall shape of the structures after anisotropic etching is dependent on the crystal orientation of the silicon crystal. Both isotropic and anisotropic etchings are available for the dry etching. There are many kinds of dry etch methods, such as plasma, ion milling and vapor-phase etching etc. Figure 2.1 shows the different etching methods.

One of the dry etching methods is reactive ion etch (RIE) which is the primary etching process used to form the structures used in this thesis. The processing approach used for making accelerometer in this thesis, is based on several dry etching steps for post-processing CMOS chips. More details are covered in section 2.3.

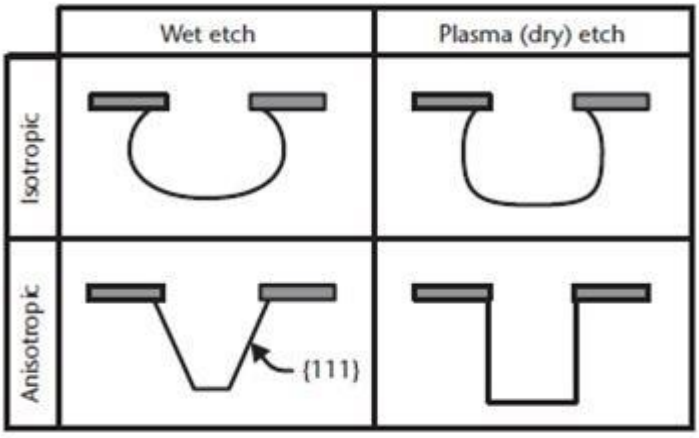

Figure 2.1: Schematic illustration of cross-sectional trench profiles resulting from four different types of etching methods. [11]

2.2 Integrating CMOS and MEMS

In order to integrate MEMS and electronic circuits on the same chip, one must combine the micromachining process and CMOS technology. There are many different ways to accomplish this integration as mentioned in chapter 1. The primary processing methods today are pre-, intermediate/mixed- and post-CMOS. Each method has its own benefits and drawbacks. Depending on the chosen integration method, a number of fabrication constraints are imposed on the micromachining steps in order not to deteriorate the performance of the CMOS electronics [12]. Generally, the micromachining and CMOS processes have to be modified in order to be compatible with each other.

2.2.1 Pre-CMOS

Pre-CMOS micromachining is often designated as a MEMS-first process. After the micromechanical structures are accomplished, the CMOS process is run to form the electrical circuits. This fabrication approach allows us to optimize the MEMS structures for the integration, since the micromachining steps need high temperature for annealing in order to reduce residual stress in the mechanical structures. The annealing temperature is normally higher than 900℃ which is not allowed in CMOS process. A passivation step is needed after micromachining process. The main challenges include planarization before the CMOS process because of the large topography variations after MEMS processing, and methods for making the interconnections between MEMS and circuitry areas. Pre-CMOS process also has another problem to be solved, and that is unwanted contaminants remained after MEMS process. CMOS foundry processes require clean silicon wafers. Some of these problems can be solved by building the MEMS structures in a trench, which has been etched into the bulk silicon using an

anisotropic wet silicon etchant, as it is shown in figure 2.2. This is called M^3EMS (Modular, Monolithic MicroElectroMechanical Systems) technology which is developed at Sandia National Laboratories.

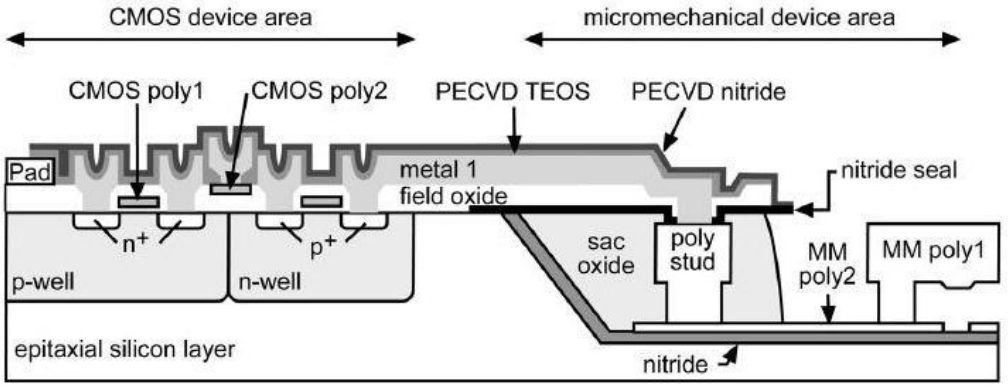

Figure 2.2: Schematic cross-section of pre-CMOS MEMS processes for fabrication of monolithically integrated polysilicon microstructures from SANDIA (M^3EMS) [13]

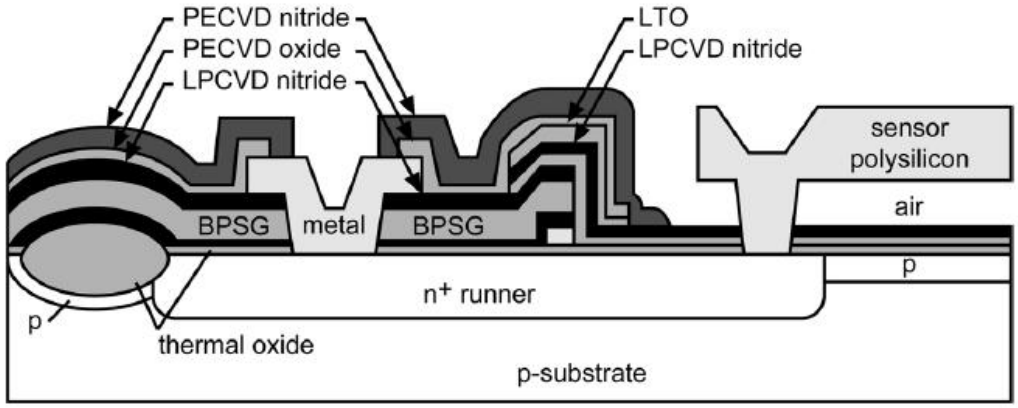

Figure 2.3: Schematic cross-section of Analog Devices' integrated MEMS technology with an n+-diffusion interconnects structure between polysilicon microstructure and on-chip electronics. [14]

2.2.2 Intermediate/mixed-CMOS

In this processing approach, the CMOS process is interrupted for running micromachining steps. Both MEMS and CMOS processes have to be adjusted for a successful integration. The MEMS process has limitations while the CMOS process has to be modified. This approach is most commonly used to integrate polysilicon microstructures in CMOS/BiCMOS process technologies. The polysilicon requires high temperature annealing which is dangerous for the electronics. The annealing temperature is typically limited to about 900℃ in order not to affect the doping profiles of the CMOS process [15]. Contamination caused by the processes between micromachining and normal CMOS steps is another problem and many passivations are needed. Due to the limitations in the pre- and inter-CMOS foundries, the overall cost of

MEMS devices is relatively high. An example of BiMOSII process from Analog Devices for fabrication of accelerometers is shown in figure 2.3.

2.2.3 Post-CMOS

In post-CMOS micromachining process, the CMOS circuits are completely made before the MEMS process. The most attractive benefit of this approach is that any kind of advanced or standard CMOS foundry can in principle be used; hence the planarization is not needed in this approach. But some of the micromachining steps need high temperature for annealing, which is dangerous for the CMOS circuits based on Al-metallization, as mentioned in section 2.2.1. Therefore, several MEMS steps have to be abandoned or modified. Some compromises must be done for one or both processes. Under MEMS process, the CMOS area needs special protection. However, this processing approach gives more design options and possibilities for realizing monolithic integrated systems to date.

There are basically two strategies to perform post-CMOS: the microstructures can be built on top of the CMOS substrate or can be made by machining the CMOS layers themselves. The first strategy with building the MEMS on top of CMOS substrate is done by using surface micromachining techniques described in section 2.1. The low temperature within MEMS process is especially important in this strategy. The examples as MICS process uses tungsten instead of aluminum as CMOS metal (tungsten can withstand higher temperature) and UoC Berkeley uses SiGe as MEMS structure material (SiGe has lower deposition temperature).

In the second approach, the microstructures are made of a multilayer with metal and dielectrics that can be released by machining the CMOS substrate wafer. Using a variety of CMOS compatible bulk and surface-micromachining techniques, e.g., pressure, inertial, flow, chemical, and infrared radiation sensors have been produced [15]. By far the majority of demonstrated devices rely on bulk micromachining processes, such as wet and dry anisotropic and isotropic etching [12]. This approach only allows us to use the CMOS layers to form microstructures according to the regular CMOS process. The disadvantage is that the build-in stress within the multi thin film layers causes curling of the microstructures which can reduce performance of the micro systems. More details about that feature and the specific solution for the accelerometers can be found in the end of chapter 4.

2.3 CMOS-MEMS processes

The post-CMOS micromachining based on the CMOS layers for making the MEMS is referred to as a CMOS-MEMS process. The micromachining steps start with regular CMOS foundry. Gary K. Fedder has presented several types of post-CMOS processing methods in his paper [3]. Some of them which are commonly used are illustrated in

following sections.

2.3.1 Several post processes using unchanged CMOS foundry

Sacrificial oxide etch

After CMOS process shown in figure 2.4(a), the microstructures are made with VIAs and sacrificial layers (silicon dioxide) between the metal layers. During post processing, the sacrificial layers are removed by dry etching (plasma etch) without a mask and the microstructures are released after post processing as figure 2.4(b) shows. More metal layers can be made to form the microstructures after CMOS process.

With this CMOS-MEMS process, thin film structures can be made. This CMOS-MEMS process has been use to construct micro actuators in measuring Young's modulus and it also can be used to make micro sensors and other MEMS components [36].

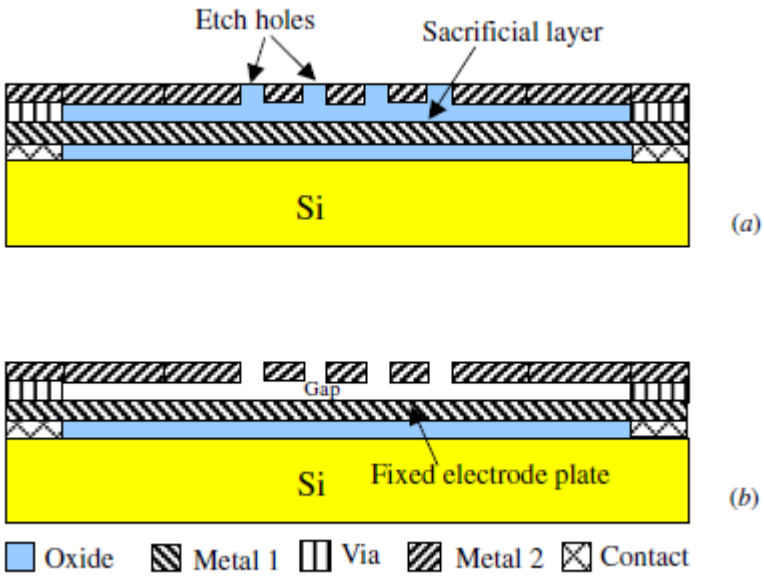

Figure 2.4: CMOS-MEMS process with sacrificial oxide etch
(a) after CMOS process; (b) after post process. [36]

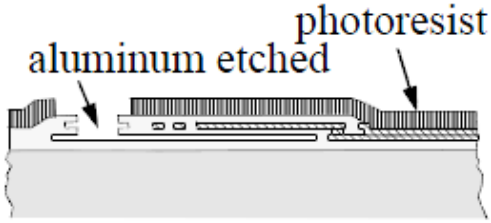

Figure 2.5: Released microstructure after sacrificial aluminum etching

Sacrificial aluminum etch

This micromachining technique is developed at ETH Zurich [37]. After the CMOS process, the selected metal layer (aluminum) is removed to release microstructures consisted of dielectric layers, metal layers and a passivation. The sacrificial aluminum layer is etched using standard wet etchants. Figure 2.5 shows the released microstructure after post CMOS processing with sacrificial aluminum etching.

This post CMOS process is used to release the membrane of vacuum sensor [38]. A post-process combining both sacrificial aluminum etching and bulk silicon micromachining can be used to release the microstructures of the fluid density sensors [39].

Maskless post-processing with one wet etch

After the CMOS process is completed, The CMOS wafer is remained with the microstructures which contain several metal layers with vias between them, a passivation on top and sacrificial silicon oxide layers, shown in figure 2.6 (a). The passivation layers are selective removed and the oxide layers are exposed. Under the post-CMOS process, the sacrificial layers are etched away by using silox vapox III etchant and the microstructures are released. The metal layers are used as an etch-resistant mask.

Using this processing method, RF switches and micro mirrors are manufactured successfully [42] [43].

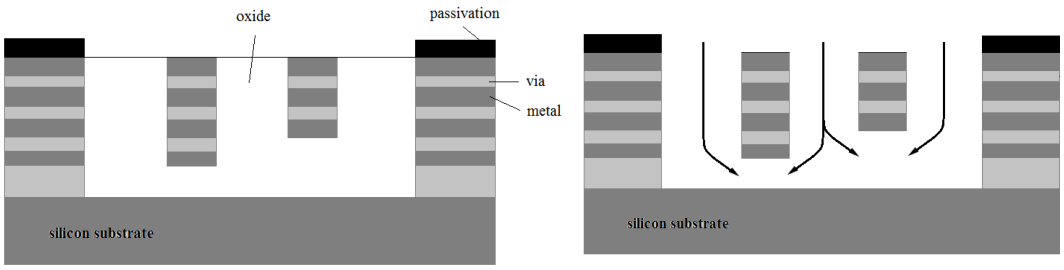

(a) (b)

Figure 2.6: Maskless post-processing using one wet etch: (a) after CMOS process; (b) etching oxide layers

2.3.2 Maskless post-processing with several dry etching steps

A surface micromachining technology from the front side of CMOS wafers using dry etching steps has been developed at Carnegie Mellon University (CMU) [16]. This high-aspect-ratio CMOS MEMS processing method is used for realizing the capacitive accelerometers in this thesis. After the CMOS circuits are made in a regular CMOS process, the post-CMOS MEMS process is performed by three etching steps illustrated in figure 2.7. The CMOS circuits are covered by top metal layer as an etch-resistant

mask, while the releasable MEMS structure holds a distance from the electronics following the MEMS design rules, as it is shown in figure 2.7 (a). The etching steps are the following:

1. The dielectric layers (silicon dioxide) are removed by an anisotropic CHF_3/O_2 reactive-ion etch (RIE) with the top metal layer as a mask. The sidewalls of microstructure are defined at this step. (Figure 2.4 b)
2. The exposed silicon substrate is etched by an anisotropic SF_6/O_2 DRIE. The sidewalls are extended down into the substrate (Figure 2.4c). In some design papers, this step is skipped [17] [18].
3. The silicon substrate is undercut by using an isotropic SF_6 RIE and the microstructure is released. (Figure 2.4d)

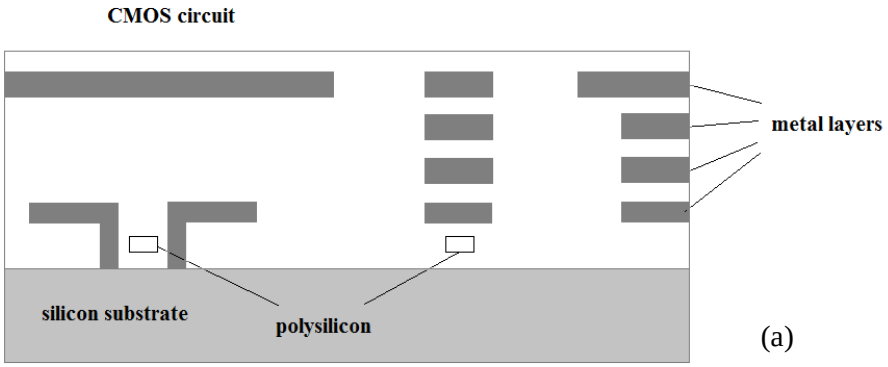

(a)

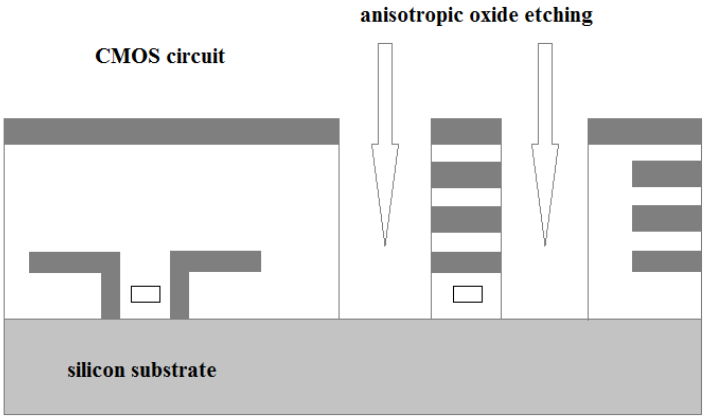

(b)

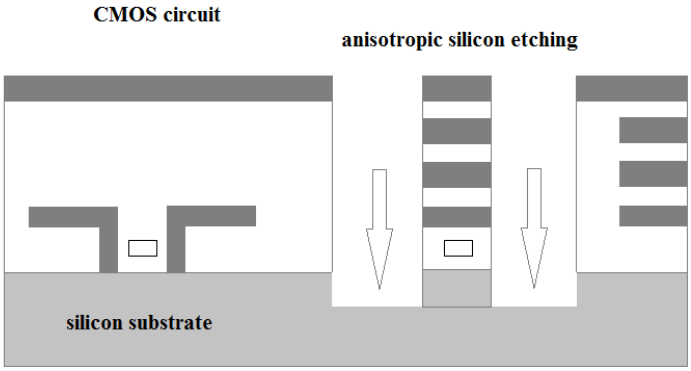

(c)

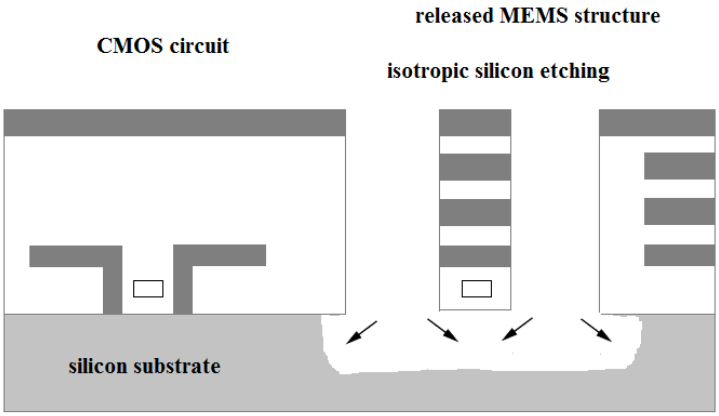

(d)

Figure 2.7: Procedure for maskless post-processing

The primary attributes of the process are the ability to make narrow beams and gaps, the use of the multi-level interconnect within the microstructures for routing sensor and actuator signals, and the proximity to electronics to minimize parasitic capacitances [3]. The main challenges of this processing approach include lateral curl caused by finite precision under the fabrication and vertical curl (out-of-plane) due to the thin film microstructures built up with the CMOS multilayer. These two drawbacks can reduce performance of the MEMS devices. More details on the lateral and out-of-plane curl and the specific solutions for the capacitive accelerometers are discussed in section 4.3.

The post-CMOS processing approach described above is also referred to as a frond side dry etching process with CMOS metal mask. Another post-CMOS processing approach is developed to overcome the drawbacks from the previous one, where a backside etch of the silicon substrate is performed in order to make thicker microstructures. A completed microstructure after post-CMOS processing with backside etch is shown in figure 2.8. More details on the procedure of this post processing approach can be found in [44], where a comb-drive resonator, a cantilever beam array and a z-axis accelerometer are fabricated using this post-CMOS processing approach. Making thicker microstructures is beneficial to a capacitive accelerometer with large mass and thicker comb fingers. However, this approach increases fabrication cost and complexity.

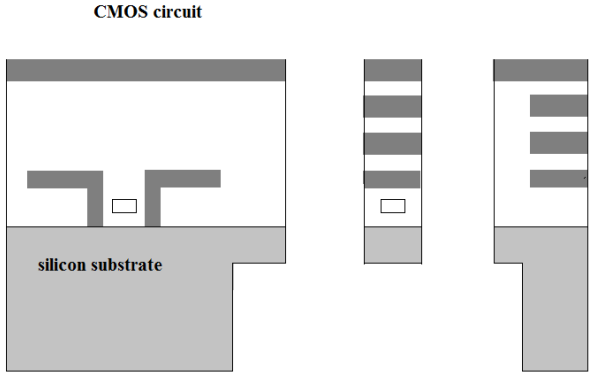

Figure 2.8: Microstructures after maskless post processing with backside etch

2.4 CMOS-MEMS design parameters used in this thesis

Table 2.1 shows material properties for all the metal layers using to construct the beams and the other mechanical components for the accelerometers in this thesis. In STM SiGe 0.25μm BiCMOS (BiCMOS7RF) process, there are also one metal layer (M5) and one dielectric layer (Via4) upon M4. M5 is made of Cu that is not used in the multilayer structures after the post processing design rules. The average Young's modulus E is ca. 116GPa and the estimated thickness is 4.8μm without the polysilicon layer. These design parameters listed are used in design of systems, both mathematical analysis and simulation models. STM 0.25 μm BiCMOS process is specifically defined in CoventorWare as it is shown in appendix A, where the multilayer structure is also shown.

The MEMS design rules were developed through the ASIMPS (Application-Specific Integrated MEMS Process Service) project at CMU. However, the structures must follow both the CMOS and MEMS design rules in order to be successfully fabricated. CMU also provides a set of ST7RF MEMS-specific design rules, which shows all restrictions for the CMOS compatible post processing, such as minimum gap, minimum and maximum structure width etc. All the design parameters this thesis are followed by this set of design rules.

Table 2.1: Material properties used for the simulation

Metal layers	Material	Young's modulus (GPa)	Thickness (μm)	Density ($kg/\mu m^3$)
Metal 4 (M4)	Alumium (Al)	77	0.6	$2.3 \cdot 10^{-15}$
Via 3 (M4-M3)	Silicon dioxide (SiO_2)	70	0.6	$2.15 \cdot 10^{-15}$
Metal 3 (M3)	Al	77	0.6	$2.3 \cdot 10^{-15}$
Via 2 (M3-M2)	SiO_2	70	0.6	$2.15 \cdot 10^{-15}$
Metal 2 (M2)	Al	77	0.6	$2.3 \cdot 10^{-15}$
Via 1 (M2-M1)	SiO_2	70	0.6	$2.15 \cdot 10^{-15}$
Metal 1 (M1)	Tungsten/Wolfram (W)	410	0.6	$1.93 \cdot 10^{-14}$
Via (M1-Poly)	SiO_2	70	0.6	$2.15 \cdot 10^{-15}$
PolySi	Polysilicon	160	0.6	$2.23 \cdot 10^{-15}$

2.5 The integrated CMOS-MEMS system design flow

In order to have a clear overview of the CMOS-MEMS system design, a home-made system design flow (for reference only) is shown in figure 2.9. This design flow is made

with the reference from [45].

First of all, the systems have to be specified. The most important specifications or the main goals are made before the project is started. The CMOS-MEMS system design is divided into two main branch lines, MEMS design and CMOS circuits design. In this thesis, the CMOS circuits are not made to the MEMS systems, and hence the right branch line and the top level analysis are ignored.

The MEMS design in this thesis is followed by behavioral component modeling in MatLab, 3D simulation models in CoventorWare, comprehensive analysis with the mathematical and simulation results and layout drawing in Cadence. The layout of MEMS structures is the final production in this project. The fabricated chip is measured and the measuring results are used to be compared with the simulation results, in order to improve the systems.

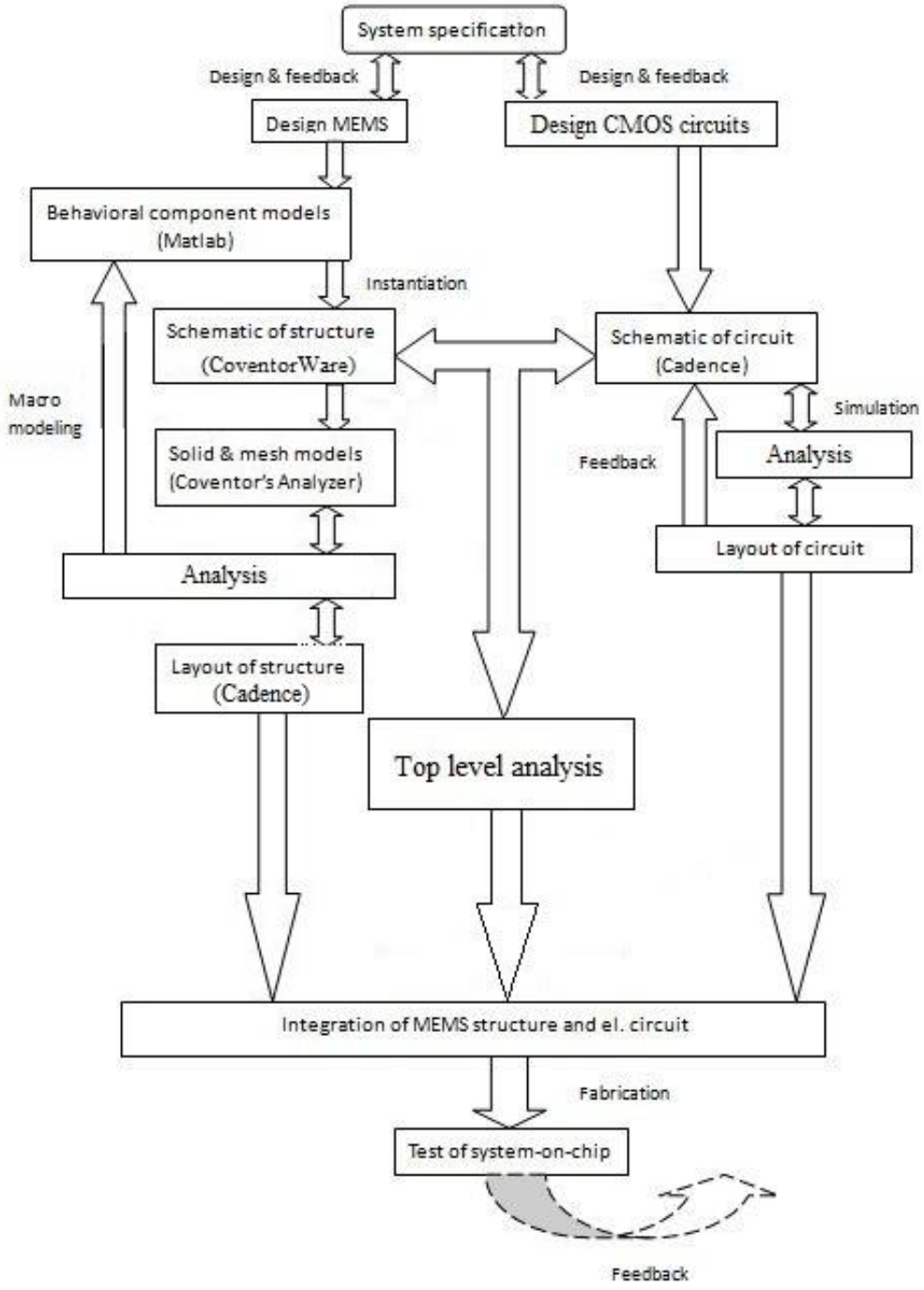

Figure 2.9: CMOS-MEMS system design flow

Chapter 3

Design of CMOS-MEMS accelerometers

A single-axis lateral capacitive accelerometer (design A) and a dual-axis accelerometer by integrating two single-axis accelerometers have been made. Alternative design of the single-axis lateral capacitive accelerometer (design B) based on modification of the design A is analyzed. MEMS accelerometers based on different sensing mechanisms and theirs applications are presented in this chapter. The operation principle of the single-axis capacitive accelerometer is explained and an overview of the systems in this thesis is given in the end of this chapter. The mechanical structures and the capacitive sensing are further discussed in the following chapters.

3.1 MEMS accelerometers

Accelerometers are the devices for measuring acceleration or force applied to the devices. The acceleration is often measured in G-force and 1G is 9.81m/s^2. Single- and multi-axis accelerometers have the capability of detecting accelerations in any directions, and can be used for sensing position change, vibration and shock of a device. The earliest commercial accelerometers based on MEMS technology are used in airbags in cars. Today, MEMS accelerometers are demonstrated as the most common inertial sensors in the fast growing market today, due to their small size, high sensitivity and low cost. They have been applied in engineering monitoring, medicine, navigation, transport and consumer electronics etc. Figure 3.1 shows the typical applications and performance requirements for accelerometers in these applications.

Many different sensing mechanisms can used for MEMS accelerometers, and piezoresistive sensing, piezoelectric sensing, capacitive sensing are the most commonly used.

Piezoresistive sensing is based on piezoresistors integrated on a cantilever beam or a spring. The acceleration causes the beam or the spring to bend, and thus the piezoresistor resistance changes. In that way, the acceleration can be measured. Piezoresistive accelerometers have advantage as the simplicity of their structures and fabrication processes and drawbacks as poor noise, power performance, low sensitivity and large temperature dependence. The first MEMS accelerometer commercialized by NovaSensor was piezoresistive [47].

Piezoelectric sensing is based on a charge polarization of piezoelectric materials

due to the strain caused by the inertial force or the acceleration [23]. A current is generated by the piezoelectric plate due to the acceleration change. This is called self-generating of the accelerometers and the advantage is that no bias voltage or current is needed. The drawbacks are following: static acceleration measuring is not available; piezoelectric accelerometers are strongly dependent on the materials in use, so that difficulty to process the piezoelectric materials is increased and integration with CMOS technology is a big challenge. However, this sensing mechanism has been used to fabricate accelerometers in [48].

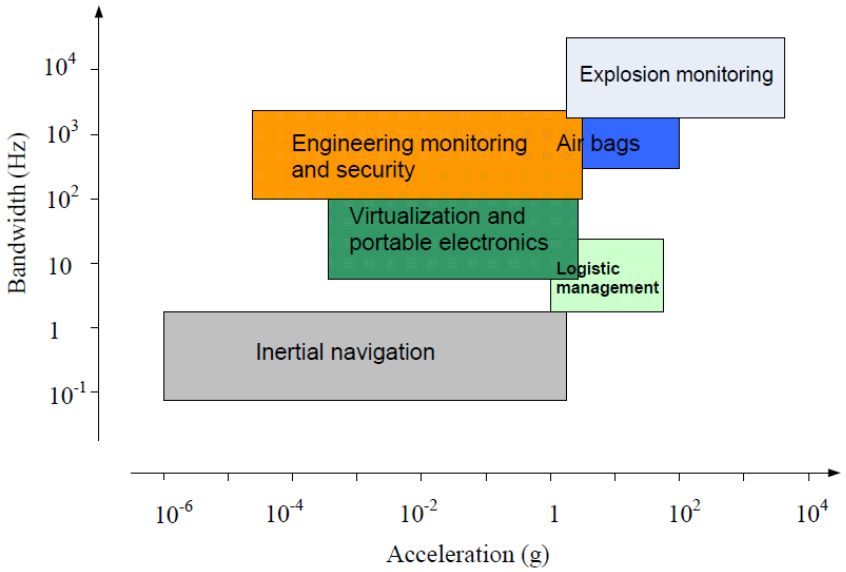

Figure 3.1: Typical applications and performance requirements for accelerometers in these applications [46]

Capacitive sensing is based on detecting small changes in capacitance due to relative displacement of the proof mass. Compared to the other types of MEMS accelerometers, capacitive accelerometers have high sensitivity, low power consumption, low noise level, stable dc characteristics and less temperature dependence [5]. Integrating with CMOS sensing circuits is much easier for capacitive accelerometers due to their simple structures and fabrication processes. Therefore, capacitive sensing mechanism becomes more and more dominant in making MEMS accelerometers.

The integrated CMOS-MEMS capacitive accelerometers have been demonstrated as high-G and low-G sensors. High-G accelerometers are often applied in vehicle crash, safety testing and in-flight munitions testing and the sensors require acceleration measuring up to 20 000 G. A high-G CMOS-MEMS capacitive accelerometer is demonstrated in [49], while low-G accelerometers can be found in [31] [32]. All the accelerometer designs in this thesis are based on the capacitive sensing mechanism and detecting low-G acceleration. More details on capacitive sensing can be found in chapter 5.

However, MEMS accelerometers also can be implemented with the other sensing mechanisms such as thermal transfer, optical and electromagnetic mechanism etc. But these methods and the piezoelectric sensing method described above require more

researches in order to be compatible with the CMOS technology in making monolithic integrated systems on a same chip.

In the following section, the operation principle of the MEMS accelerometers based on capacitive sensing mechanism is illustrated.

3.2 Single-axis capacitive accelerometer

A lumped model of the capacitive accelerometer is shown with the mechanical parameters in figure 3.2. This model is suitable for illustrating the capacitive accelerometers both in lateral and vertical movement. When an external acceleration is applied to the proof mass, the force ($F_{ext} = ma_{ext}$) drives the mass in the direction of the acceleration. The movement gives a change of the capacitance between the rotor (movable finger attached to the proof mass) and the stator (immobile finger attached to the substrate or a frame). The capacitance at equilibrium is C_0 and change of the capacitance gives ΔC. The capacitance change is nearly linear to the displacement of the proof mass when the displacement is much smaller than the gap (g_0). The relationship between capacitance change and displacement is discussed in section 5.2. More details on the capacitive sensing can be found chapter 5.

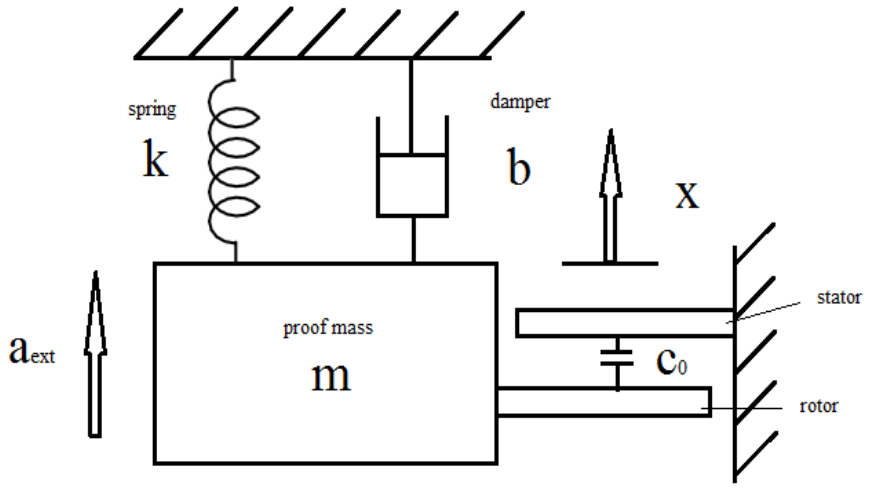

Figure 3.2: Lumped model of a capacitive accelerometer with the key parameters

The lumped model in figure 3.2 can be described as a second order mass-spring-damper system and the differential equation for the displacement x as a function of external acceleration is:

$$m\frac{\partial^2 x}{\partial t^2} + b\frac{\partial x}{\partial t} + kx = ma_{ext} \tag{3.1}$$

where m is mass, b is damping coefficient, k is spring constant and a_{ext} is the external acceleration applied on the proof mass. The equation above converts to a second-order Laplace transfer function as:

$$H(s) = \frac{X(s)}{A(s)} = \frac{1}{s^2 + s\frac{b}{m} + \frac{k}{m}} = \frac{1}{s^2 + s\frac{\omega r}{Q} + \omega_r^2} \tag{3.2}$$

where ω_r is the resonance frequency which equals to $\sqrt{k/m}$, and the quality factor is defined as Q = $\omega_r m/b$.

The MEMS accelerometers are normally operated below the resonance frequency. Most MEMS sensors operate in this region with the typical resonance frequency in the 10 Hz to 10 kHz range [23]. The accelerometers operated above the resonance frequency are used as seismometers to measure the ground vibrations and earth quakes, which are not the types of MEMS accelerometers in this thesis. At low frequency ($\omega \ll \omega_r$),

$$\frac{x}{a} \approx \frac{1}{\omega_r^2} = \frac{m}{k} \tag{3.3}$$

This expression shows the mechanical sensitivity of the accelerometer and we can note that the mechanical sensitivity is inversely proportional to the square of the resonance frequency, which means that decreasing resonance frequency gives higher mechanical sensitivity of the accelerometer. In principle, larger mass and lower spring constant result in decreased resonance frequency, and thus higher mechanical sensitivity. But these two factors are limited by the device size. The spring design with spring constant analysis can be found in section 4.1. The mass is also an important factor on determining the mechanical noise of the capacitive accelerometers. The mechanical noise and damping are discussed in section 4.2.

3.3 System overview

This thesis begins with the design of a single-axis capacitive accelerometer (design A) with lateral motion. A simplified schematic of the system is shown in figure 3.3. The system consists of 6 main components explained in the following:

1. Two anchors sustain the entire system and hold it a distance from the substrate.
2. The rigid frame compensates out-of-plane curling of the comb fingers. More details on the curl compensation frame can be found in section 4.3.
3. Four serpentine springs support the large proof mass. There are also connection beams between the serpentine springs and the proof mass. These beams are designed to be stiffer than the serpentine springs. The details about the spring design can be

found in section 4.1.

4. The proof mass moves in the same direction of the applied acceleration. The movement of the proof mass gives small changes of the capacitances between the comb fingers.
5. The comb fingers include a considerable number of rotors and stators in order to increase the overall capacitance. The rotors are attached to the two sides of the proof mass, while the stators are fixed to the rigid frame. However, the number of fingers is depended on the size of proof mass. More details on the comb fingers design can be found in section 5.3.
6. Four groups of actuators are designed in order to realize self-test of the system. The actuators have the same structure as the comb fingers. Discussion of the self-test actuators can be found in section 5.4.

The 6 components shown above constitute the single-axis lateral capacitive accelerometer. This design has been realized by post-CMOS processing and the layout made in Cadence. The size of the accelerometer is $325\mu m \times 355\mu m$.

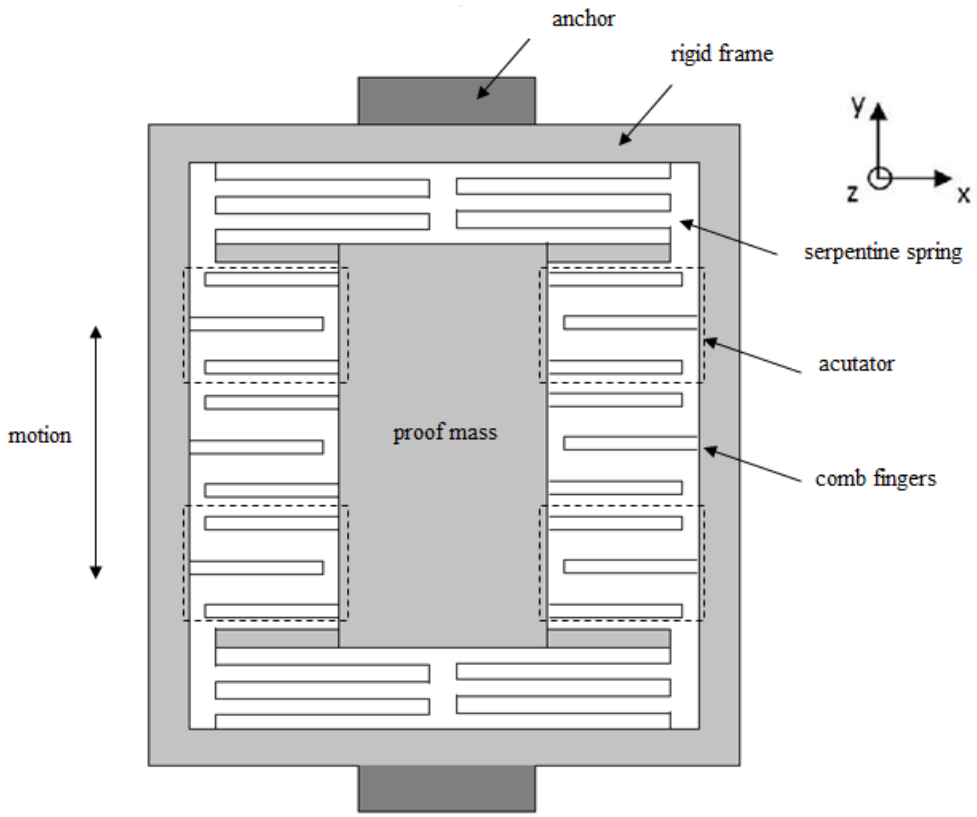

Figure 3.3: Schematic for the single-axis lateral capacitive accelerometer (design A)

Based on design A, another design is considered. Figure 3.4 shows a sketch of the design B. The primary concept is to increase the number of sensing fingers for increasing the overall sensing capacitance. The center part of the proof mass in design A is removed and replaced with comb fingers. The additional rotors are attached to the

inside of the proof mass and the stators are settled on the anchor in the center. The proof mass is sustained by two compliant springs which are also the leading routes for the output signals. The type of design sacrifices a part of the proof mass and increases the spring constant because of the two additional springs, which means that the mechanical sensitivity is decreased according to equation (3.3). But the overall sensing capacitance is increased in a great amount. The total sensor sensitivity can be increased. The sensor sensitivity is explained in equation (5.9) in chapter 5. Design B has reference from [35], where the capacitive accelerometer is shown with improved sensitivity. Because it is uncertain for that design B is realizable, the design is not made in Cadence, but the analysis and more discussions are covered in chapter 6.

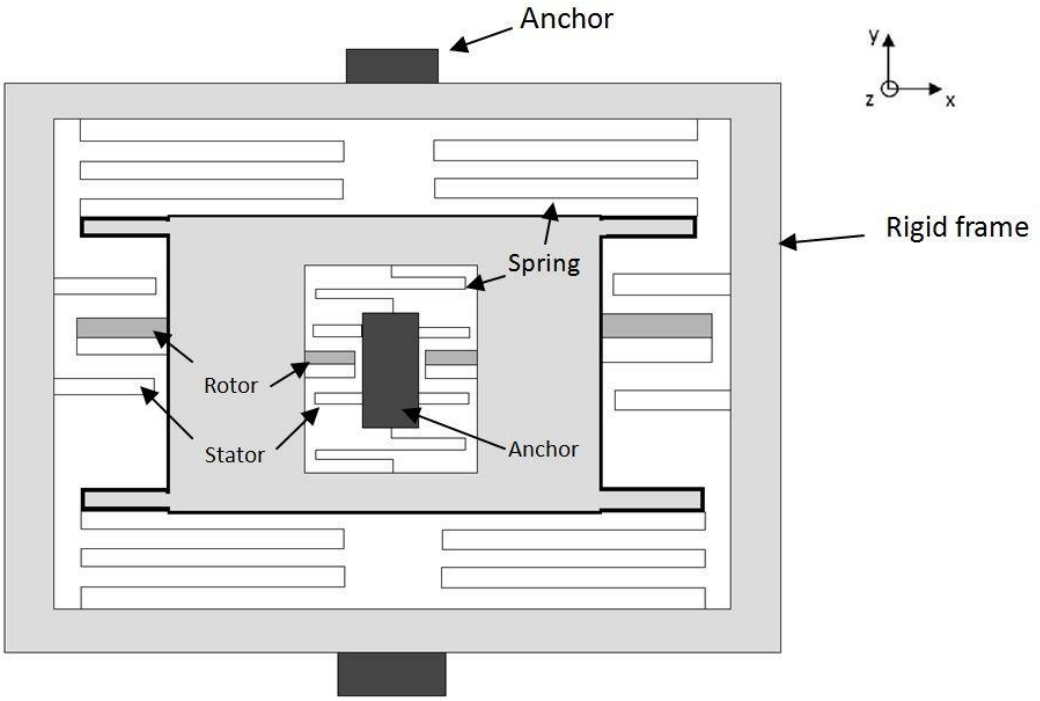

Figure 3.4: Alternative design of the single-axis lateral capacitive accelerometer (design B)

Another design realized in post-CMOS MEMS is a dual-axis in-plane capacitive accelerometer by integrating two single-axis lateral capacitive accelerometers (design A). A schematic of the design is shown in figure 7.1. The design is using one single-axis lateral capacitive accelerometer without the anchors as a proof mass and adding the same structural components mentioned earlier in the section around the "new" proof mass. The inner accelerometer can detect the movement in y-direction, while the outer accelerometer is sensitive to the movement in x-direction. The benefit of this design is a miniaturized size of the overall system. A problem with this integration is that the inner and outer accelerometers can influence each other, and thus additional signals in the output. The dual-axis in-plane capacitive accelerometer has a size of $440\mu m \times 550\mu m$. More details can be found in chapter 7.

Chapter 4

Mechanical structures, design and modeling

This chapter takes the focus on design of the mechanical structures in the single-axis lateral capacitive accelerometer. The mechanical components include springs, a proof mass, comb fingers and a rigid frame. The design consists of mathematical modeling, theoretical analysis and 3D FEM (Finite Element Method) simulation. A layout of the accelerometer is implemented in Cadence after the dimensions of the structures are determined.

4.1 Spring design

In order to achieve high sensitivity for the accelerometer, a compliant spring with low stiffness has to be designed. Due to the lumped model and equation (3.3) described in section 3.2, the main goal in spring design is that a small spring constant, k-value in sensing direction has to be obtained. Based on Hooke's law, the spring constant can be defined as:

$$k = F/\delta \tag{4.1}$$

where F is the force applied to the open end of the spring and δ is displacement of the open end from its equilibrium position, while the other end of the spring is anchored. A dimension-depended expression of spring constant for the chosen spring design will be discussed in the following sections.

4.1.1 Flexural spring topologies

There are many types of springs which can be utilized in the design of an accelerometer. Four flexures are commonly used in micromechanical designs: the fixed-fixed flexure, the crab-leg flexure, the folded flexure, and the serpentine flexure. Figure 4.1 shows the four types of springs. The fixed-fixed flexure/clamped-clamped flexure is stiffest among these four types. A variation of the fixed-fixed flexure is crab-leg flexure where the "thigh" is added in order to reduce the extensional axial stress [19]. The folded flexure

has lower stiffness compared to the two flexures above and also has reduced axial stress. Several variations of the folded flexure and analysis are given in [20].

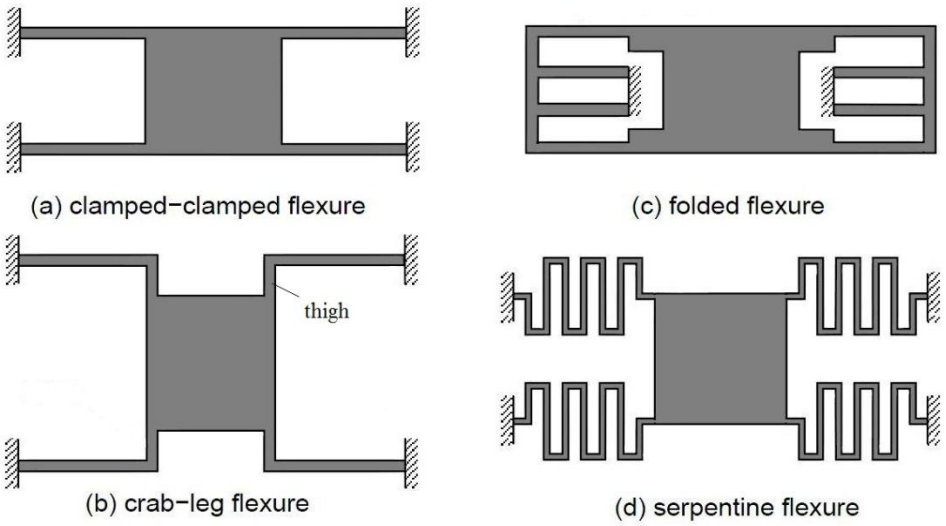

Figure 4.1: Various spring design. (a) fixed-fixed flexure. (b) crab-leg flexure. (c) Folded flexure. (d) Serpentine flexure. [21]

The serpentine flexure shown in figure 4.1(d) is used in the design of the micromechanical system in this thesis. Compact springs can be designed to form compliant serpentine flexures. It means that the springs with small spring constant can be made in a small area. The flexure is made of four serpentine springs. The meandered beam like a snake in shape gives the name of the serpentine spring. The dimension of the meanders can be adjusted to give the desired stiffness of the springs. It is further discussed in the following sections.

4.1.2 Spring constant analysis

The serpentine springs with a proof mass shown in figure 4.2, are used in the design of the single-axis lateral capacitive accelerometer. The proof mass is suspended by 4 serpentine springs with uniform dimensions in order to ensure that the motion of the proof mass is balanced. The open end of one spring is attached to the corner of the proof mass, while the other end is anchored. Compared with the midpoint attachment design shown in figure 4.3, the corner attachment design can avoid the problem with tilting and provides better curl matching. Between one serpentine spring and the proof mass, there is also a connection beam which is much stiffer than the serpentine spring.

The motion of the proof mass and the displacement of the open-end of the spring are defined in y-direction. The total spring constant defined in y-direction ($k_{y,tot}$) is the desired mechanical parameter.

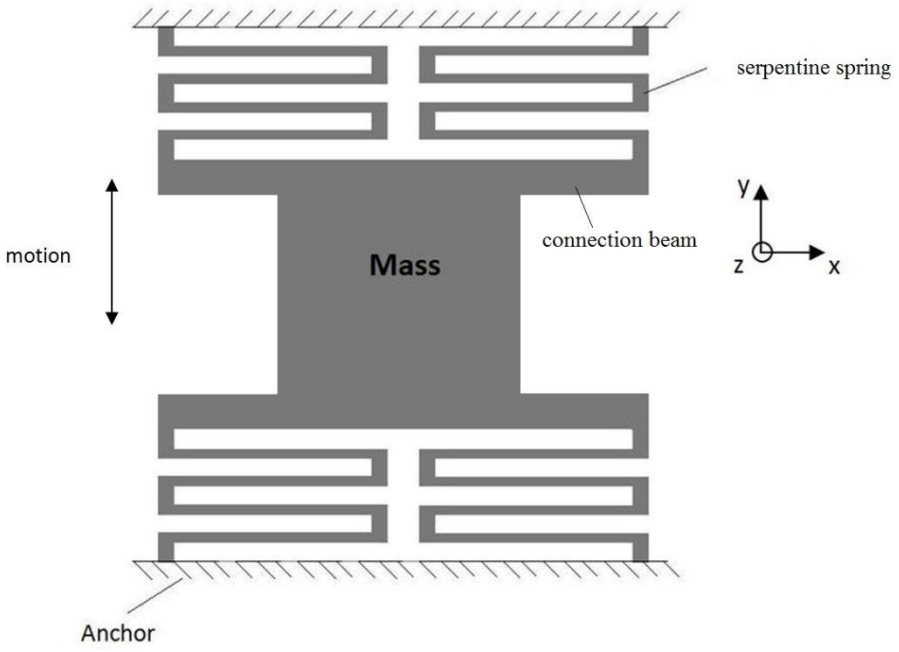

Figure 4.2: Serpentine springs with proof mass

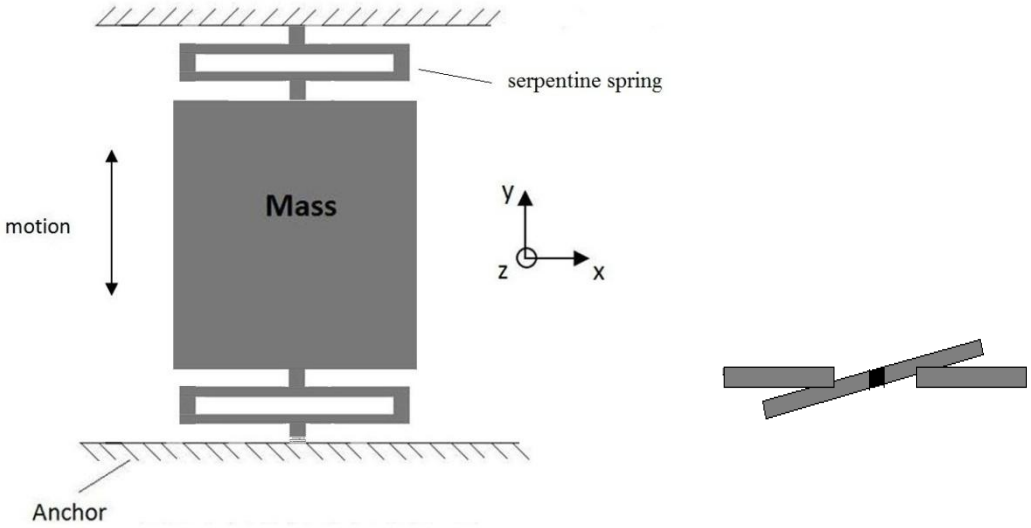

Figure 4.3: Midpoint attachment of the serpentine springs and tilting problem

Based on equation (4.1), the total spring constant for four serpentine springs in y-direction is obtained:

$$k_{y,tot} = 4k_y = 4F_y/\delta_y \tag{4.2}$$

where k_y is the spring constant of one serpentine spring in y-direction. For a constant force F_y provided by the proof mass, a larger displacement of the spring, δ_y means a smaller spring constant. As mentioned in section 3.2, the spring constant is one of the key parameters in the accelerometer design, and it can be adjusted by changing

dimensions of the spring.

To have a better analysis on the spring constant, one of the serpentine springs is illustrated with the key geometrical parameters in figure 4.4(a). The long beam has width w_l and length l, while the short beam has width w_d and length d. The number of the short beams determines the number of turns, n which equals to 5 in figure 4.4(a). Figure 4.4(b) shows the cross section of the composite beam in the serpentine springs, which is made of three metal layers and dielectric layers in-between. The signal definitions can be found in table 8.2.

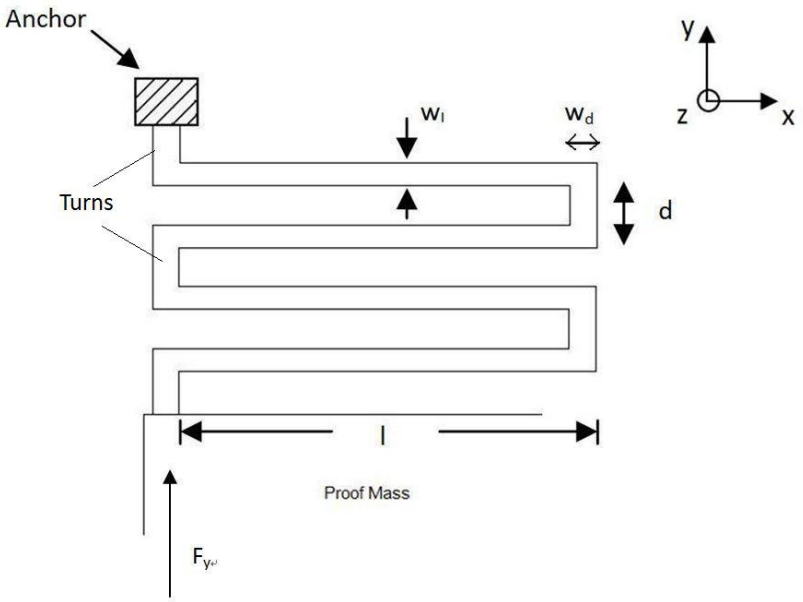

(a)

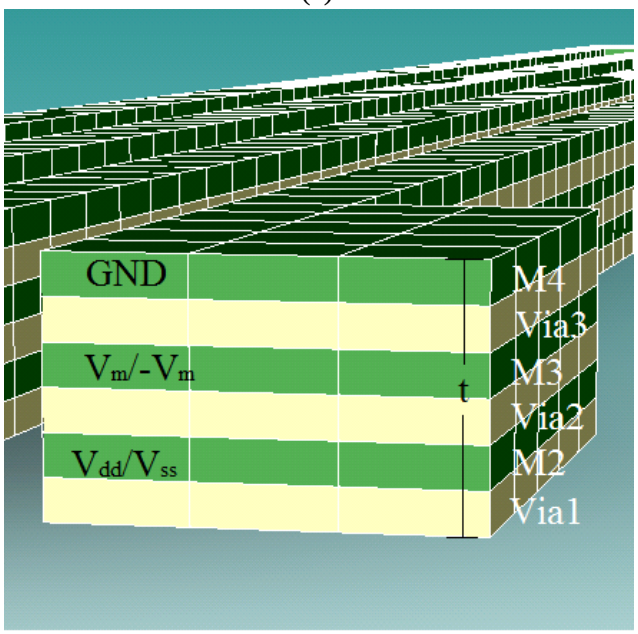

(b)

Figure 4.4: (a) One serpentine spring with the key parameters.
(b) Cross section of the composite beam.

Three mathematical models are obtained in the analysis of the spring constant in y-direction. These are described in the following.

Model 1

One simple method to obtain the spring constant k_y is that the serpentine spring is considered as several cantilever beams in series. The effect of the short beams is ignored in this model. Figure 4.5(a) shows that the serpentine springs are split into several cantilever beams. In this model, the open-end of the serpentine spring is not attached by the proof mass; therefore the short beams are free to rotate when the cantilever beams are bent as shown in figure 4.5(b).

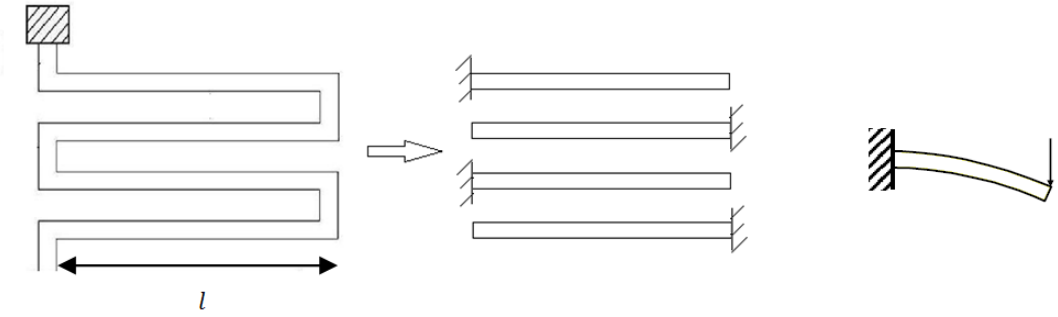

(a) (b)

Figure 4.5: (a) Simplified model for the serpentine spring with free end; (b) Free cantilever beam.

A cantilever beam with a free end is shown in figure 4.5(b) and the spring constant for the free cantilever beam is given by [22]:

$$k_0 = \frac{3EI}{l^3} = \frac{Etw_l^3}{4l^3} \tag{4.3}$$

where I is moment of inertia which is given by:

$$I = \frac{tw_l^3}{12} \tag{4.4}$$

and the spring constant in y-direction, k_y for one serpentine spring can be obtained:

$$k_y = \frac{k_0}{n_b} = \frac{Et}{4n_b} \cdot \left(\frac{w_l}{l}\right)^3 \tag{4.5}$$

where n_b is the number of beams, E is Young's modulus and t is the beam thickness as it is shown in figure 4.4(b).

Model 2

Another way to model the serpentine spring is shown in figure 4.6(a). The serpentine spring is considered as several guided cantilever beams in series. A guided cantilever beam is shown in figure 4.6(b). In this model, the serpentine spring is attached to the proof mass as the guided end; therefore the short beams are not free to rotate and just can move in y-direction when the cantilever beams are bent. The bending shape is shown in figure 4.6(b).

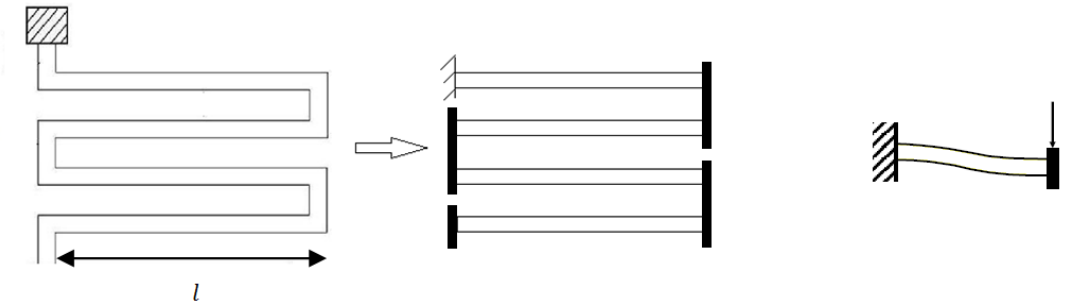

(a) (b)

Figure 4.6: (a) Simplified model for the serpentine spring with guided end; (b) Guided cantilever beam.

For a guided cantilever beam, the spring constant is given by [22]:

$$k_0 = \frac{12EI}{l^3} = \frac{Etw_l^3}{l^3} \tag{4.6}$$

Thereby, the spring constant in y-direction for model 2 is obtained:

$$k_y = \frac{E \cdot t}{n_b} \cdot \left(\frac{w_l}{l}\right)^3 \tag{4.7}$$

Both equation (4.5) and equation (4.7) show that the spring constant in y-direction is dependent on the materials of the composite beam, the thickness of the beam, the number of the long beams, and the ratio between width and length of the long beam. Young's modulus of the beams is constant in this analysis. The thickness is difficult to get accurate because of the post-CMOS process and fabrication variation. However the thickness is considered to be constant in order to simplify the theoretical analysis and the simulation. Figure 4.4(b) shows the 3 metal layers used to construct the composite beams in the serpentine springs. The input signals are routed in the beams as shown in figure 4.4(b). The routing topology will be further described in the capacitive sensing in chapter 5.

The spring constant in y-direction is inverse proportional to the number of the long beams. In other words, more beams result in smaller k_y, and thus reduced stiffness of the

serpentine springs, but also reduced stiffness in the undesired direction (x- and z-direction). The ratio between the width w_l and length l of the long beam is more critical than the other elements in model 1 and 2. The length is a critical parameter in order to obtain small spring constant k_y. It is also important to note that the spring constant in model 2 is 4 times of the spring constant in model 1.

Figure 4.7 shows how the spring constant k_y varies as the width of the long beam changes and comparison between different lengths of the beam. The graph shows that the spring constant k_y decreases as the width is smaller. But the width of the long beam is limited by post-CMOS design rules and routing of the signals. Therefore, the width is determined to be at least $2\mu m$. The graph in figure 4.8 shows that the spring constant decreases as beams are made longer when the width is $2\mu m$. As it is shown in figure 4.9, larger number of the long beams gives also decreased spring constant.

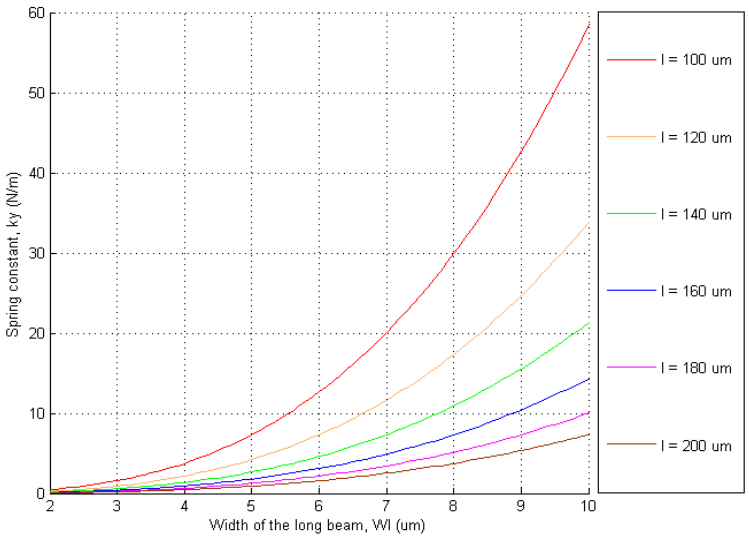

Figure 4.7: Spring constant as a function of the long beam width (w_l)

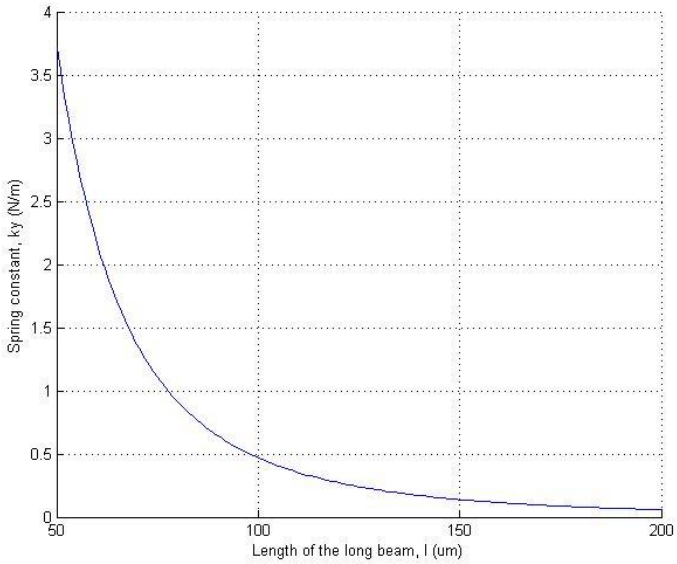

Figure 4.8: Spring constant as a function of the long beam length (l)

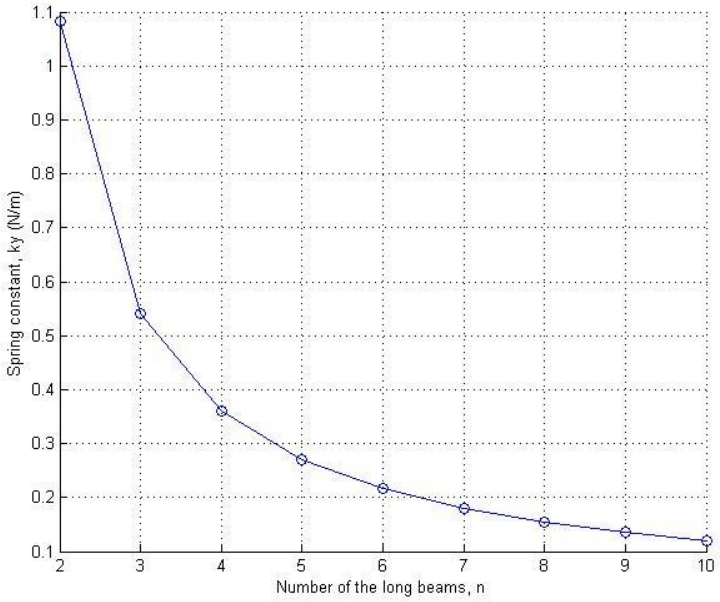

Figure 4.9: Spring constant as a function of the number of long beams

Model 3

Another analytic method to model the spring constant of the serpentine springs can be found in Gary F. Fedder's PhD thesis [21]. This method is based on the definition (4.1) and using the guided cantilever beams for the serpentine spring. Only displacement caused by bending and torsion is considered in the analysis. Deformation from shear, beam elongation, and beam shortening is neglected. In the mathematical analysis of the single-axis lateral capacitive accelerometer, only the spring constant in y-direction is the interest and assume that the curling of the multilayer structure has no influence on the spring constant. The spring constant k_y is given by [21]:

$$k_y = \frac{12EI_{zl}\,[(\tilde{c}+l)\cdot n - l]}{l^2(n-1)[(3\tilde{c}^2+4\tilde{c}l+l^2)\cdot n+3\tilde{c}^2-l^2]} \tag{4.8}$$

where I_{zl} is the same as I in equation (4.4). The number of turns, n is an odd number due to the corner attachment design of the serpentine springs. A new parameter is introduced, namely $\tilde{c}$ which is defined as:

$$\tilde{c} \equiv d \cdot \frac{I_{zl}}{I_{zd}} \tag{4.9}$$

where I_{zd} is the moment of inertia for the short beam and is given by $tw_d^3/12$. Then $\tilde{c}$ can be simplifed as:

$$\tilde{c} = d \cdot \left(\frac{w_l}{w_d}\right)^3 \tag{4.10}$$

As equation (4.10) shows, the new introduced parameter $\tilde{c}$ is dependent on the length of the short beam d, and the ratio between the width of the long beam w_l and the short beam w_d. Thereby, the spring constant k_y is dependent on all the geometrical parameters illustrated in figure 4.4(a). In the spring constant analysis, one of the geometric parameters varies while the other parameters, Young's modulus and the thickness are constant. Searching for the most critical geometric parameter for tuning the spring constant in spring design is the main goal in the analysis in this thesis.

Due to limitation of the post-CMOS design rules, the length of the short beam must be larger than the width of the long beam in order to form a minimum gap between the beams ($d - w_l > 1.2\mu m$). The width of the long beam w_l is set for 2 μm. The ratio w_l/w_d is becoming smaller by increasing w_d and it results in an increased spring constant, as it is shown in figure 4.10. But the spring constant increases slightly when the width is more than 5 μm. The graph in figure 4.11 shows that the spring constant is decreased slightly by increasing the length of the short beam.

Therefore, it can be concluded so far that: the long beam length and the number of beams are the critical parameters to adjust the spring constant in y-direction because of their large tuning range.

Note that equation (4.8) can be simplified as ($\tilde{c} \ll l$):

$$k_y = \frac{Etw_l^3}{(n-1)l^3} \tag{4.11}$$

where (n-1) is the same as n_b in equation (4.7) giving a similar equation as equation (4.11). In other words, model 2 is a version of simplified model 3. However, model 3 has more details about the spring constant. It is also important to observe that the spring constant in model 3 is 4 times of the spring constant in model 1.

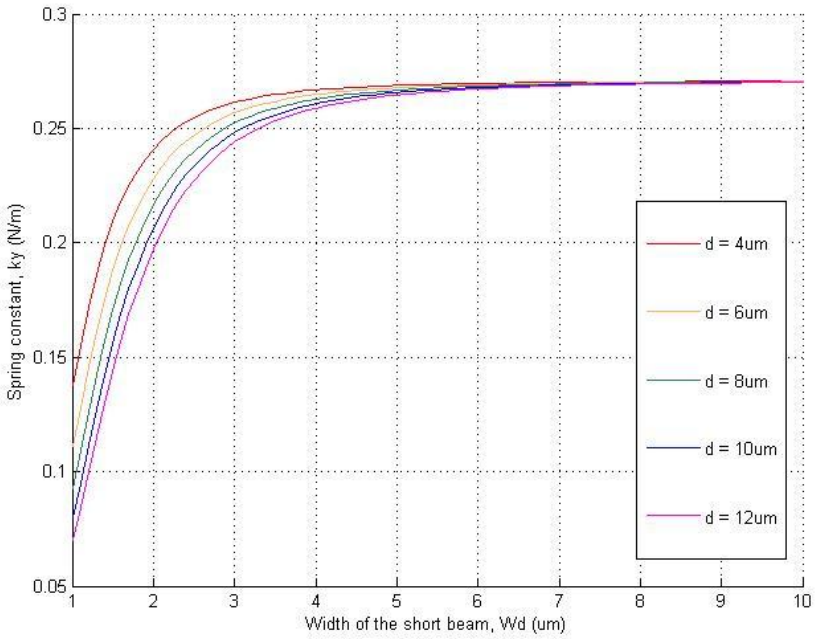

Figure 4.10: Spring constant as a function of the short beam width

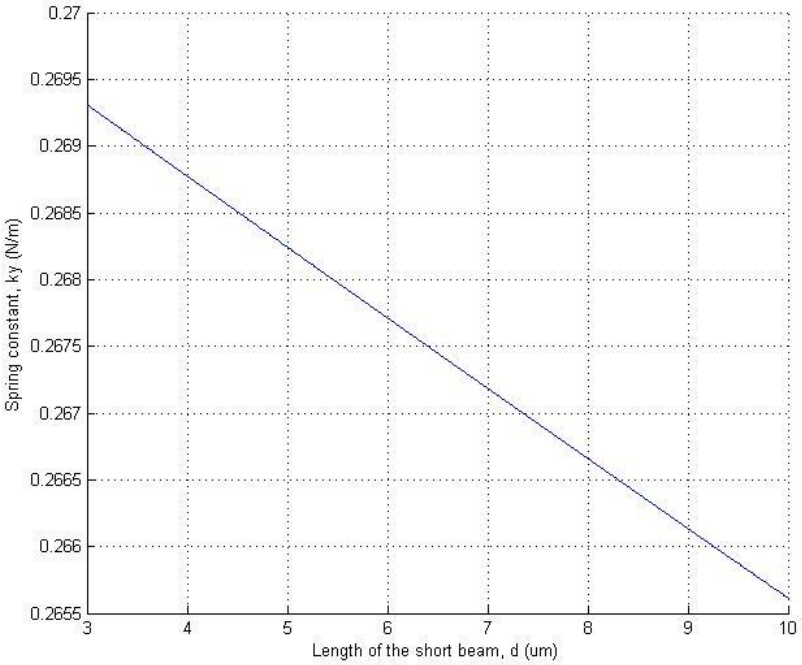

Figure 4.11: Spring constant as a function of the short beam length

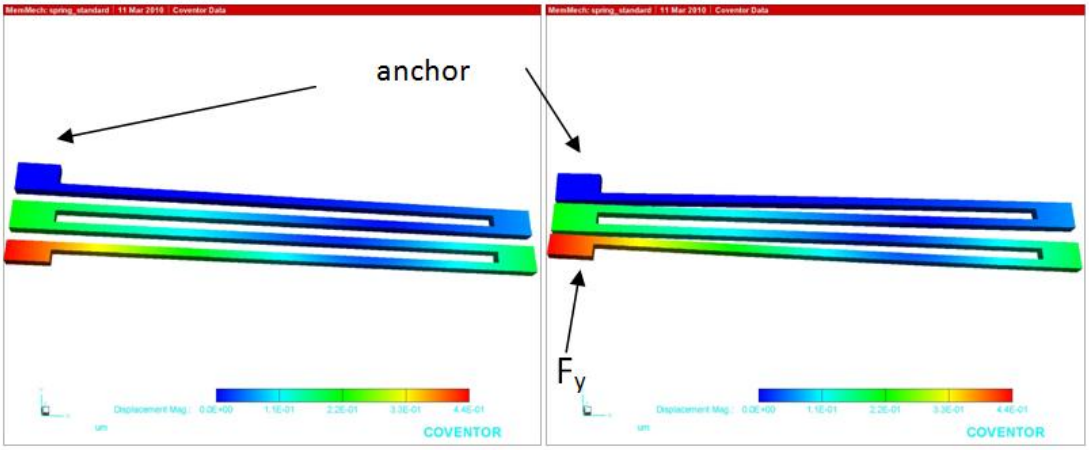

Figure 4.12: 3D model for one serpentine spring and deflection of the structure

4.1.3 Simulation of one serpentine spring

To simplify the simulation of the mechanical structures, only one of the serpentine springs is made without the proof mass. The reason is that the simulation of a complex system is time consuming. The purpose of the simulation is to verify model 1 for calculation of the spring constant, by observing the maximum displacement of the spring in y-direction. The serpentine spring is simulated by 3D FEM analysis in CoventorWare. By tuning the geometric parameters described in section 4.1.2, the simulation results are obtained by looking at the deflection of the serpentine spring. As it is shown in figure 4.12, the maximum displacement occurs at the open-end of the

spring while the other end is anchored. The bending shape is similar to a free cantilever beam which is described in model 1. The 3D model in figure 4.12 is made of a uniform material with average Young's modulus of 74GPa and thickness of 4.5 μm, approximating the actual multilayer structure. It is also important to remember that the displacement is increased as the spring constant decreases (F_y is constant). Then the spring constant in y-direction can be obtained based on equation (4.1).

Figure 4.13 shows how the spring constant in y-direction varies in simulation, by changing the geometrical parameters which are involved in model 1. The spring is simulated with several critical values of the dimensions. By increasing the width of the long beam, the spring constant increases as it is shown in figure 4.13(a). Both the mathematical model and simulation results illustrate that the width of the long beam should be kept as small as possible in order to achieve a small spring constant. Due to the limitation of the post-CMOS design rules, w_l is confirmed to be $2\mu m$ as it is already mentioned in section 4.1.2. The graph of the mathematical model 1 has a very good match compared to the simulation results as it is shown in figure 4.13(b). There is no doubt about that longer beams give smaller spring constant. The length of the long beam is the most effective parameter in tuning the spring constant. Another critical factor is the number of turns. The graph and the simulation results in figure 4.13(c) show that more turns of the serpentine spring obviously result in decreased spring constant in y-direction. But increased number of the turns gives reduced stiffness in the undesired directions (x- and z-direction) as well, and that will cause increased noise in the output signals and offset problems.

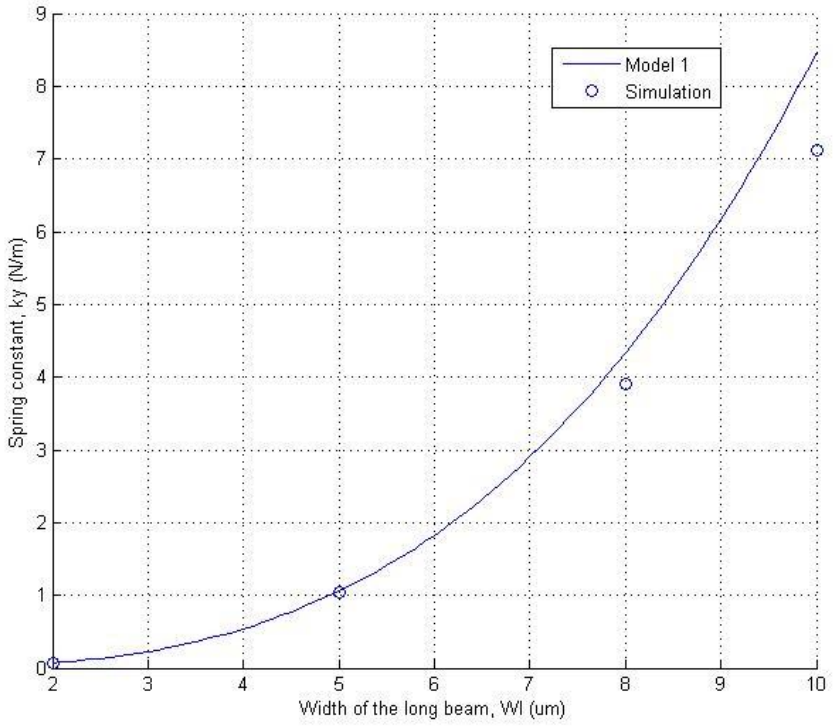

(a)

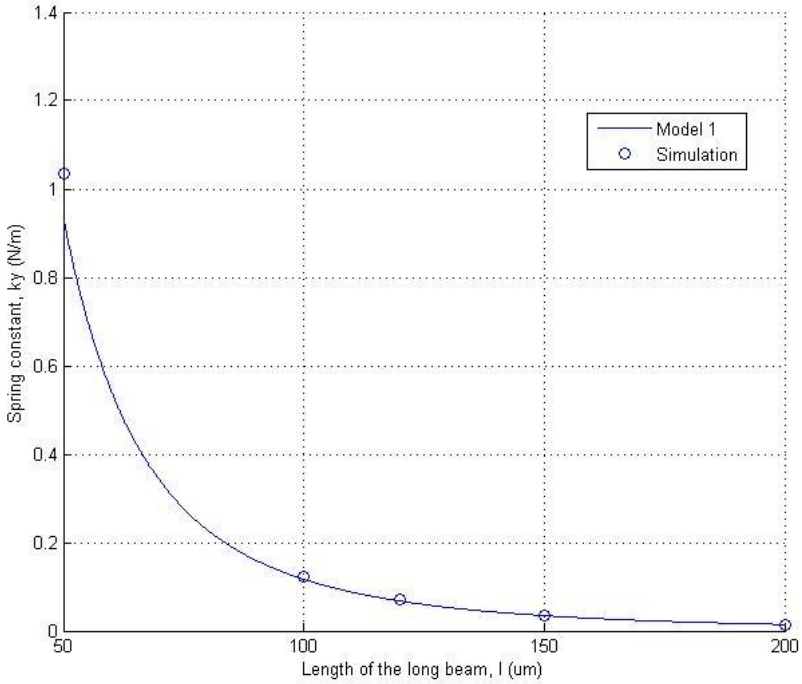

(b)

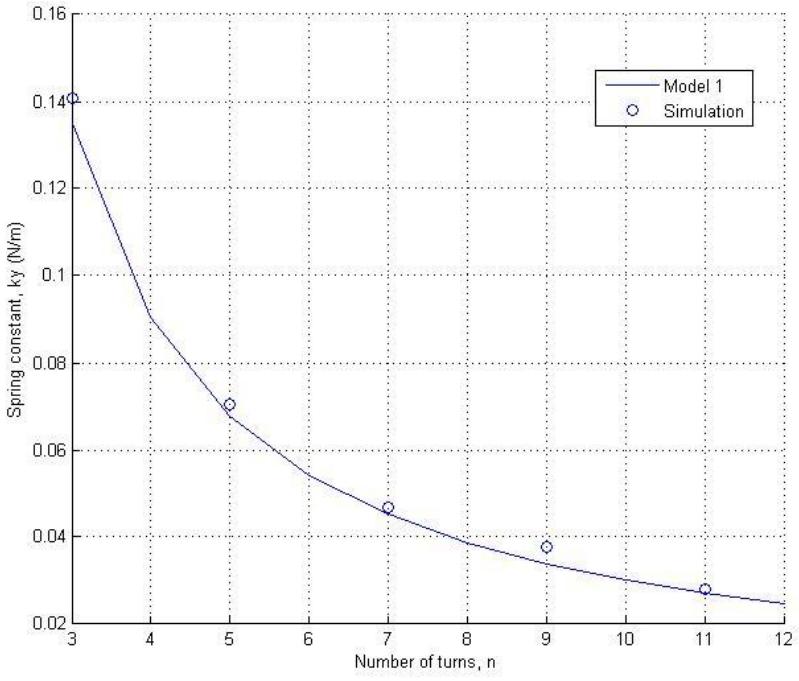

(c)

Figure 4.13: Spring constant as a function of (a) Width of the long beam, w_l; (b) Length of the long beam, l; (c) Number of turns, n. (model 1 vs. simulation)

The mathematical model 1 has no contribution on the spring constant from the geometrical parameters the short beam width and length (w_d and d). Thereby it cannot

be use for comparison with the simulation results. As it is described in section 4.1.2, model 3 has more details and the spring constant in model 3 is nearly 4 times of the spring constant in model 1. Therefore, there is no risk to describe the spring constant k_y for one serpentine spring by using modified model 3 (model 3 divided by 4). Table 4.1 shows the simulation results in comparison with the modified model 3. By changing the dimensions of w_d or d, there is no large difference between the simulation and the mathematical model. As it is already described in model 3 in section 4.1.2, the spring constant in y-direction is increased as the short beam width increases. Therefore, w_d dimension should be kept small. When the length of the short beam is smaller, the term $\tilde{c}$ in model 3 becomes much smaller than the long beam length (l), so that it can be neglected in model 3. The mathematical model 3 for the spring constant k_y can be simplified to model 2 which is independent on the geometric parameters of the short beam.

Table 4.1: Spring constant by changing dimension of (a) width of the short beam, w_d; (b) length of the short beam, d. (simulation result vs. modified model 3)

Dimension of w_d (μm)	**Spring constant of sim. result (N/m)**	**Spring constant of modified model 3 (N/m)**
5	0.068	0.0671
10	0.070	0.0676
15	0.073	0.0677

(a)

Dimension of d (μm)	**Spring constant of sim. result (N/m)**	**Spring constant of modified model 3 (N/m)**
5	0.0704	0.0676
10	0.0703	0.0675
15	0.0702	0.0674

(b)

As an overall result, the simulation results match with the mathematical models. After the mathematical analysis and the simulation, the conclusion is that the length of the long beam is the most critical parameter in tuning of the spring constant in y-axis, k_y. But the mathematical models do not take the effect of composite multilayer beams into account. Due to the post-CMOS MEMS process and routing of the signals, the beams of the serpentine springs are made of 3 metal layers (Al) and dielectric layers (SiO_2) in between. As it is shown in figure 4.14, the spring with 3 metal layers has a minor increase in the displacement in y-direction. In other words, the stiffness of the beams

with multilayer is slightly decreased. With the mathematical models, it can be interpreted as the average Young's modulus of the composite structure is smaller than the uniform material; hence the spring constant decreases with multilayer.

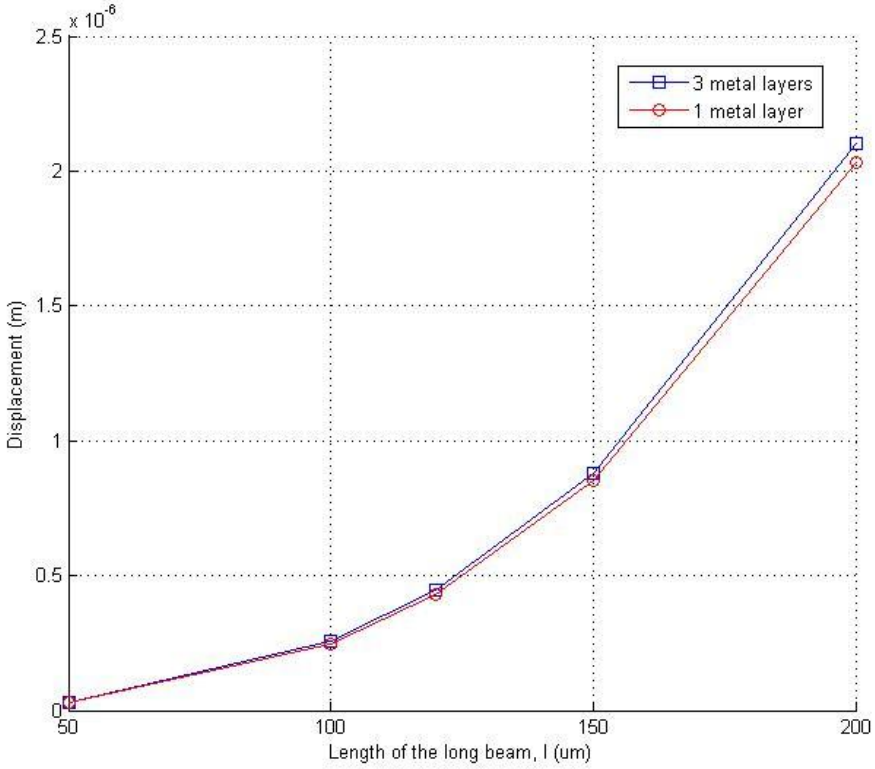

Figure 4.14: Displacement in y-direction as a function of the long beam length
Multilayer vs. uniform material

4.1.4 The proof mass with serpentine springs

A simple sketch of the proof mass with four serpentine springs has been shown in figure 4.2. According to the equation (3.3), the mechanical sensitivity increases as a larger mass is made. But the proof mass is constrained by the size of the entire device. Within an available area, a large mass has to be designed in order to increase the mechanical sensitivity, and thus the overall sensitivity of the accelerometer. The number of the comb fingers is also determined by the size of the proof mass. A proof mass with four serpentine springs is made to be simulated in CoventorWare, as it is shown in figure 4.15.

To simplify the simulation, the model is made with uniform material and thickness. Due to the post-CMOS MEMS design rules; a certain number of holes should be made inside the proof mass in order to release the MEMS structure in the final post processing step. The FEM simulation with a large system such as the model in figure 4.15 is time consuming. Therefore, no holes are made in the 3D model, and the comb fingers are not included. But the 3D simulation model is made with nearly the same weight as the actual proof mass which is calculated beforehand. The dimensions of the serpentine

springs are fixed. There are 4 beams made to connect the serpentine springs and the proof mass. The purpose with these connection beams is to make full use of the available area in the design. It is also a benefit to design the serpentine springs with longer beams. These connection beams are designed to be much stiffer than the serpentine springs. Since the springs are attached to the proof mass, the short beams are not free to swing to the sides but can only move in the y-direction. Therefore, the serpentine springs are supposed to be 4 times stiffness of the 3D model (single serpentine spring) in figure 4.12.

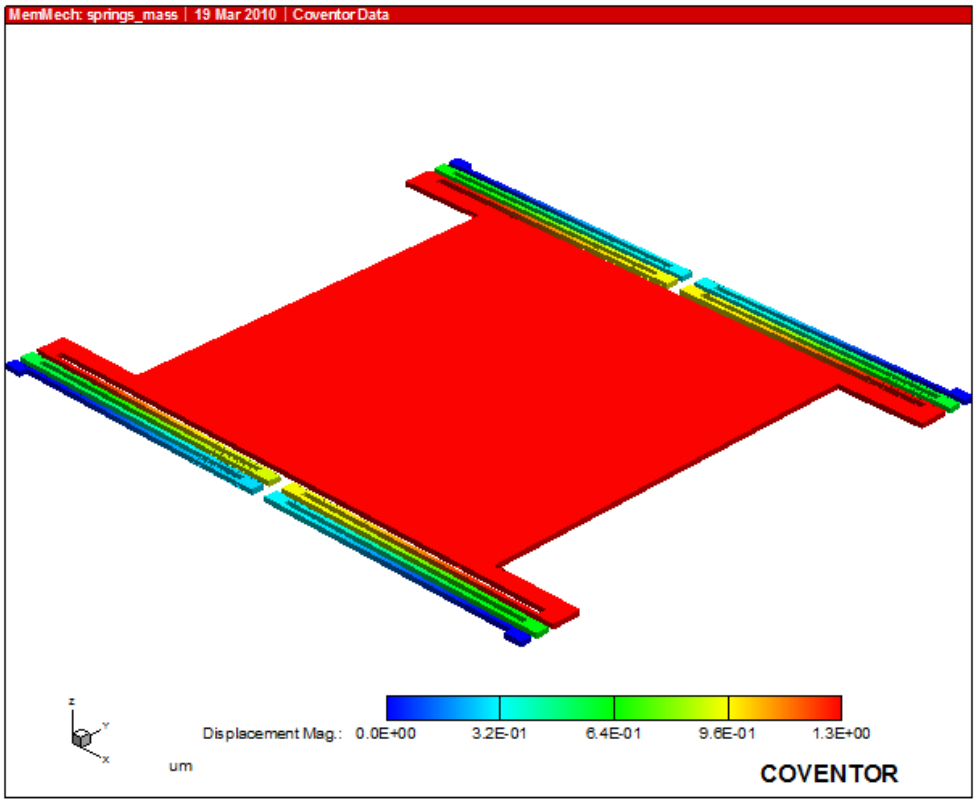

Figure 4.15: 3D model for the proof mass and 4 serpentine springs after simulation

As a result after the simulation shown in figure 4.15, the maximum displacement occurs at the connection beams and the proof mass (red color). The connection beams are not bent so much when an external acceleration drives the proof mass moving laterally in y-direction. The beams are stiff enough and can be considered as a part of the proof mass. The proof mass and the 4 connection beams are nearly $0.7\mu g$ (same weight as the actual proof mass) in the 3D model in figure 4.15. The uniform thickness of the structure is $4.5\mu m$. As table 4.2 shows, the calculated results by mathematical model 2 is very similar to the results by the model 3. The simulation results show that the serpentine springs are a little stiffer than the mathematical models. A modal analysis is also simulated for the model. Corresponding resonance frequency for the mathematical models and simulation is shown in the table. Note that the unit for the mechanical sensitivity is nm/G and 1 G equals to 9.81 m/s^2.

Table 4.2: Spring constant and the mechanical sensitivity, calculation vs. simulation

Definition	Model 2	Model 3	Simulation
Total spring constant in y-direction ($k_{y,tot}$)	0.789 N/m	0.784 N/m	0.891 N/m
Resonance frequency	5.34 kHz	5.33 kHz	5.68 kHz
Mechanical sensitivity	8.7 nm/G	8.76 nm/G	7.71 nm/G

4.1.5 Implementation

Figure 4.16 shows the layout of the serpentine springs and the proof mass that is implemented in Cadence. Only the top metal (M4) and the polysilicon layers are shown. The proof mass is constructed with a number of holes and some of the geometrical parameters are slightly changed due to the post-CMOS design rules and CMOS design rules. The gap between the beams in the serpentine springs is set for $2\mu m$ in order to fulfill the design rules and give space for a maximum displacement.

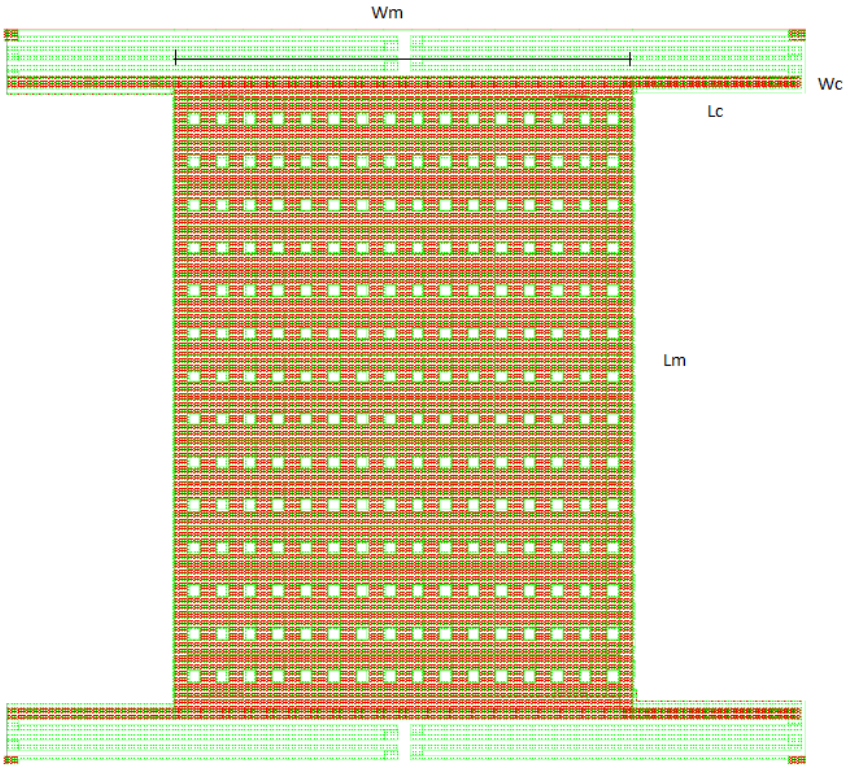

Figure 4.16: Layout of the serpentine springs and the proof mass

Table 4.3: Design parameters for the single-axis lateral capacitive accelerometer

Parameters	Symbol	Dimensions
Width of the long beam	w_l	$2\mu m$
Length of the long beam	l	$150\mu m$
Width of the short beam	w_d	$5\mu m$
Length of the short beam	d	$4\mu m$
Thickness of the beams	t	$\sim 4.5\mu m$
Number of turns	n	5
Width of the proof mass	W_m	$185\mu m$
Length of the proof mass	L_m	$255\mu m$
Size of the holes	$w_h \times l_h$	$4\mu m \times 4\mu m$
Number of holes	n_h	224
Width of the connection beam	W_c	$5\mu m$
Length of the connection beam	L_c	$65\mu m$
Thickness of the proof mass and connection beam	t_m	$\sim 5.5\mu m$
Mass of the proof mass	m	$\sim 0.7\mu g$

As a summary, the design parameters used for the fabricated single-axis lateral capacitive accelerometer, are illustrated in table 4.3. Decreased width of the short beam gives decreased spring constant in y-direction, as the graph is shown in figure 4.10. The short beam has the minimum width which can reduce the displacement in undesired direction (x-direction). The length of the proof mass determines the number of comb fingers attached to the proof mass. The total proof mass consists of the mass of the 4 connection beams, the mass of comb fingers and the weight of proof mass with the holes. Based on equation (3.3), mechanical sensitivity of the single-axis lateral capacitive accelerometer (design A) in this design is 7.71 nm/G. With a maximum gap of $2\mu m$, the accelerometer can measure a maximum acceleration of 260 G in theory. The resonance frequency for the accelerometer is 5.68 kHz. As mentioned, the accelerometer is operated below this frequency.

4.2 Noise, damping and Q-factor

According to the transfer function in equation (3.2), the damping coefficient b is one of the factors which can reduce the performance of the accelerometer. In Microsystems, there are several different damping sources such as the intrinsic material losses, anchor losses (structural losses) and the air damping [23]. Structural losses are as much as five orders of magnitude lower than viscous effects at atmospheric pressure and thus may be ignored [24]. The primary damping occurs in the lateral capacitive accelerometer is the air damping because the microstructures are so small and have to push away the air molecules. The air damping can be controlled by either the gas pressure inside the device package or the device geometry. Reducing the air pressure using vacuum package is the way to reduce the damping coefficient, and thus the quality factor $(Q = \omega_r m/b)$ is increased.

For the lateral capacitive accelerometers in this thesis, the proof mass has a large distance above the substrate (ca. $50\mu m$) and moves laterally. Couette-flow (air or fluid between two parallel plates) damping between the proof mass and the substrate can thus be neglected. Due to the great number of the comb fingers in the lateral accelerometers, squeeze-film damping which occurs between the comb fingers is the primary source for the air damping. Figure 4.17 shows that the air is pressed out between the fingers when the rotors are moving towards the stators. The capacitive sensing is operated by changing the gap between the plates of a capacitor; more details are covered in chapter 5.

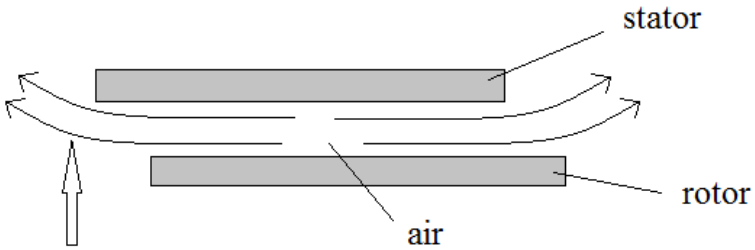

Figure 4.17: Squeeze-film damping between the stator and rotor

The squeeze-film damping coefficient between one stator and one rotor is given by [25]:

$$b_0 = \mu_{eff} L_{eff} (\frac{t}{g_0})^3 \qquad (4.12)$$

where μ_{eff} is effective viscosity of the air which equals to $1.837 \cdot 10^{-5}$ Pas at atmospheric pressure and 20°C, L_{eff} is overlapping length of the stator and the rotor, t is thickness of the fingers and g_0 is the gap between the fingers. As it is shown in the equation, longer and thicker beams result in larger damping coefficient. Larger distance between the fingers gives decreased damping coefficient. More details on the

geometrical parameters for the comb fingers can be found in table 5.1 in chapter 5. For the single-axis lateral capacitive accelerometer of design A, there are 42 gaps when the proof mass is moving toward one direction. The overall damping coefficient can be obtained as $1.02 \cdot 10^{-6}\, Ns/m$ or $1.02\, \mu kg/s$, and thus the quality factor assuming squeeze-film damping is 4 after calculation. The quality factor in reality is expected to be a little lower than 4 when the other damping forces are taken into account.

The quality factor is critical for the response time for an accelerometer. As Ville Kaajakari describes in his book [23], the optimal speed is obtained with critical damping (Q = 0.5) as it is shown in figure 4.18. Over-damped accelerometer (Q < 0.5) has lower response time. The quality factor calculated above is larger than the critical one, which means that the designed accelerometer in this thesis is an under-damped accelerometer with high quality factor. As it is shown in the figure, high quality factor results in ringing of the proof mass that is not desired. The ringing exhibits in the output signals significantly and can be interpreted as noise in the signals. One solution to filter this ringing is to operate the accelerometer at a bandwidth which is much lower than the resonance frequency. With the quality factor of 4, the response time is $2.8\mu s$ after calculation with the equations in [23].

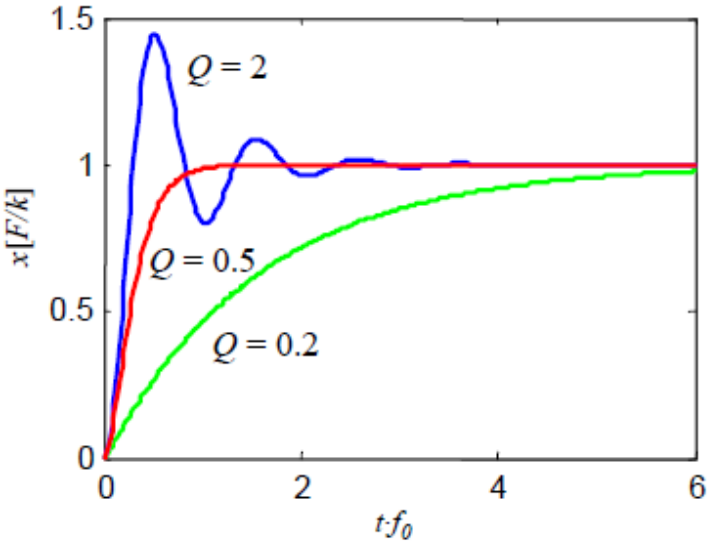

Figure 4.18: Accelerometer step responses for different quality factors [23]

The major mechanical noise is an accelerometer is Brownian noise which is dominated by the squeeze-film damping. For the damped accelerometer, Brownian noise floor is given by [26]:

$$\frac{a}{\sqrt{\Delta f}} = \frac{\sqrt{4k_B T b}}{m} = \sqrt{\frac{4k_B T \omega_r}{mQ}} \tag{4.13}$$

where k_B is Boltzmann constant ($1.38 \cdot 10^{-23}\, J/K$), T is the absolute temperature of

the environment. As equation (4.13) shows, increasing the proof mass can reduce the Brownian noise caused by squeeze-film damping. That is another benefit having a large mass in an accelerometer. In reality, the most commercial accelerometers are equipped with a large mass to increase performance of the devices. Higher quality factors and lower resonance frequencies can also reduce the mechanical noise of an accelerometer as the equation shows. For the designed single-axis lateral capacitive accelerometer, the mechanical noise which sets the limit for the acceleration noise floor, is calculated using equation (4.13) and equals $19\mu G/\sqrt{Hz}$, assuming room temperature (303.15 K) and only Brownian noise with squeeze-film damping effect.

4.3 Lateral & out-of-plane curl

The CMOS-MEMS process described in chapter 2 is used to construct the microstructures in this thesis. One of the benefits with this process is the ability to make thin beams and narrow gaps as it is mentioned in section 2.3.2. An important design issue arises due to the thin beams implemented as multilayer structures in a CMOS-MEMS accelerometer, especially for the comb fingers. The beams curl laterally in-plane because of the misalignment of the metal layers. The lateral curl leads to offset problem which can be seen directly in the output signals. The offset can reduce the performance of the devices. The misalignment between the different metal layers occurs during fabrication of the devices due to the finite precision of the photolithography, as it is shown in figure 4.19. The multilayer beam can be an asymmetric structure after the RIE step, as the figure 4.19 (b) shows. Residual stress difference in the oxide and metal layers causes the beam to bend laterally upon release and the difference in values of the temperature coefficient of expansion (TCE) causes the beams to bend with temperature changes [12]. This lateral curl dependent on different temperature coefficient can be utilized to design MEMS varactors [27]. However, the two lateral curl effects are the major issues in design of the accelerometer in this thesis. One of the solutions is to make tapered beams as it is shown in figure 4.19 (c). This beam design eliminates the oxide sidewall formation even when misalignment between metal layers occurs [28], and thus reduces the lateral curl significantly. Another solution is to use wider beams and wider gaps to reduce lateral curl. To simplify the design of the accelerometers in this thesis, symmetric beams as shown in figure 4.19 (a) is used to form the springs and comb fingers.

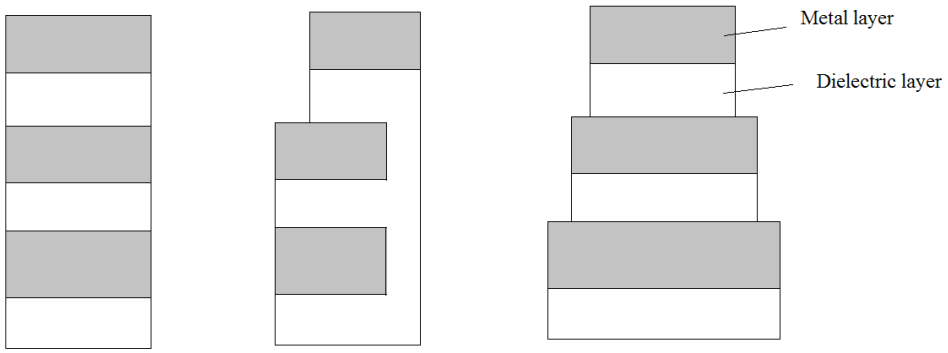

(a) (b) (c)

Figure 4.19: Cross-sections of CMOS-MEMS beams.
(a) Symmetric beam with 3 metal layers; (b) Asymmetric beam; (c) Tapered beam.

Another critical issue in design of the CMOS-MEMS accelerometers is out-of-plane curl. After the final etching step is finished, the MEMS structures are released. Since it is not allowed with high temperature annealing in this CMOS-MEMS process, residual stress within different materials is the major reason for the out-of-plane curl. Due to the build-in residual stress of metal layers and dielectric layers, the composite structures curl vertically, as it is shown in figure 4.20. The vertical curling is also dependent on temperature. The curling gradient varies from run to run. More analysis and modeling of the out-of-plane curl can be found in [29] where the master student uses the curling effect to design MEMS varactors. However, in the design of CMOS-MEMS accelerometers vertical residual stress gradients in the structures can result in a radius of curvature of 1mm ~ 5mm [30]. The out-of-plane curling reduces the sidewall capacitance in capacitive sensing for the accelerometer.

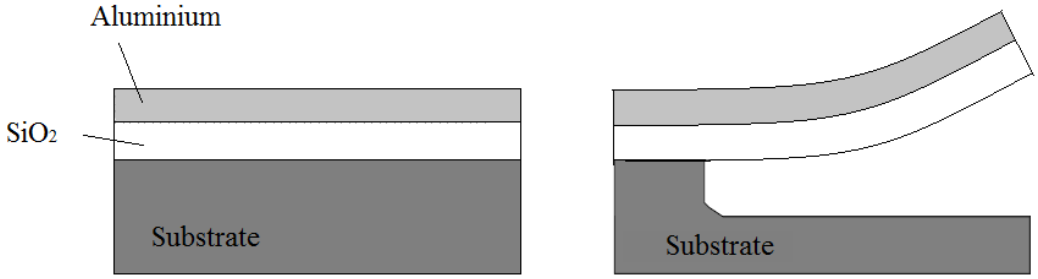

(a) (b)

Figure 4.20: (a) Multilayer beam before release; (b) Curled beam after release.

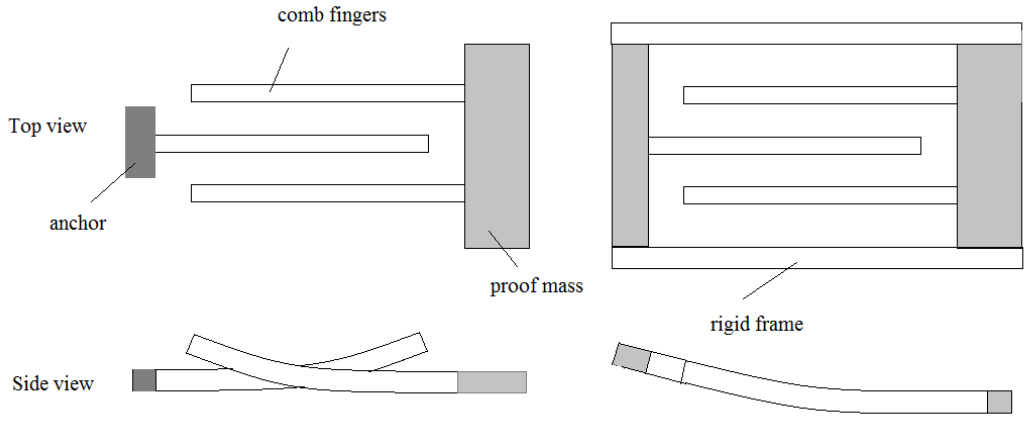

(a) (b)

Figure 4.21: Curl matching technique used for the comb fingers

One of the important methods to reduce the out-of-plane curl is to use a curl compensation frame (rigid frame). Figure 4.21 illustrates the curl matching technique used for the comb fingers. The technique has been used in many of the latest accelerometer designs [18] [31]. Without the compensation frame, the stators are anchored on the substrate and the rotors are attached on the proof mass as it is shown figure 4.21 (a). The comb fingers curl up in opposite directions and the sidewall capacitance is significantly reduced. This mismatching problem can be solved by using a rigid frame anchored properly. The stators are attached to a rigid frame while the rotors are changed on the proof mass, as it is shown in figure 4.21 (b). The rigid frame is anchored along a common-axis with the proof mass and curls up in the same direction as the rotors in order to improve the sidewall, overlapping capacitance.

To have a better matching, a rigid frame has to be designed to suite the other parts of the accelerometer. The layout of the single-axis lateral capacitive accelerometer with the rigid frame is shown in figure 4.22. The inner part of the rigid frame has the same structure as the proof mass, while the outer part has the same structure as the comb fingers. This arrangement eliminates mismatch between the inner and outer part of the structures. The rigid frame is anchored in the middle of the two edges in order to not affect the curl matching. The anchors sustain the whole device, and fix it to the substrate. Further analysis on the curl matching technique is not made due to the difficulty of residual stress modeling and limited knowledge about simulation methods in CoventorWare. For the rigid frame design, it is referred to the latest articles about capacitive accelerometer design [31] [32].

Another method to reduce out-of-plane curl is to use CMOS “ACTIVE” mask covered on the microstructures, and thus the field oxide which has high compressive stress can be removed under CMOS process In the design show in figure 4.22, the “ACTIVE” layer is made on the serpentine springs, the comb fingers and outer edges of the rigid frame.

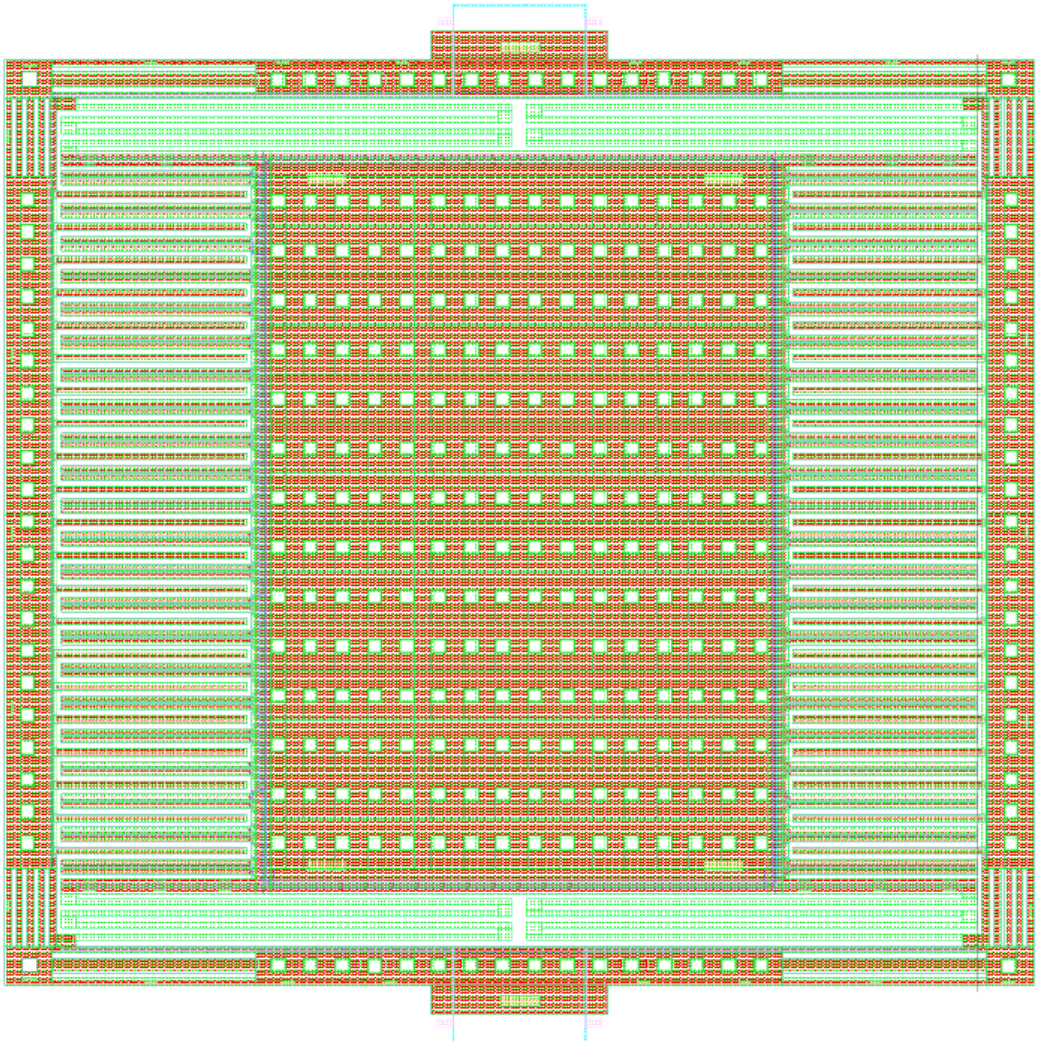

Figure 4.22: Layout of the single-axis lateral capacitive accelerometer (design A)

Chapter 5

Capacitive sensing and self-test actuator, design and modeling

In this chapter, capacitive sensing of the single-axis lateral capacitive accelerometer will be presented. Special comb fingers are designed due to the full differential capacitive topology and the design can be found in section 5.3.3. A capacitive actuator is also designed in order to realize self-testing of the accelerometer. Both the sensing and actuation fingers are based on gap-tuning capacitors. The capacitance between two parallel plates is defined as:

$$C = \frac{\varepsilon A}{g} \tag{5.1}$$

where ε is air permittivity, A is the overlapping area and g is gap between the two plates. By tuning the gap distance, the capacitance between the comb fingers is changed. The output signals are obtained according to the capacitance change caused by displacement of the proof mass, and thus the sensor sensitivity can be obtained. 3D models of the comb fingers are made and simulated in CoventorWare. The simulation models are made without respect for the out-of-plane curl effect on the comb fingers. In other words, the overlapping area between the comb fingers is optimal and the sidewall capacitance is a maximum.

5.1 Full differential capacitive topology

As it is mentioned in chapter 2, the post-CMOS MEMS process can benefit from using a multi-level interconnect between the microstructures. Various methods to implement the routing of the input and output signals can be used to increase sensitivity of the sensor. The multilayer structures give more freedom in the design of the capacitive accelerometers. One of the routing methods is full differential capacitive topology.

The schematic of the design is shown in figure 5.1. To simplify the design, the topology is made symmetrically. The input signals such as modulation voltages (V_m) are led in from one side of the accelerometer through the serpentine springs to the proof mass. The output signals (V_{s+} and V_{s-}) are led out through the rigid frame. The rotors

with input signals are attached to the proof mass while the stators with output signals are anchored to the rigid frame. With this symmetric topology, the parasitic capacitance can be minimized, since the rigid frame has a considerable distance from the substrate and the routed wires are short.

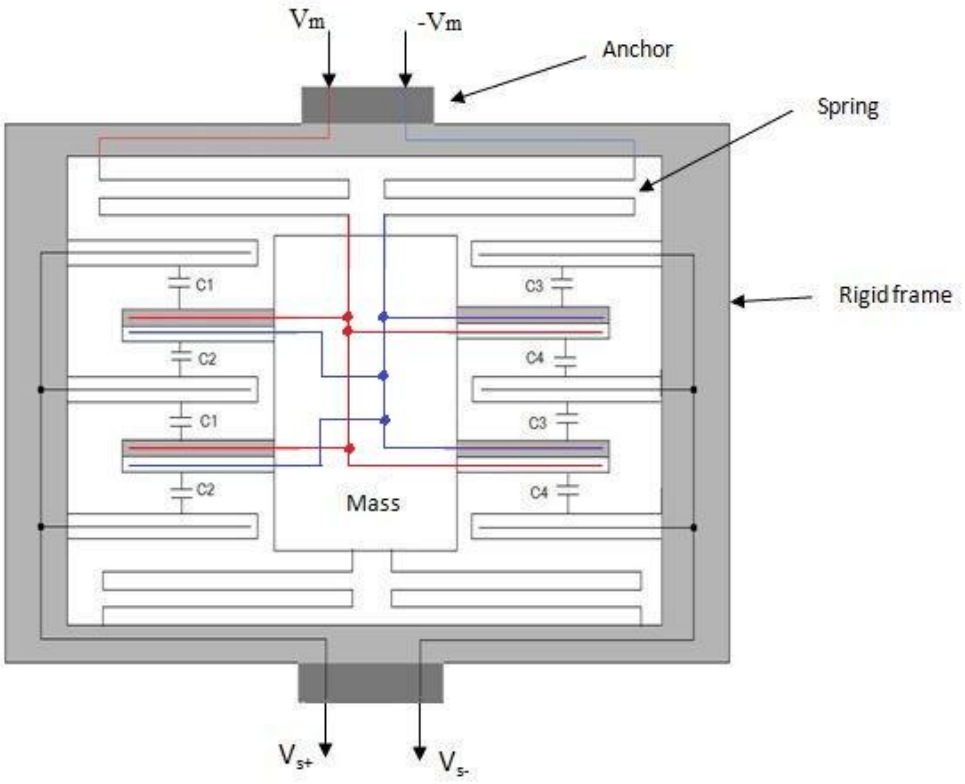

Figure 5.1: Schematic of the full differential capacitive accelerometer

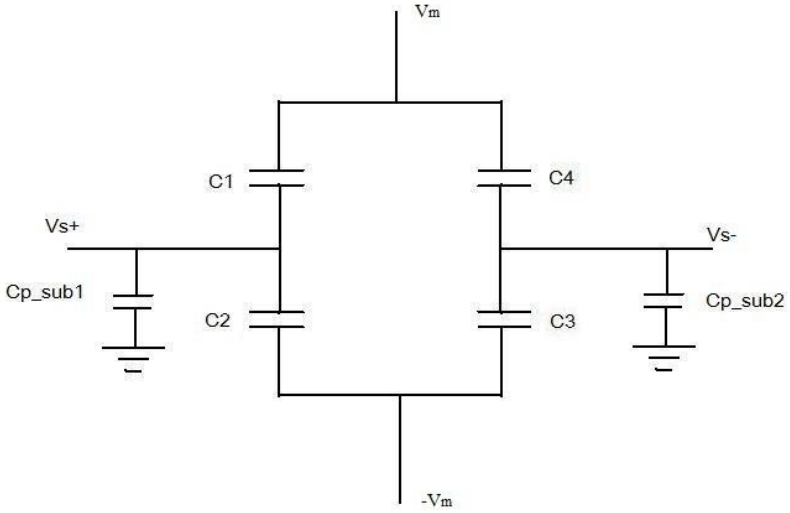

Figure 5.2: Equivalent electrical model for the full differential capacitive topology

An equivalent model for the full differential capacitive topology is shown in figure 5.2.

Based on this electrical circuit, the output voltage ($V_{out} = V_{s+} - V_{s-}$) can be obtained:

$$V_{out} = V_m \cdot \left(\frac{C_1 - C_2}{C_1 + C_2 + C_{p_{sub\,1}}} - \frac{C_4 - C_3}{C_4 + C_3 + C_{p_{sub\,2}}}\right) \tag{5.2}$$

where $C_1 = C_3$ and $C_2 = C_4$. Assume that $C_p = C_{psub\,1} \cong C_{psub\,2}$ is the load parasitic capacitance, and thus the equation (5.2) can be expressed as:

$$V_{out} = 2V_m \cdot \left(\frac{C_1 - C_2}{C_1 + C_2 + C_p}\right) \tag{5.3}$$

When the accelerometer is at rest, C_1 equals to C_2 and the output voltage is zero. As it is shown in equation (5.3), this topology doubles the sensitivity of the half-bridge topology with the same sensing capacitance. A half-bridge topology is that only one pair of the sense capacitors is configured. In most tranditional capacitive accelerometers, the half-bridge topology is utilized due to the single metal structures. A case study of a polysilicon capacitive accelerometer with half-bridge topology can be found in [1].

5.2 Sensor sensitivity

One of the most important specifications for a sensor is sensitivity which is the ratio of a small change in electrical signal due to a small change in the physical signal such as acceleration. Sensor sensitivity for an accelerometer is defined as a change in output voltage for a given acceleration variation ($\Delta V/A$). For the single-axis lateral capacitive accelerometer shown in figure 5.1, no output signals can be found when no acceleration is applied on the proof mass and there is no capacitance change. V_{out} equals to 0 for $C_1 = C_2 = C_0$, according to equation (5.3). C_0 is the capacitance between one stator and one rotor when the accelerometer is at rest, and can be obtained:

$$C_0 = \frac{\varepsilon A}{g_0} = \frac{\varepsilon \cdot L_{eff} \cdot t}{g_0} \tag{5.4}$$

where L_{eff} is the overlapping length between stator and rotor, t is thickness of the structure, the same as for the proof mass, nearly $5.5\mu m$, g_0 is the gap between stator and rotor.

When the rotors are moved toward the stators with a displacement Δx, the capacitance between them is changed as the gap is changed. The capacitance change can be found:

$$\Delta C = C_1 - C_0 = \frac{\varepsilon A}{g_0 - \Delta x} - \frac{\varepsilon A}{g_0} = \frac{\varepsilon A \cdot \Delta x}{g_0 \cdot (g_0 - \Delta x)} \tag{5.5}$$

Assume that $\Delta x \ll g_0$,

$$\Delta C \cong \frac{\varepsilon \cdot A \cdot \Delta x}{g_0^2} = C_0 \cdot \frac{\Delta x}{g_0} \tag{5.6}$$

Then the capacitance change as a function of displacement is obtained:

$$\Delta C / \Delta x = \frac{C_0}{g_0} \tag{5.7}$$

To obtain an approximate linearity of the capacitance change according to the displacement Δx. Figure 5.3 shows comparison between equation (5.5) and equation (5.6) for a variation within $0.2\mu m$ displacement. Δx is smaller than $0.2\mu m$ for a gap of $2\ \mu m$ and the largest difference between equation (5.5) and equation (5.6) can be found at the end of the graphs. In other words, equation (5.5) has a largest nonlinear error within 10% when the displacement is smaller than $0.2\mu m$. Therefore maximum 26G acceleration is assumed to be measured with the accelerometer of design A. The linear measuring range is thereby $\pm$26G which is much smaller than the theoretic measuring range found in section 4.1.

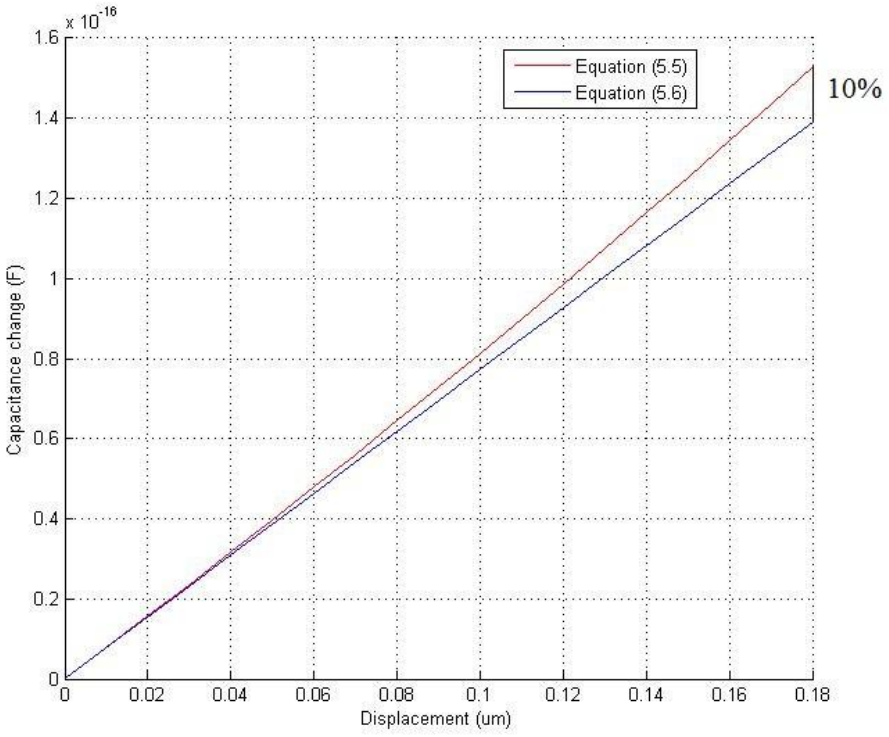

Figure 5.3: Capacitance change as a function of displacement, equation (5.5) vs. equation (5.6)

For larger C_1, C_2 becomes smaller, thus $C_1 = \Delta C + C_s$ and $C_2 = C_s - \Delta C$, and vice versa. For N gaps, $C_s = N \cdot C_0$ is the total capacitance. Equation (5.3) can be expressed

as:

$$V_{out} = \frac{2V_m \cdot \Delta C}{C_s + C_p/2} \tag{5.8}$$

And then the sensor sensitivity can be calculated:

$$\Delta V/A = V_{out}/a_{ext} = \frac{V_{out}}{\Delta C} \cdot \frac{\Delta C}{\Delta x} \cdot \frac{\Delta x}{a_{ext}}$$

$$\Downarrow$$

$$\Delta V/A = \frac{2V_m}{C_s + C_p/2} \cdot \frac{C_s}{g_0} \cdot \frac{1}{\omega_r^2}$$

$$\Downarrow$$

$$\Delta V/A = \frac{2V_m}{1 + C_p/2C_s} \cdot \frac{m}{g_0 \cdot k} \tag{5.9}$$

where $1/\omega_r^2$ is the mechanical sensitivity as it is described in chapter 3 and also equals to m/k. The equation (5.9) shows that the sensor sensitivity is dependent on four parameters: modulation voltage (V_m), the ratio between the parasitic capacitance and 2 times sensing capacitance at rest ($C_p/2C_s$), the gap between comb fingers (g_0) and the mechanical sensitivity which is dependent on the proof mass and spring constant of the serpentine springs. This equation for sensor sensitivity can be also found in [12].

The modulation voltages (input signals) are limited by power supply for the specific application of the sensor. For example, the sensors in WSN which is described in chapter 1, use limited power source in most cases. Increasing the sensitivity by increasing the modulation voltage is not a good choice, with respect to the power consumption.

The sensor sensitivity can be increased by reducing parasitic capacitance and increasing capacitance between the comb fingers. The parasitic capacitance is minimized by using the routing topology described in section 5.1. Therefore, the sensing capacitance C_0 is another critical parameter in tuning the senor sensitivity, besides dimensions of the mechanical structures (springs and proof mass). From the equation (5.4), it is known that smaller g_0 gives larger C_0, and thus higher sensitivity, but the minimum gap is limited by post-CMOS design rules (effective gap > $1.2\mu m$). The other issue is that smaller gap increases the damping coefficient, and thus higher mechanical noise described in section 4.2. Therefore, either the sensor sensitivity or the mechanical noise can be optimized for an accelerometer, dependent on the sensor application, for example, the commercial accelerometers with high-G detection for air bags in cars must be very sensitive to acceleration and has not high requirement for system noise (both mechanical and electronical). More about sensitivity and noise optimization can be found in [33].

5.3 Comb fingers, design and modeling

As it is mentioned in section 5.2, the capacitance C_0 can be adjusted in tuning the sensor sensitivity. Therefore, comb fingers have to be designed for a capacitive accelerometer in order to increase the number of sensing fingers, and thus increase sensitivity. The comb fingers are already shown in the layout in figure 4.22 in chapter 4. It is important to note that the lateral & out-of-plane curling effect is not taken into account in design and modeling of the comb fingers, assuming that the capacitance between the fingers is optimized. More details on comb fingers design are coming in following sections.

5.3.1 Capacitance with fringing field

Equation (5.1) described the capacitance between two parallel plates without consideration of the fringing field. In reality, there is not only electric field normal to the plates, and the field lines at the end of the plates have to be taken into account in calculating the capacitance, as it is shown in figure 5.4. The fringing field effect results in increased capacitance between two parallel plates and also increases the difficulty in calculating the capacitance precisely. A simplified formula can be used to calculate the capacitance and that is given by [34]:

$$C \approx \varepsilon \frac{(t+2g)(L+2g)}{g} \approx \varepsilon\left(\frac{tL}{g} + 2t + 2L\right) \tag{5.10}$$

where t is the structure thickness, g is the gap, L is the overlapping length and ε is air permittivity (8.85×10^{-12} F/m).

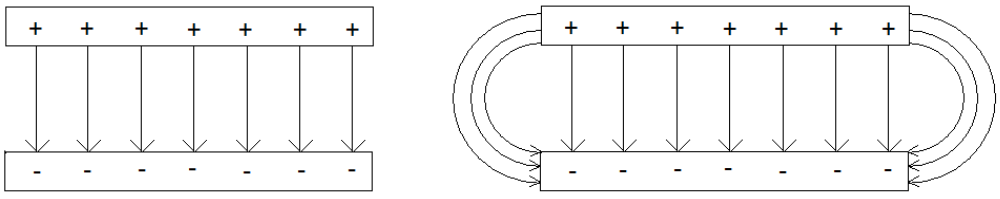

(a) (b)

Figure 5.4: Electric field between two plates (a) without fringing fields; (b) with fringing fields.

5.3.2 Mathematical modeling

Due to the fringing field effect, a mathematical model has to be obtained in calculating

the capacitance between the comb fingers (stators and rotors). Two pairs of the fingers are shown in figure 5.5. The capacitance between one rotor and one stator is C_0 which is the dominant capacitance between two fingers. The other capacitances such as the capacitance between stators and the wires routed in proof mass and rigid frame are relatively small and can be neglected. With fringing field, the approximated capacitance between 2 fingers can be obtained as:

$$C_0 = \varepsilon\left(\frac{tL_{eff}}{g_0} + 2t + 2L_{eff}\right) \tag{5.11}$$

where L_{eff} is the overlapping length between the rotor and the stator, g_0 is the gap between the rotor and the stator at rest. Increasing structure thickness results in increased capacitance, and hence all of the available metal layers listed on table 2.1 are in use to construct the fingers. A great number of the fingers increases the total capacitance, but is limited by device size. The gap between one stator and one rotor, g_0, is the critical parameter in tuning sensor sensitivity and sensor noise as it is mentioned in section 5.2. The designs in this thesis use $2\mu m$ for the gaps in order to give a space for lateral curl of the beams and a maximum displacement for acceleration. The overlapping length L_{eff} is the most flexible parameter for increasing the total capacitance. As equation (5.11) shows, C_0 is linear to the overlapping length. More details on comparison between the mathematical model and the simulation results are covered in section 5.3.5.

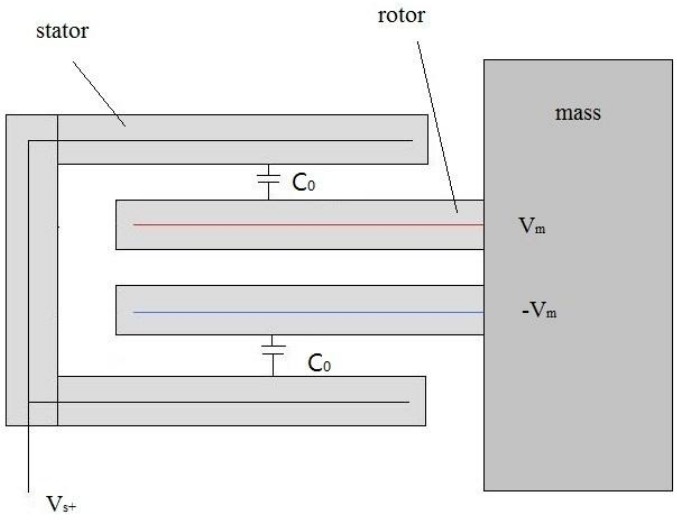

Figure 5.5: Schematic of the capacitances between comb fingers at rest

5.3.3 Comb fingers design

Due to the full differential capacitive topology, specific comb fingers have to be designed. Figure 5.6 shows cross section of the comb fingers with some geometrical

parameters. The fingers are made with four metal layers and one polysilicon layer in order to achieve maximum sidewall capacitance. All of the metal layers are connected together through VIAs (electrical connection between different metal layers) in the dielectric layers (SiO_2). The fingers are designed with symmetric beams as it is described in section 4.3. The rotors shown in figure 5.4 have their own input signals. A special rotor is made by combining the two rotors together, but separated metal layers. The arrangement of metal layers is shown in figure 5.6. One of the benefits with this design is that lateral curl of the beams can be damped. The rotor beams are attached to the proof mass. When an external acceleration is applied to the proof mass and the rotors, the rotors have a bending tendency. The total width of the rotor beam is increased in order to increase its stiffness, and thus damp the bending which can result in reduced performance of the accelerometer. The etched hole between the top metal layers has a width of $0.4\mu m$ and the total beam width is $5\mu m$.

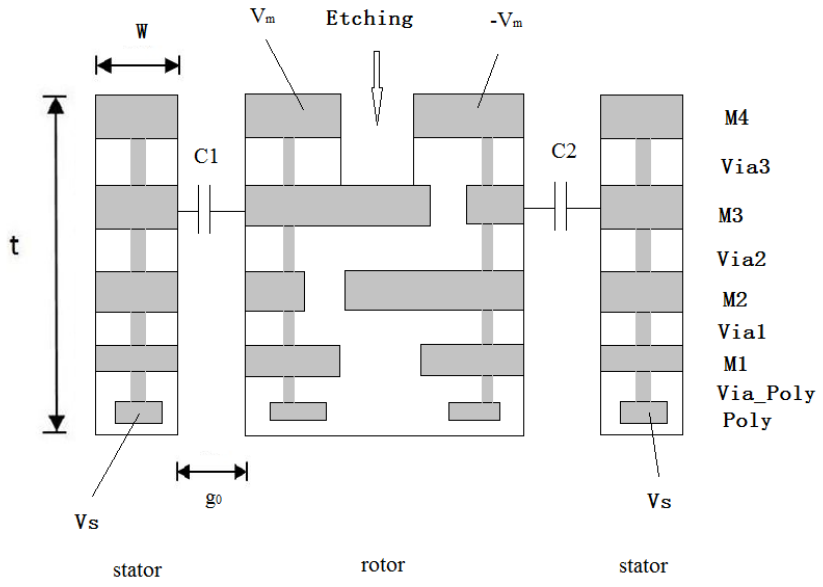

Figure 5.6: Cross section of the comb fingers

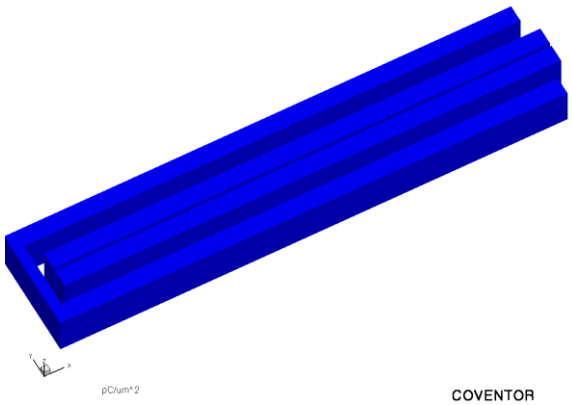

Figure 5.7: Simulation model for 2 pairs of fingers

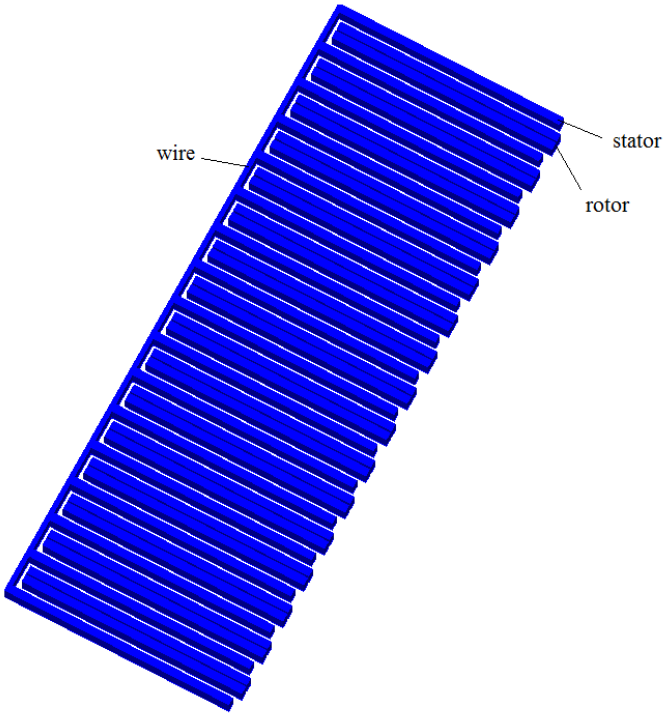

(a)

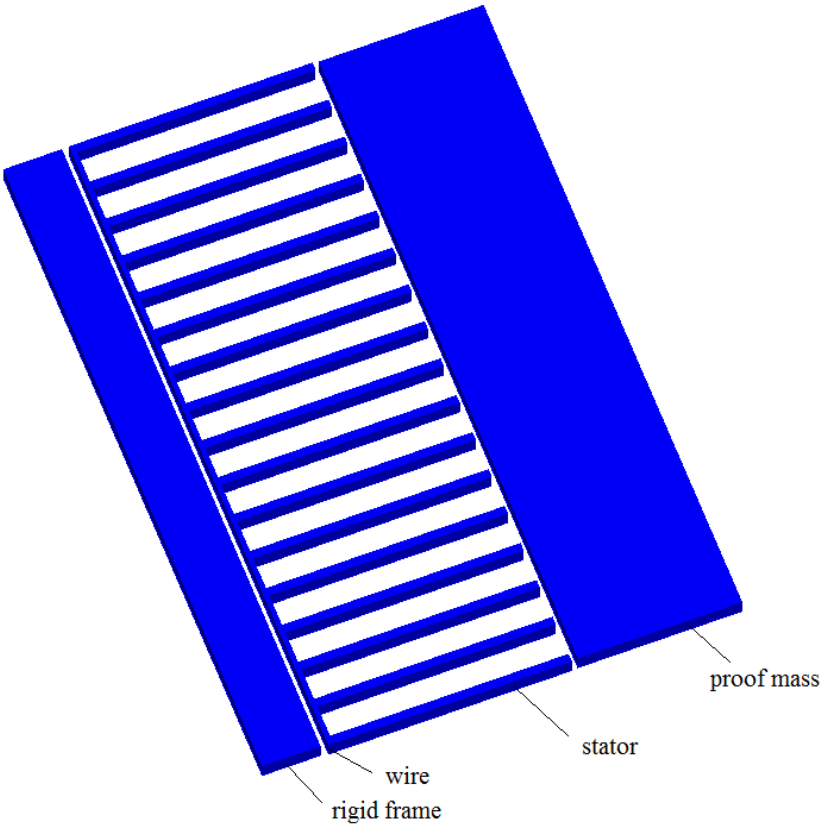

(b)

Figure 5.8: Simulation model for (a) Comb fingers on one side of the proof mass; (b) Parasitic capacitance C_p

5.3.4 Simulation model

A 3D model for 2 pairs of the comb fingers is made in CoventorWare as it is shown in figure 5.7. Note that the rotor is made as two electrodes with a narrow gap between them. The simulation model uses a uniform metal layer instead of multilayer structure in order to save simulation time. The fringing field can fill up the dielectric layers; hence the finger can be seen as one complete electrode. Table 5.1 shows the geometrical parameters used in the simulation and the final design.

A simulation model with all the comb fingers on one side of the proof mass is also made, as it is shown in figure 5.8 (a), where the stators are coupled together with a wire. Figure 5.8 (b) shows the model for simulation of the parasitic capacitance C_p within the structures. The rigid frame and the proof mass are electrical grounded as the substrate. The mechanical structures have a distance of $50\mu m$ from the substrate, therefore the capacitance between the stators and substrate can be neglected. The rigid frame has a separation of nearly $20\mu m$ from the surrounding substrate, and the capacitance between them can also be neglected. The simulation results are described in the following section.

Table 5.1: Geometrical parameters for 3D model and final design

Definition	Symbol	Value
Length of beam	L	$65\mu m$
Overlapping length	L_{eff}	$63.5\mu m$
Gap between fingers	g_0	$2\mu m$
Total thickness of structure	t	$\sim 5.5\mu m$
Number of gaps	N	64

5.3.5 Calculation vs. simulation results

By displacing the rotor in the simulation model shown in figure 5.7, capacitance change can be obtained. The calculation results based on equation (5.6) are compared with simulation results in figure 5.9. As the graphs show, the nonlinearity becomes more significant as the displacement is larger and equation (5.9) for sensor sensitivity is not longer available. In other words, the sensor sensitivity is not linear for larger displacement.

Table 5.2 shows the calculated and simulated values for C_s, C_p and sensor sensitivity. The modulation voltage is set for 1.5V. The total capacitance is calculated based on equation (5.11). By simulating the 3D model in figure 5.8 (a), the total

capacitance is found a little larger than the calculated one. The parasitic capacitance is found by simulation model in figure 5.8 (b), but the value cannot represent the overall parasitic capacitance. If an electronic circuit amplifies the sensor output signals, the input capacitance to the circuit can be found much larger than the routing parasitic capacitance found by the simulation model. The input capacitance is nearly 10 times of the routing parasitic capacitance in [18]. The overall parasitic capacitance can be estimated to be much larger than the parasitic capacitance found from simulation model. Figure 5.10 shows that the sensor sensitivity decreases significantly as larger parasitic capacitance (nearly halved when C_p is 2 times of simulated C_s). The sensor sensitivity is calculated based on equation (5.9).

Table 5.2: Calculated and simulated values for C_s, C_p and sensor sensitivity

Definition	Calculated value	Simulation result
Total capacitance (C_s)	$177fF$	$160fF$
Parasitic capacitance (C_p)	----	$35.1fF$
Sensor sensitivity ($\Delta V/A$)	9.4mV/G	9.3mV/G

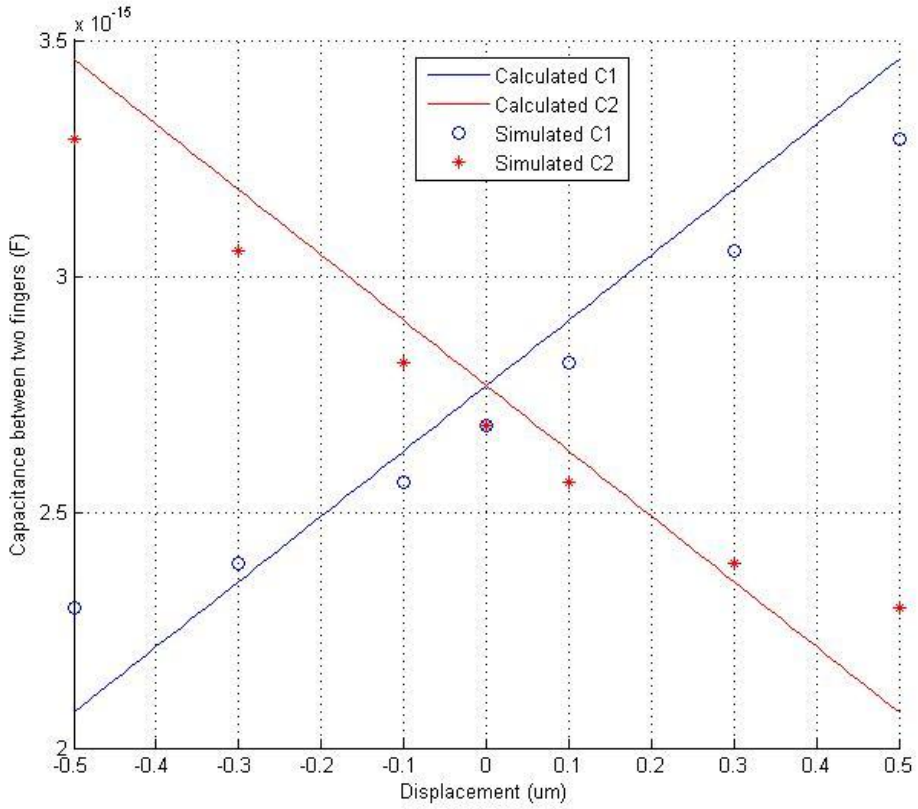

Figure 5.9: Capacitances (C_1 and C_2) as a function of displacement, calculation vs. simulation

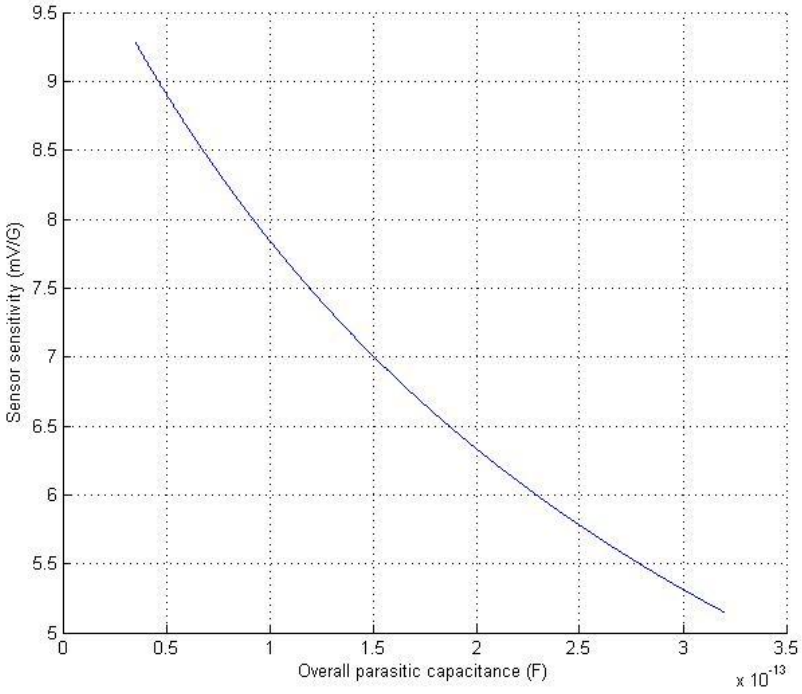

Figure 5.10: Sensor sensitivity as a function of the overall parasitic capacitance

5.4 Self-test actuator

To realize self-test of the accelerometers, actuators are made in the designs in this thesis. The actuators have identical comb fingers as the sensing part and are divided in 4 groups which are settled at the 4 corners of the proof mass. One of the groups is shown in figure 5.11. The actuators are utilizing electrostatic actuation which is based on the attraction of electric charges on the rotors and the stators. The difference from the sensing part is that the stator is routed by actuation voltage (V_a, AC) and the rotors are routed by symmetric biases (V_{dd} & V_{ss}, DC). Between the actuation fingers and the sensing fingers, there is a finger used for shield which can avoid feedthrough of the signals.

The parallel plate capacitors as shown in figure 5.12, have two electrostatic forces (F_1 & F_2) attracting the rotors with V_{dd} & V_{ss}. The electrostatic force between two parallel plates is given by [1]

$$F_e = \frac{\varepsilon A}{2g^2} V^2 \tag{5.12}$$

where ε is air permitivity, A is overlapping area, g is gap between two plates and V is voltage difference between two plates.

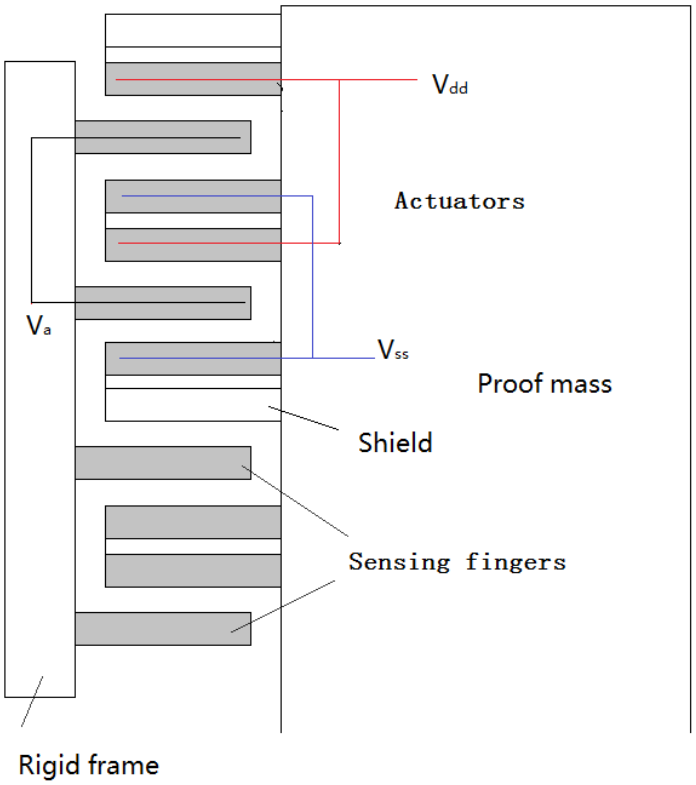

Figure 5.11: Electrostatic actuators (top view)

Based on equation (5.12), a net force can be obtained as:

$$F_{net} = F_1 - F_2 = \frac{C_0}{2g_0}\left[(V_{dd} - V_a)^2 - (V_{ss} - V_a)^2\right] \qquad (5.13)$$

where C_0 can be found by equation (5.11) or obtained from simulation model, g_0 is the gap between fingers at rest and V_{dd} is inverted V_{ss}. The actuation voltage and the symmetric biases can be controlled by an external IC circuits, thus controlling the generated acceleration on the proof mass. For 4 groups of actuators and 4 C_0 for each group, the total force is 16 times of the net force from equation (5.13).

Figure 5.13 shows how the generated acceleration varies as the actuation voltage (V_a) changes between -3V and 3V. The generated acceleration shows a linear relationship to the actuation voltages. For C_0 = 2.7 pF (from simulation model), g_0 = $2\mu m$, V_{dd} = -V_{ss} = 3V and the proof mass m = 0.7 μg, a maximum acceleration of 56G can be generated to measure the single-axis capacitive accelerometer in this thesis. This generated acceleration is larger than the one (26G) found in section 5.2. However, increasing actuation voltage results in larger acceleration for test purposes.

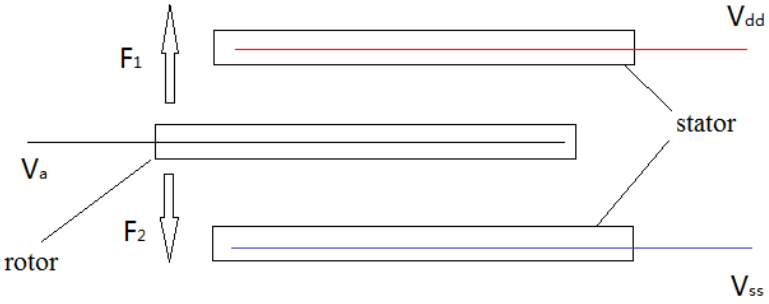

Figure 5.12: Electrostatic actuation

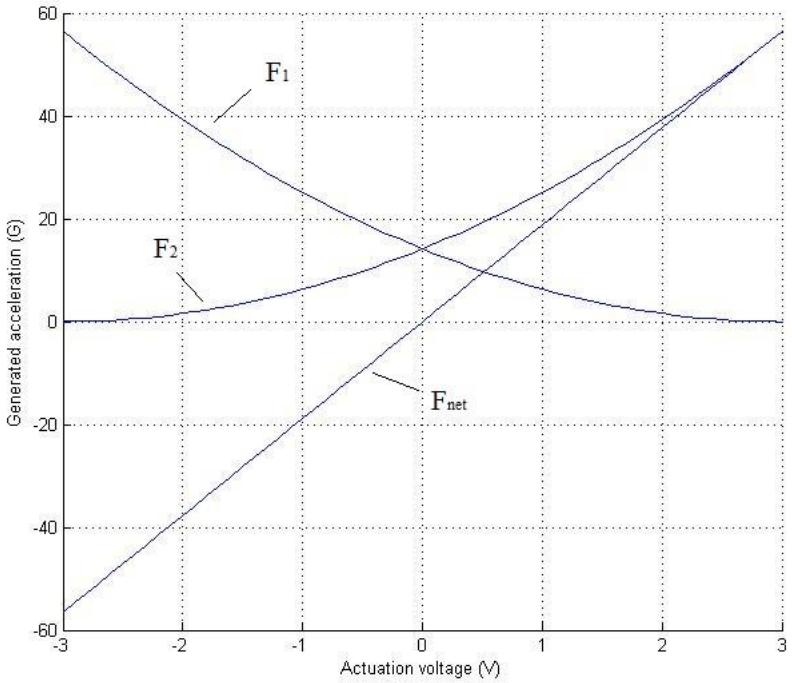

Figure 5.13: The generated acceleration as a function of the actuation voltage

5.5 Implementation

Figure 5.14 shows the layout of the single-axis lateral capacitive accelerometer (design A) and 2 pairs of the comb fingers. The input wires are led into the accelerometer through one of the anchors, the rigid frame, two of the serpentine springs, proof mass. The input and the actuation bias signals are routed in the rotors. The output and the actuation AC signals are routed in the stators and led out through rigid frame and the anchor on the other side of the accelerometer. The output wires are further connected to the bonding pads. The primary geometrical parameters for design A can be found in table 4.3 and table 5.1.

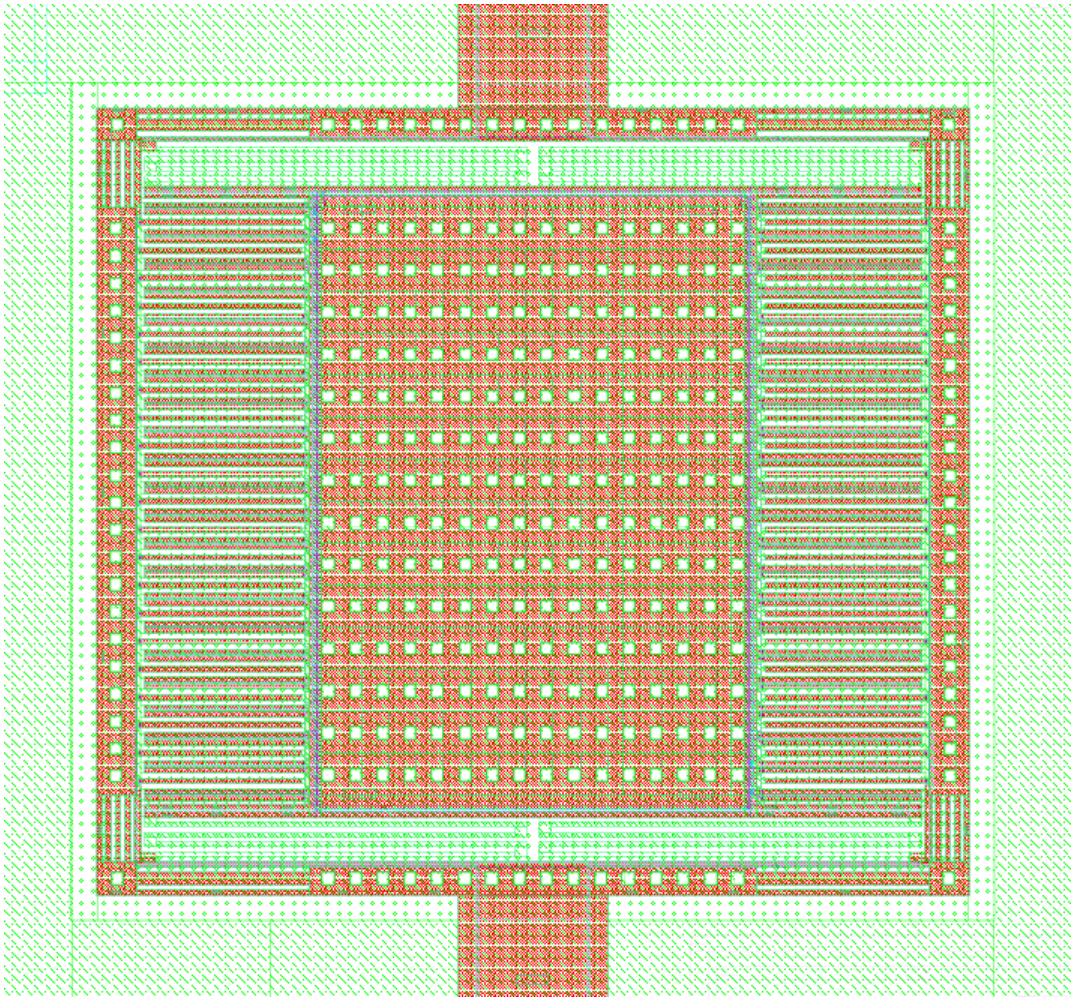

(a)

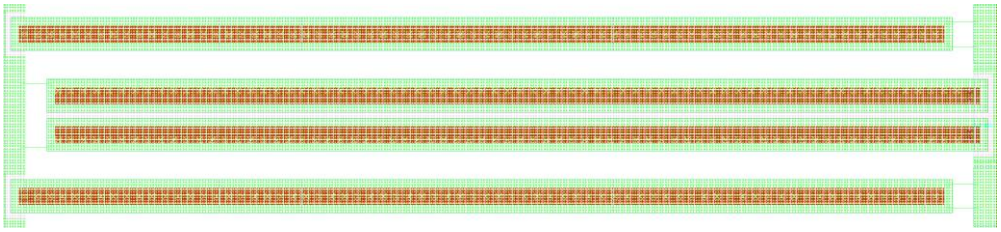

(b)

Figure 5.14: The layout of (a) single-axis lateral capacitive accelerometer (design A); (b) 2 pairs of comb fingers

Chapter 6

Alternative design of a single-axis lateral capacitive accelerometer

In this chapter, another design of a single-axis lateral capacitive accelerometer is presented and referred to as design B. The conventional accelerometer which is similar to design A is compared with the new accelerometer design in [35], where it is shown that the new one has 88% higher sensitivity than the previous one within a same die size. The prospective design based on design A is discussed by modeling and analysis in this chapter. However, the concrete design with a layout in Cadence is not made due to limited size of the experimental chip which will be sent to production.

6.1 Design and modeling

A simplified schematic of the design B is already shown in figure 3.4. The only difference from the design A which is illustrated in figure 3.3 is that the center part of the proof mass is removed and replaced with comb fingers, two supporting springs and an anchor. Therefore, larger sensing capacitance is obtained due to the additional sensing fingers. Figure 6.1 shows the schematic of the inner part of the design B. The routing arrangement is the same as the symmetric topology described in section 5.1. The rotors are attached to the proof mass while the stators are fixed to an anchor in the center. Two supporting springs are made between the proof mass and the anchor for connecting to the output signals (V_{s+} and V_{s-}).

Several problems have to solve in design B, such as increased spring constant due to the two supporting springs and a reduced proof mass. Therefore it requires more analysis of these two parameters and the total sensing capacitance to prove that the design B is feasible.

The same as the previous work for design A, the structure analysis is separated into two parts: spring design and capacitance analysis. They are discussed in the following.

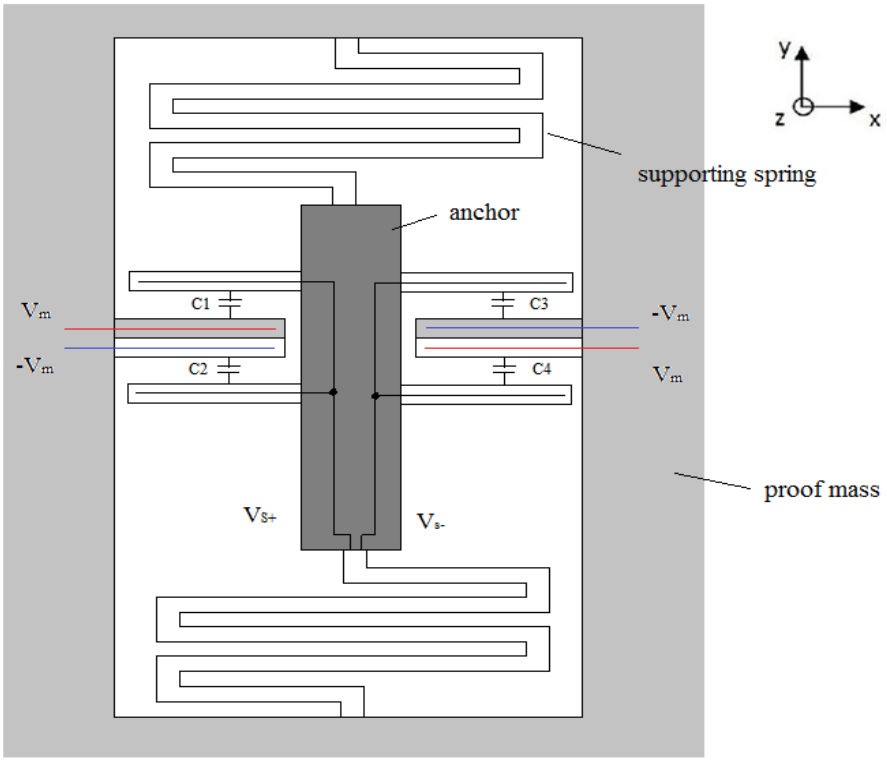

Figure 6.1: Schematic for inner part of the design B

Spring design

The main purpose of the two supporting springs in design B is the routing of the output signals. Thereby, the spring constant in y-direction has to be obtained as small as possible. The spring shown in figure 6.1 can be considered as two short, guided cantilever beams and several long, guided cantilever beams. The short beams are half length of the long beams because of the center attachment. Based on equation (4.6), the spring constant in y-direction for the two supporting springs can be obtained as:

$$k_y = \frac{2E \cdot t}{(\frac{1}{4}+n)} \cdot (\frac{w_l}{l})^3 \qquad (6.1)$$

where t is the thickness of the structure which has 3 metal layers, n is the number of the long beams, w_l is the beam width and l is the long beam length. The parameters involved in equation (6.1) are the same as the serpentine springs described in chapter 4, except the number and the length of long beams. It is no doubt that more and longer beams give smaller spring constant.

However, the supporting springs is limited by the available area which is removed from the proof mass, thereby the geometrical parameter design for the springs is not very flexible. Figure 6.2 shows the 3D simulation model for the two supporting springs with a frame surrounded. The frame is considered as a replacement of the proof mass. By pushing the frame, a maximum displacement (red color) of the springs can be found.

The spring constant found by this model is 0.91N/m and the calculated spring constant is 0.99N/m.

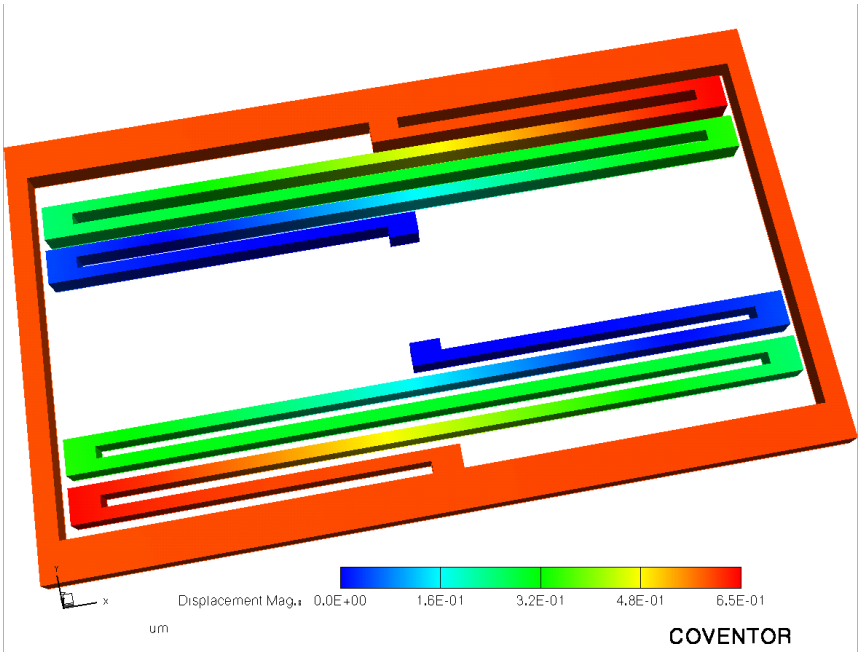

Figure 6.2: 3D simulation model for two supporting springs

Capacitance analysis

Due to the area limitation, the inner comb fingers have to be made shorter than the outer comb fingers (nearly half of the length). It is important to note that all the comb fingers in this thesis are made with the same structure as described in chapter 5. By using equation (5.11), the capacitance with fringing field for the inner comb fingers can also be found. The 3D simulation model is the same as the one in figure 5.7 and 5.8, but with shorter length.

It is estimated that we have 40 gaps for the inner comb fingers. After calculation, the total capacitance is $0.52 \cdot 10^{-13} F$. From the simulation model, the total capacitance is found to be $0.48 \cdot 10^{-13} F$.

6.2 Conclusion

In the design A, the proof mass is found to be $0.7 \mu g$, as shown in table 4.3. After the center part is removed, the proof mass has 20% reduction. The primary parameters in calculating the sensor sensitivity are listed in table 6.1, where the design B is compared with the improved accelerometer from NTHU in Taiwan.

The sensor sensitivity is decreased and the accelerometer is not improved for the design B, while the one from NTHU has significant improved sensor sensitivity. The design B is not feasible to make based on the design A in this thesis. But what is the reason and how it cannot be improved?

In the design from NTHU in Taiwan, the conventional accelerometer have larger proof mass and smaller spring constant than the design A have in this thesis. A large proof mass in the improved accelerometer gives large area which can be removed and replaced with springs and comb fingers. Therefore, the extra supporting springs can be designed to be more compliant. The mass to spring stiffness ratio (m/k) is not decreased so much in comparison with the previous accelerometer. More comb fingers with the same structures can be made to increase the total sensing capacitance. A picture of the improved capacitive accelerometer from NTHU is shown in figure 6.3, where the sensing capacitance is increased 80% and the proof mass is decreased by 20% [35]. The parasitic capacitance (C_p) includes the wires, the structures and the input capacitance to the electrical circuits. C_p is simulated to be much larger than the sensing capacitance (almost 3 times of the sensing capacitance). Increasing the sensing capacitance can result in obvious change in the ratio between parasitic capacitance and the sensing capacitance ($C_p/2C_s$), and thus the sensor sensitivity changes based on equation (5.9). That is also the reason for significant improvement on the sensor sensitivity for the capacitive accelerometer from NTHU.

For the new design (design B) in this thesis, the existing accelerometer (design A) has not such a large proof mass as the one from NTHU has, and hence the removed area is very limited. The spring stiffness (four serpentine springs and two supporting springs) is nearly doubled while the spring constant in design A is 0.9N/m. Comb fingers with only half length of the fingers can be made. The total sensing capacitance is only increased by 30% and the proof mass is decreased by 20%. With the same parasitic capacitance, gap between fingers and modulation voltage, the sensor sensitivity for design B is decreased obviously.

To solve this problem, the previous accelerometer (design A) has to be adjusted by a larger proof mass in order to increase design space for more compliant springs and higher sensing capacitance. It is important to note that the new design is based on increasing total sensing capacitance, so that increasing the number of the comb fingers is the key factor in an improved capacitive accelerometer.

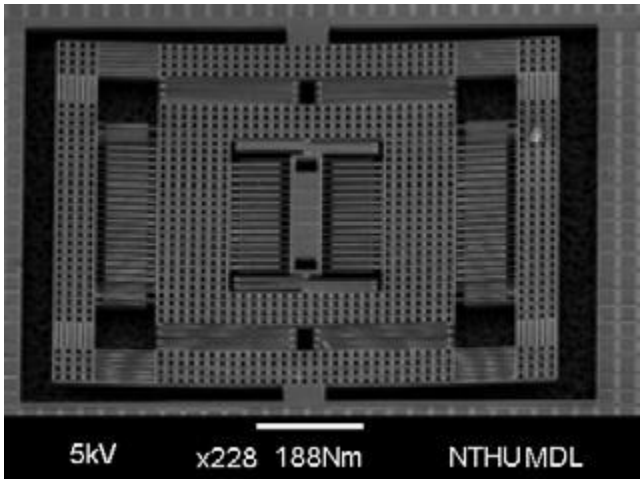

Figure 6.3: The SEM photo of the improved capacitive accelerometer [35]

Table 6.1: The design B vs. the improved accelerometer from NTHU

Definition	Design B	Improved accelerometer from NTHU
Acclerometer size	$325\mu m \times 355\mu m$	$440\mu m \times 490\mu m$
Proof mass	$0.5\mu g$	$0.85\mu g$
Spring stiffness	$1.8N/m$	$0.98N/m$
Sensing capacitance	$208fF$	$112.2fF$
Parasitic capacitance	$35.1fF$	$300fF$
Gap	$2\mu m$	$1.5\mu m$
Modulation voltage	1.5V	1V
Sensor sensitivity	3.7mV/G (calculated)	3.95mV/G (measured)
Sensor sensitivity from previous work	9.3mV/G (calculated)	2.1mV/G (measured)

Chapter 7

Dual-axis in-plane capacitive accelerometer

In this chapter, a dual-axis in-plane capacitive accelerometer is presented. By integrating two single-axis lateral capacitive accelerometers, the dual-axis accelerometer can be realized. Compared with a system with two separated single-axis accelerometers which measure acceleration in two directions, the total die size is minimized by the integration. This design is implemented in Cadence.

7.1 Design and analysis

The primary design concept with dual-axis in-plane capacitive accelerometer is to utilize a single-axis lateral capacitive accelerometer as a large proof mass and add comb fingers, springs and a compensation frame surround the proof mass, as it is shown in figure 7.1. The outer accelerometer detects the acceleration in y-direction while the inner accelerometer is implemented to detect movement in x-direction. Both accelerometers are operated in measuring the capacitance change, and thus the acceleration. Thereby, the dual-axis in-plane capacitive accelerometer can be realized in this way.

The main challenge for this design is the influences between two different directional movements of the inner and outer accelerometers (x-direction and y-direction motions). For example, when the proof mass in the center has a motion in x-direction, the inner rigid frame also moves in the same direction due to acceleration. The outer serpentine springs sustained the inner rigid frame are not absolute rigid in x-direction, so that the inner rigid frame can be slightly displaced in x-direction. That can result in additional signal in the output of the inner accelerometer in operation.

The additional signal problem can be solved by spring design. For example, for the outer accelerometer which detects acceleration in y-direction, increasing stiffness of the serpentine springs in x-direction can minimize influence on the motion of the inner rigid frame in x-direction. The designed dual-axis capacitive accelerometer in this thesis uses the single-axis accelerometer described in chapter 4 and 5 as a large proof mass with the same size of the comb fingers and springs. It is necessary to study more closely the spring constant in x-direction of the serpentine spring shown in figure 4.4.

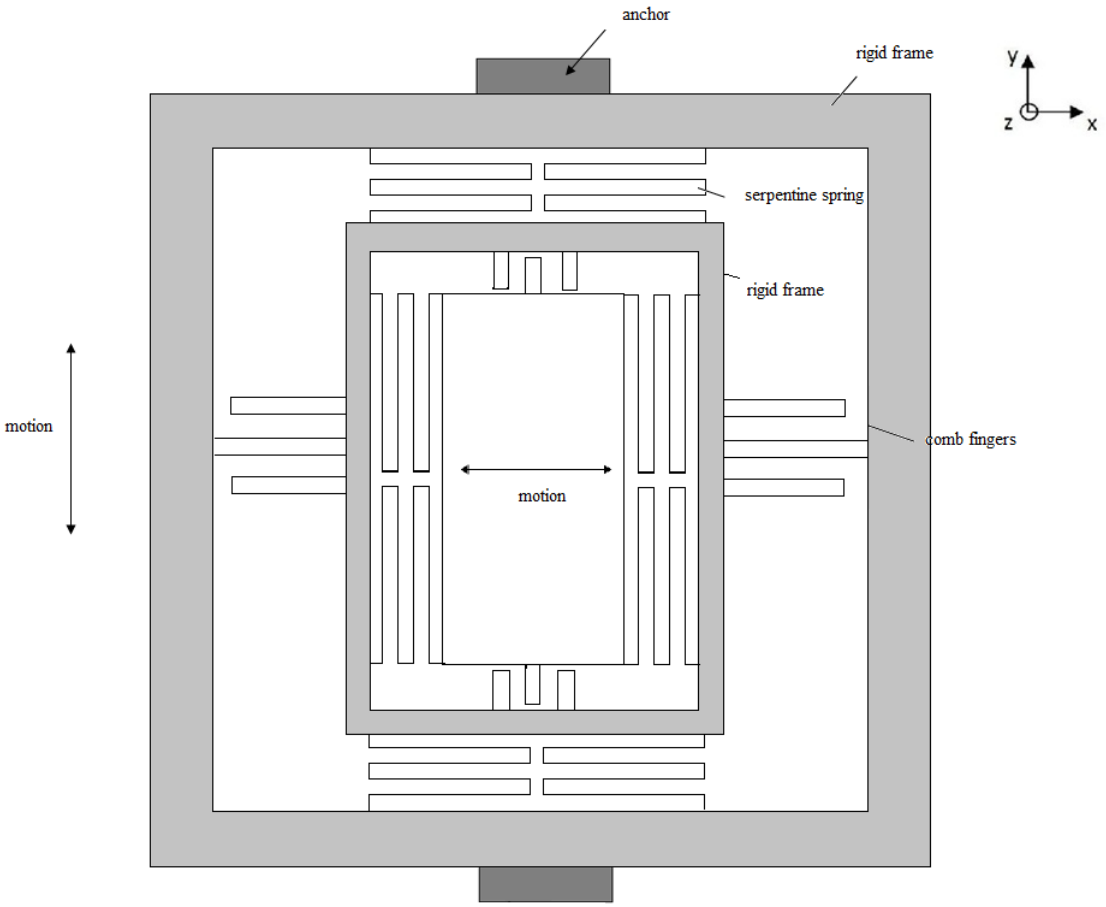

Figure 7.1: Simplified schematic of a dual-axis in-plane capacitive accelerometer

Spring analysis

The spring constant of one serpentine spring in x-direction is given by [21]:

$$k_x = \frac{12EI_{zl}}{d^2 n[(\tilde{c}^2+l)\cdot n^2-3l\cdot n+2l]} \tag{7.1}$$

where all the parameters are described in model 3 in section 4.1.2. For $\tilde{c} \ll l$, equation (7.1) can be simplified as:

$$k_x = \frac{Etw_l^3}{d^2 l\cdot n\cdot(n-1)\cdot(n-2)} \tag{7.2}$$

and then the ratio between the spring constant in y-direction from equation (4.11) and in x-direction can be obtained as:

$$Ratio_{k_y,k_x} = \frac{k_y}{k_x} = n\cdot(n-2)\cdot\left(\frac{d}{l}\right)^2 \tag{7.3}$$

where n is the number of turns, d is the short beam length, l is the long beam length. Equation (7.3) shows that the ratio between k_y and k_x is dependent on the ratio between short beam length and long beam length when n is constant. $Ratio_{k_y,k_x}$ should be kept as low as possible, which also means that the spring constant in x-direction should be much larger than the one in y-direction. To obtain a low $Ratio_{k_y,k_x}$, the short beam length is the critical parameter. As it is discussed in section 4.1.2, the spring constant in y-direction is almost unchanged for various lengths of the short beam. For a smaller d, the spring constant in x-direction is larger, and $Ratio_{k_y,k_x}$ is smaller. This is respectively shown in figure 7.2(a) and figure 7.2(b).

However, the number of turns can also determine $Ratio_{k_y,k_x}$ and is supposed to be small, but smaller n gives larger k_y as it is discussed in section 4.1.2. Therefore, this parameter is not flexible in tuning the spring constants and the ratio.

In this design, the outer accelerometer has serpentine springs with 4 metal layers due to the routing arrangement shown in figure 7.3. The signal definitions are listed in table 8.2. The springs are a little thicker and have a higher average Young's modulus than the springs in the inner accelerometer have, because the metal layer with tungsten has much higher Young's modulus than aluminum, as it is shown in table 2.1 in chapter 2. Therefore, the spring constants of the serpentine springs both in y-direction and x-direction are larger in the outer accelerometer than in the inner accelerometer.

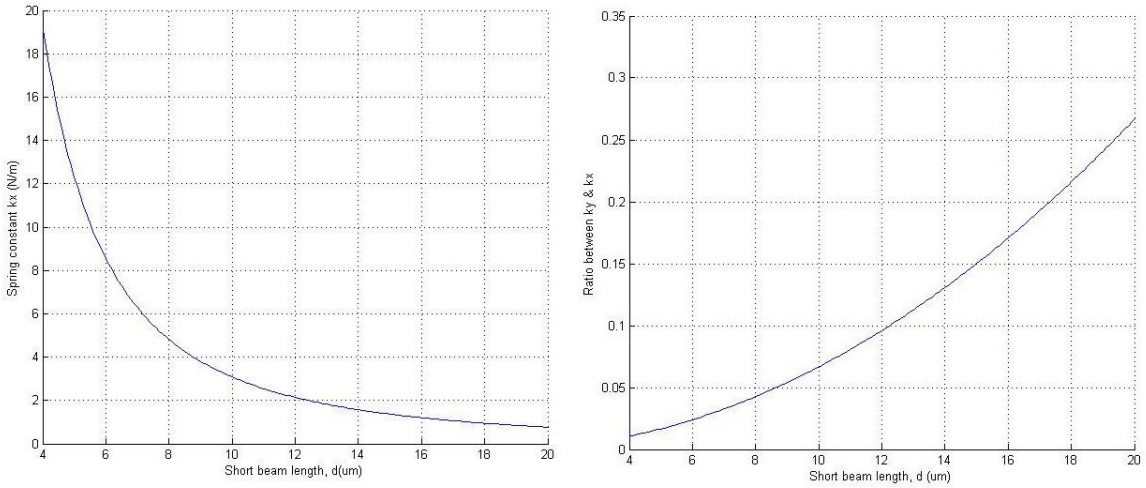

(a) (b)

Figure 7.2: (a) Spring constant k_x as a function of short beam length, d;

(b) $Ratio_{k_y,k_x}$ as a function of short beam length.

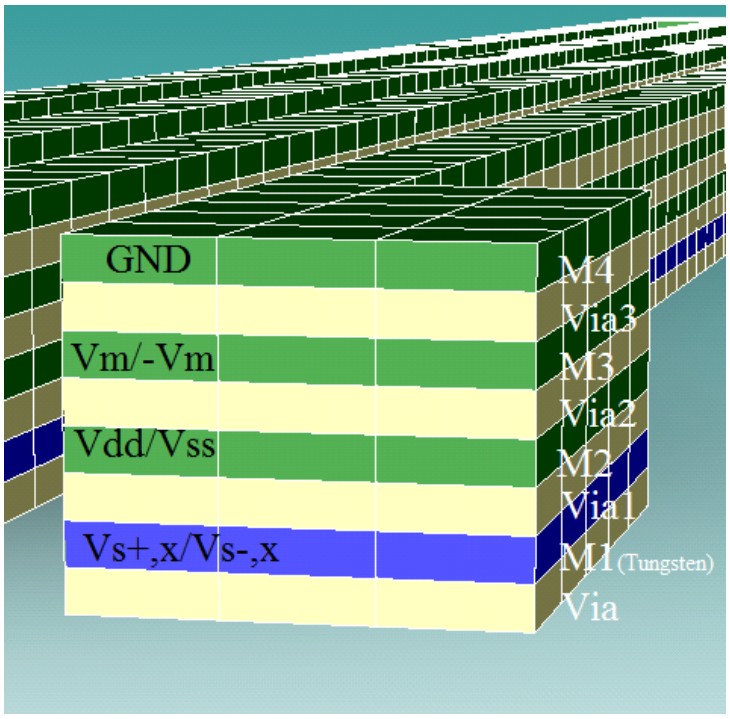

Figure 7.3: Cross section of the spring in the outer accelerometer

Capacitance analysis

The outer accelerometer which detects acceleration in y-axis has 60 gaps between comb fingers and 4 groups of actuators with 2 gaps for each actuator. The comb fingers have the same structures as those in the inner accelerometer. With 60 gaps, the total sensing capacitance C_s can be obtained by equation (5.11) to be 166fF. By using the same simulation model as in figure 5.7, C_s can be found to be 150fF.

The actuators have totally 8 gaps while the actuators in the inner accelerometer have 16 gaps. In other words, the actuators can generate maximum 32G acceleration for the outer accelerometer.

Conclusion

All of the important parameters for the outer accelerometer and the calculated sensor sensitivity are listed in table 7.1, where only the geometrical parameters different from the previous ones are shown. The other unchanged geometrical parameters for springs and comb fingers are listed in table 4.3 and table 5.1 respectively. The estimated proof mass for the outer accelerometer is the total mass of the inner accelerometer plus the inner rigid frame. Based on the simulation results, the sensor sensitivity for the outer accelerometer can be calculated by using modulation voltage of 1.5V.

The ratio between k_y and k_x for the serpentine springs can also be expressed as:

$$Ratio_{k_y,k_x} = \frac{k_y}{k_x} = \left(\frac{m}{Sens_y}\right)/\left(\frac{m}{Sens_x}\right) = \frac{Sens_x}{Sens_y} \qquad (7.4)$$

where $Sens_y$ and $Sens_x$ are the mechanical sensitivity in y-direction and in x-direction respectively for one accelerometer. The mechanical sensitivity is expressed as the mass to stiffness ratio (m/k). $Sens_y$ is obtained as 8.3nm/G and $Sens_x$ equals 0.08nm/G. In other words, when 1 G acceleration is applied to the inner accelerometer (proof mass for the outer accelerometer), the inner rigid frame has a displacement of 0.08nm in x-direction that can influence the inner accelerometer in operation. The additional displacement can be interpreted as an extra signal to the output of the inner accelerometer. The extra signal can reduce the performance of the inner accelerometer. The ratio is controlled within 0.01 so that the displacement of 0.08nm in x-direction can be ignored.

In the other hand, when the outer accelerometer is in operation, the inner accelerometer acts as a large proof mass, but it is not absolute rigid. That can also cause an additional signal in the output of the outer accelerometer. After analysis, the x-directional spring constant of the inner serpentine springs is large enough to keep the center proof mass in a relative steady state. The influence on the outer accelerometer is small.

Table 7.1: Important parameters and sensor sensitivity for the outer accelerometer

Definition	Symbol	Value
Thickness of the springs	t	~5μm
Average Young's modulus	E	116GPa
Spring constant in y-direction	k_y	1.36N/m (calculated) 1.30N/m (simulated)
Spring constant in x-direction	k_x	128.8N/m (calculated) 132.1N/m (simulated)
Ratio between k_y and k_x	$Ratio_{k_y,k_x}$	0.01
Number of gaps	N	60
Sensing capacitance	C_s	166fF (calculated) 150fF (simulated)
Estimated proof mass	m	~1.1μg
Sensor sensitivity	$\Delta V/A$	11.1mV/G

7.2 Implementation

Figure 7.4 shows the layout of the dual-axis in-plane capacitive accelerometer. A compensation frame is also made for the outer accelerometer in order to reduce the mismatch between rotors and stators due to out-of-plane curl. In order to not affect the inner rigid frame, the comb fingers are attached on the center part of the rigid frame and the actuators are fixed to the outer part of the rigid frame. Note that there are not connection beams made for the outer accelerometer, while the inner accelerometer has connection beams between the serpentine springs and the proof mass.

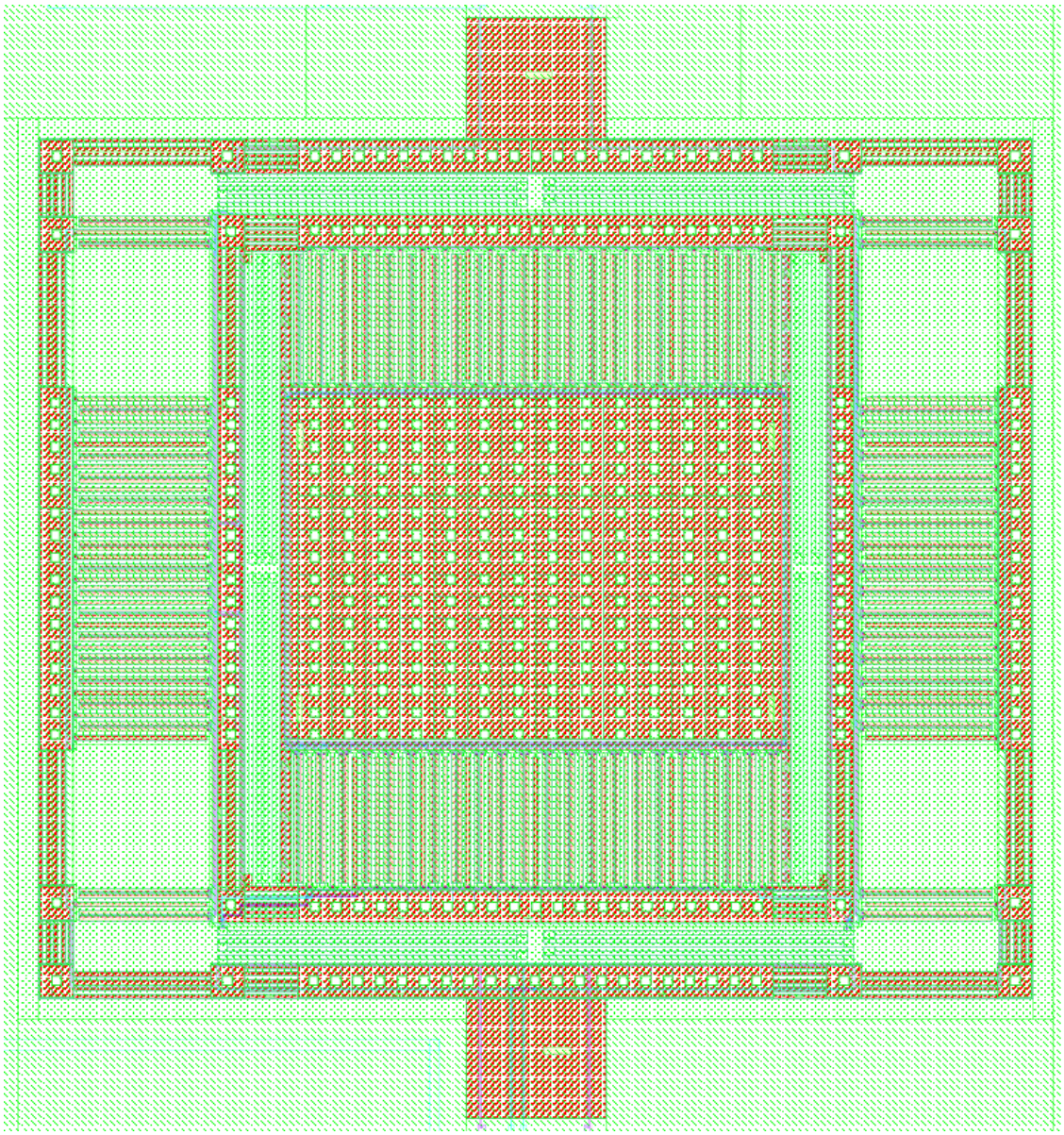

Figure 7.4: The layout of the dual-axis in-plane capacitive accelerometer

Chapter 8

Summary & discussion

In this chapter, the achieved results from both the single- and dual-axis lateral capacitive accelerometers are summarized and compared to other works. The layout of the designs is implemented in Cadence and the die layout is shown in section 8.2. The proposed improvement of the designs is discussed at the end of this chapter.

8.1 Short summary and comparison with other works

This thesis is emphasized on the design of a single-axis lateral capacitive accelerometer (design A). An alternative design of the single-axis lateral capacitive accelerometer (design B) based on modification of design A is analyzed and discussed in chapter 6. A dual-axis in-plane capacitive accelerometer by integrating two single-axis lateral capacitive accelerometers is explained in chapter 7.

The design of the single-axis lateral capacitive accelerometer is divided in two main parts: the mechanical structure design in chapter 4 and the capacitive sensing in chapter 5. In addition to the accelerometers, self-test actuators based on electrostatic actuation are designed in order to realize self-testing of the accelerometers (both single-axis and dual-axis) on the chip.

The mechanical part includes springs, a proof mass and a compensation frame (rigid frame). The spring design in chapter 4 is the most important section in the mechanical structure design in this thesis. The four serpentine springs sustain the proof mass. The main goal is to obtain a small spring constant of the springs in sensing direction. Various parameters involved in the spring design are analyzed by mathematical and simulation models in section 4.1. The mathematical model 1 gives simple description of one serpentine spring. The mathematical model 2 and 3 can explain how the different geometrical parameters influence the spring constant in sensing direction when the serpentine springs are corner attached to the proof mass. The model 2 is the simplified model 3 and 4 times of the model 1. The simulation model in figure 4.12 is built to verify the calculated results from the mathematical models. After the design parameters are obtained, the 3D simulation model for the springs and the proof mass is made and the mechanical sensitivity (m/k) can be found.

The springs

The primary design parameters for the serpentine spring (figure 4.4) and their effects on the spring constant in sensing direction are summarized in the following:

- **The long beam length –** Increased length gives a smaller spring constant (figure 4.8 and 4.13).
- **The long beam width –** Increased width gives a larger spring constant (figure 4.7 and 4.13).
- **The short beam length –** Increased length gives no obvious effect on the spring constant (figure 4.11 and table 4.1).
- **The short beam width –** Increased width gives no obvious effect on the spring constant when the short beam length is larger than $5\mu m$ (figure 4.10 and table 4.1).
- **The number of turns –** More turns or more number of the long beams give a smaller spring constant (figure 4.9 and 4.13).
- **Thickness of the beams –** Increased thickness gives a larger spring constant according to the mathematical models.
- **Beams with multilayer structures –** Design A uses springs with three metal layers (Al), while the outer accelerometer in the dual-axis accelerometer uses springs with four metal layers (Al + tungsten as the first metal layer). Tungsten has much larger Young's modulus than aluminum has and the thickness is also increased. Therefore, the springs for the outer accelerometer are stiffer than the ones in design A. The inner accelerometer is the same as design A.

The proof mass

The size of the proof mass is determined by the serpentine springs' length, the number and the width of the comb fingers. Larger mass gives higher mechanical sensitivity, then higher sensor sensitivity according to equation (5.9). On the other hand, the mechanical noise is increased when the proof mass is heavier, according to equation (4.13).

Lateral & out-of-plane curl

The curling problems are the main challenges for CMOS-MEMS design due to the thin film multilayer structures and the fabrication variation explained in section 4.3. The beams are made symmetrically, but they could be made as tapers shown in figure 4.19 for reducing lateral curl. The compensation frame is constructed to reduce out-of-plane curl of the comb fingers. The out-of-plane curl can reduce sidewall, overlapping capacitance between the comb fingers.

Capacitance sensing

The capacitive sensing is based on the full differential capacitive topology (section 5.1) and the special comb fingers design (section 5.3). The mathematical and the simulation models in section 5.3 are used to find the sensing capacitance and the parasitic

capacitance within the wires and structures.

Actuators

The actuators use the same comb finger structures as in the capacitive sensing part. The actuators for design A can generate maximum 56G acceleration which is larger than the linear measuring range of 26G for design A. The actuators can be controlled by actuation voltages.

Sensor sensitivity vs. mechanical noise

As mentioned, the proof mass is one of the primary parameters in optimizing either the sensor sensitivity or the mechanical noise of the accelerometers. Another important parameter is the gaps between the comb fingers. The considerable number of gaps determines the squeeze film damping between the comb fingers according to equation (4.12). Smaller gap gives higher squeezing film damping coefficient, thus higher Brownian noise floor. The choice between the sensor sensitivity and the mechanical noise optimizations is dependent on the application of the accelerometers.

Basic performance of the single-axis lateral capacitive accelerometer (design A)

The design parameters for the single-axis lateral capacitive accelerometer (design A) are listed in table 4.3 and table 5.1. The obtained results for design A are summarized in table 8.1, where design A is also compared to the CMOS-MEMS accelerometers from other publications [18] [32]. However, the designed chip has not been sent to production for some reasons, so the accelerometers are not measured for this thesis. Therefore, only calculated and simulated results are listed in table 8.1, while the other two accelerometers are listed with measured results.

As it is shown in table 8.1, the sensing capacitance of the design A is calculated without respect to the out-of-plane curling effect, while the other two are measured results. The parasitic capacitance is simulated with the 3D simulation model in figure 5.8 that cannot represent the total parasitic capacitance precisely when an electronic circuit is coupled to the sensor. In most publications, the measured parasitic capacitance is always larger than the sensing capacitance due to the CMOS amplifier circuit which has high input parasitic capacitance. As larger parasitic capacitance is found, the sensor sensitivity is reduced according to equation (5.9) and figure 5.10. One of the solutions to minimize the parasitic capacitance is to use symmetric capacitive topology described in section 5.1.

It is difficult to compare the sensor sensitivity for the design A with the ones from other works, because the sensor sensitivity is also dependent on the modulation voltage used to the accelerometers and the gap between the comb fingers.

Based on my assumption to the properly measuring results of design A, the performance of the design A could be reduced. The reasons are in the following:

- The lateral curl of the serpentine springs causes mechanical offset problem.

- The curling problem could reduce the spring constant in sensing direction, but it needs to be proved further.
- Damping coefficient is larger than the calculated one, and thus the mechanical noise level is increased.
- The parasitic capacitance is measured to be larger than the simulated one.
- The sensing capacitance is reduced due to the mismatch of the comb fingers.
- The gaps between the comb fingers cannot be the same everywhere due to the lateral curl and the finite precision under fabrication. The lateral curl can also cause offset problem in the capacitive sensing and its output signals.

Table 8.1: Design A vs. the other single-axis lateral capacitive accelerometers

Definition	Design A	Hao Luo et al.	Gang Zhang
Spring constant	0.9N/m (simulated)	1.77N/m	1.0N/m
Proof mass	$0.7\mu g$	$0.57\mu g$	$0.36\mu g$
Mechanical sensitivity	7.71nm/G	3.1nm/G	3.5nm/G
Resonance frequency	5.68kHz	8.9kHz	8.5kHz
Q factor	4	24	8
Noise floor	$19\ \mu G/\sqrt{Hz}$	$6.9\ \mu G/\sqrt{Hz}$	$50\ \mu G/\sqrt{Hz}$
Sensing capacitance	160fF (simulated)	64fF	60fF
Parasitic capacitance	35.1fF (simulated)	120fF	74fF
Linear range	$\pm$26G	$\pm$13G	$-$
Modulation voltage	1.5V	2V	1V
Sensor sensitivity	9.3mV/G	2.2mV/G	1.5mV/G

Design B

The design B is completely based on the modification of design A, namely the center part of the proof mass is replaced with additional comb fingers and springs. The design parameters and results are listed in table 6.1, where they are compared to an improved accelerometer from NTHU. The results show that the design B has no improvement on the sensor sensitivity due to a limited design area. Therefore, the design A has to be modified in order to make an improved accelerometer based on design B.

Dual-axis in-plane capacitive accelerometer

The major challenge in the design is the influences between two different directional movements of the inner and the outer accelerometers. The solution is increasing the spring constant in x-direction of the serpentine springs while y-direction is the sensing direction. Increased spring constant in x-direction can reduce the displacement of the inner rigid frame, and then reduce the influence to the inner accelerometer in detection. The obtained results show that the spring constant in x-direction is quite large so that the displacement in affecting the inner accelerometer can be ignored. In the other hand, the movement of the inner accelerometer has also small influence on the outer accelerometer after analysis. But the influences have to be proved with measuring results.

The inner accelerometer has sensor sensitivity of 9.3mV/G, while the outer accelerometer has sensor sensitivity of 11.1mV/G.

8.2 Implementation

The layout of the experimental chip with two accelerometers and bonding pads is shown in figure 8.1. The single-axis lateral capacitive accelerometer has a size of $325\mu m \times 355\mu m$, while the dual-axis in-plane capacitive accelerometer has a size of $440\mu m \times 550\mu m$. The accelerometers take half a part of the chip, while the rest of the chip is used for another project. The input and output wires are coupled to 13 bonding pads and the signal definitions are listed in table 8.2.

Table 8.2: Signal definitions on the chip

Signal definition	Description
GND	Ground
$\mathbf{V_{dd}}$	Positive actuation bias voltage
$\mathbf{V_{ss}}$	Negative actuation bias voltage
$\mathbf{V_m}$	Positive modulation voltage
$\mathbf{-V_m}$	Negative modulation voltage
$\mathbf{V_{s-}}$	Negative output signal of the single-axis accelerometer
$\mathbf{V_{s+}}$	Positive output signal of the single-axis accelerometer
$\mathbf{V_{s-,\,x}}$	Negative output signal of the inner accelerometer in the dual-axis accelerometer
$\mathbf{V_{s+,\,x}}$	Positive output signal of the inner accelerometer in the dual-axis accelerometer
$\mathbf{V_{s-,\,y}}$	Negative output signal of the outer accelerometer in the dual-axis accelerometer
$\mathbf{V_{s+,\,y}}$	Positive output signal of the outer accelerometer in the

	dual-axis accelerometer
$\mathbf{V_{a,\,x}}$	AC actuation voltage (3V) for the single-axis accelerometer and the inner accelerometer in the dual-axis accelerometer
$\mathbf{V_{a,\,y}}$	AC actuation voltage (3V) for the outer accelerometer in the dual-axis accelerometer

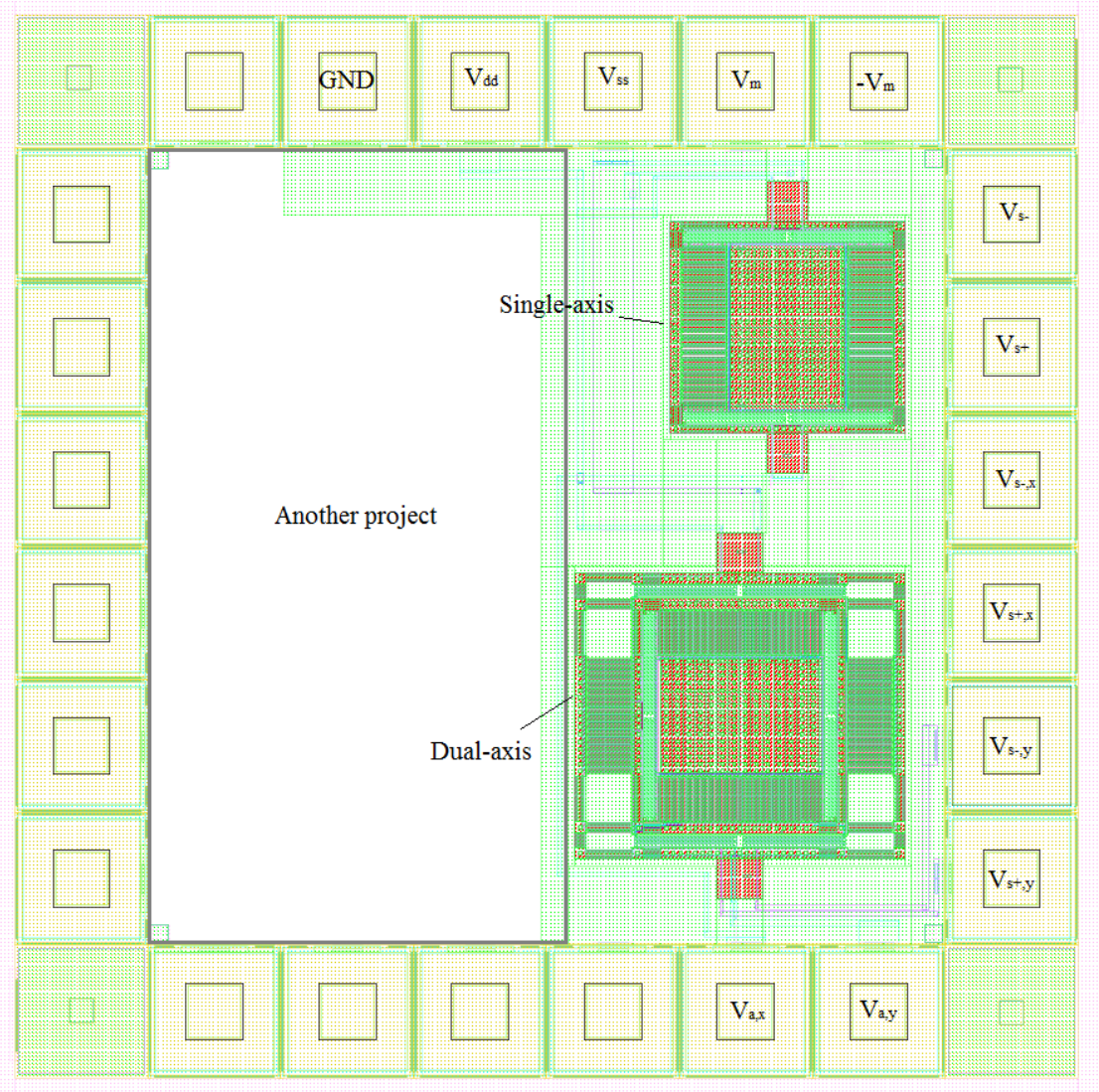

Figure 8.1: Layout of the experimental chip in Cadence

8.3 Proposed improvement of the designs

In this section, some suggestions are given to improve the designed systems in this thesis. Many details on the STM 0.25μm BiCMOS process are inadequate, and hence the material properties used for the calculation and the simulation are obtained through CoventorWare. The obtained results could not be desirably accurate compared to the

measured results. The multilayer structures can affect the actual performances of the systems.

The designed single-axis and dual-axis lateral capacitive accelerometers will be fabricated using the CMOS-MEMS process described in chapter 2. The post-CMOS process used is also referred to as a frond-side dry etching with CMOS metal mask. Another post processing method could be used in to make thicker structures. That is the maskless post CMOS-process with backside etch described in section 2.3.2. The additional layers (Silicon layer) can make the microstructures thicker so that they can benefit for the capacitive accelerometers. For example, the proof mass can be increased; the sidewall, overlapping capacitance of the comb fingers is increased, but average Young's modulus is also increased which does not benefit the springs. This processing approach has to be researched further.

Due to the CMOS-MEMS process used in this thesis, the main challenge with thin film multilayer structures is the lateral and out-of-plane curl. The tapered beams can be built to reduce lateral curl, but more analyses have to be made and a new value of the sensing capacitance could be obtained. In order to reduce out-of-plane curl, the comb fingers are compensated with a rigid frame surrounding the accelerometers. The compensation frame requires a closer analysis on the curling gradient and the overall overlapping capacitance. The curling effects could influence the performances of the serpentine springs and more analyses are necessary.

One of the benefits with multilayer structures is that the full differential capacitive topology can be implemented in the capacitive accelerometers. The systems in this thesis use a symmetry topology described in section 5.1. The symmetry topology has the advantage of minimizing the parasitic capacitance within the structures and is simple to be implemented in the layout. In some state-of-the-art capacitive accelerometers [17][18], another full differential capacitive topology referred to as common-centroid topology is used. It has better (higher) common-mode reject ratio (CMRR) and larger dynamic range [18], but higher parasitic capacitance. This topology is more complex than the symmetry topology in the implementation. More researches on this topology and the method of measuring the output signals are interesting for further studies.

For design B which is completely based on modification of the design A, a larger proof mass can be made for the design A. In that way, a genuine improved capacitive accelerometer can be produced according to the design B.

For the dual-axis in-plane capacitive accelerometer, the influences between the inner and outer accelerometers can be minimized by spring design. Another solution depends on comb finger design that requires more researches. I have not figured out how to design the comb finger according to minimize the influences.

Chapter 9

Conclusion

A single-axis lateral capacitive accelerometer (design A) and a dual-axis in-plane capacitive accelerometer based CMOS-MEMS technology have been made. An alternative design (design B) based on the modification of design A is also analyzed. The system designs are emphasized on the mechanical structure design and capacitive sensing. Self-test actuators based on electrostatic actuation mechanism are built to both the single-axis and dual-axis capacitive accelerometers. The design parameters are obtained through mathematical analysis in MatLab and 3D FEM simulation in CoventorWare. The achieved results are used to calculate the mechanical sensitivity and the sensor sensitivity according to equation (3.3) and equation (5.9) respectively.

The sensor sensitivity of the single-axis accelerometer is found to be 9.3mV/G by modulation voltage of 1.5V and the mechanical noise floor is $19\mu G/\sqrt{Hz}$. The linear range of the sensor sensitivity is defined as $\pm$26G. A summary of the achieved results can be found in chapter 8. The dual-axis accelerometer has a sensor sensitivity of 9.3mV/G in one direction and 11.1mV/G in the cross direction. No measurement results can be obtained at present and only calculated and simulated results can be shown for the main features of the accelerometers.

By using the CMOS-MEMS process, the accelerometers with high sensitivity and low input voltage requirement are made. The devices with the achieved results are basically compatible with the sensor node in a wireless sensor network described in chapter 1.

9.1 Future work

The suggestion of using another CMOS-MEMS process with backside etch is mentioned in chapter 8, which benefits to make capacitive accelerometers. However, this kind of post processing method requires higher cost.

The designed capacitive accelerometers in this thesis have the movement detection in x-direction and y-direction. The capacitive accelerometer can also be operated in z-direction (vertical movement). The spring design and the capacitance analysis should be carried out in another way. For example, the spring constant in z-direction has to be obtained as small as possible; the overlapping capacitance between the comb fingers is based on area tuning of a capacitor. By integrating the accelerometers in 3 sensing directions, a 3-axis capacitive accelerometer can be constructed.

A CMOS circuitry can be made to enhance the accelerometers performance with respect to make a real monolithic integrated system on the same chip (SoC) which has characteristics of decreasing the overall parasitic capacitance. For measuring the extreme small capacitance, a sensing el. circuit has to be made before enhancing the performance. Differential amplifiers, low-pass filters, and comparators, even a feedback loop circuit are the typical electronic components in enhancing the sensor performances.

Appendix A

STM SiGe 0.25μm BiCMOS (BiCMOS7RF) process defined in CoventorWare

Number	Step Name	Layer Name	Material Name	Thickness	Mask Name	Photoresist	Depth	Mask Offset	Sidewall Angle	Comments
0	Substrate	Substrate	SILICON	5	GND					
1	Stack Material	dielectric	OXIDE	0.3						
2	Stack Material	Scrafice	BPSG	50						
3	Conformal Shell	poly	POLYSILICON	0.6						
4	Straight Cut				poly	+		0	0	
5	Conformal Shell	viaPoly	OXIDE	0.6						
6	Straight Cut				viaPoly	+		0	0	
7	Conformal Shell	metal1	TUNGSTEN	0.6						
8	Straight Cut				met1	+		0	0	
9	Conformal Shell	via1	OXIDE	0.6						
10	Straight Cut				viaPoly	+		0	0	
11	Conformal Shell	metal2	ALUMINUM	0.6						
12	Straight Cut				met2	+		0	0	
13	Conformal Shell	via2	OXIDE	0.6						
14	Straight Cut				via2	+		0	0	
15	Conformal Shell	metal3	ALUMINUM	0.6						
16	Straight Cut				met2	+		0	0	
17	Conformal Shell	via3	OXIDE	0.6						
18	Straight Cut				via2	+		0	0	
19	Conformal Shell	metal4	ALUMINUM	0.6						
20	Straight Cut				met2	+		0	0	
21	Scrafice		BPSG							

Cross section of the multilayer structure after the process

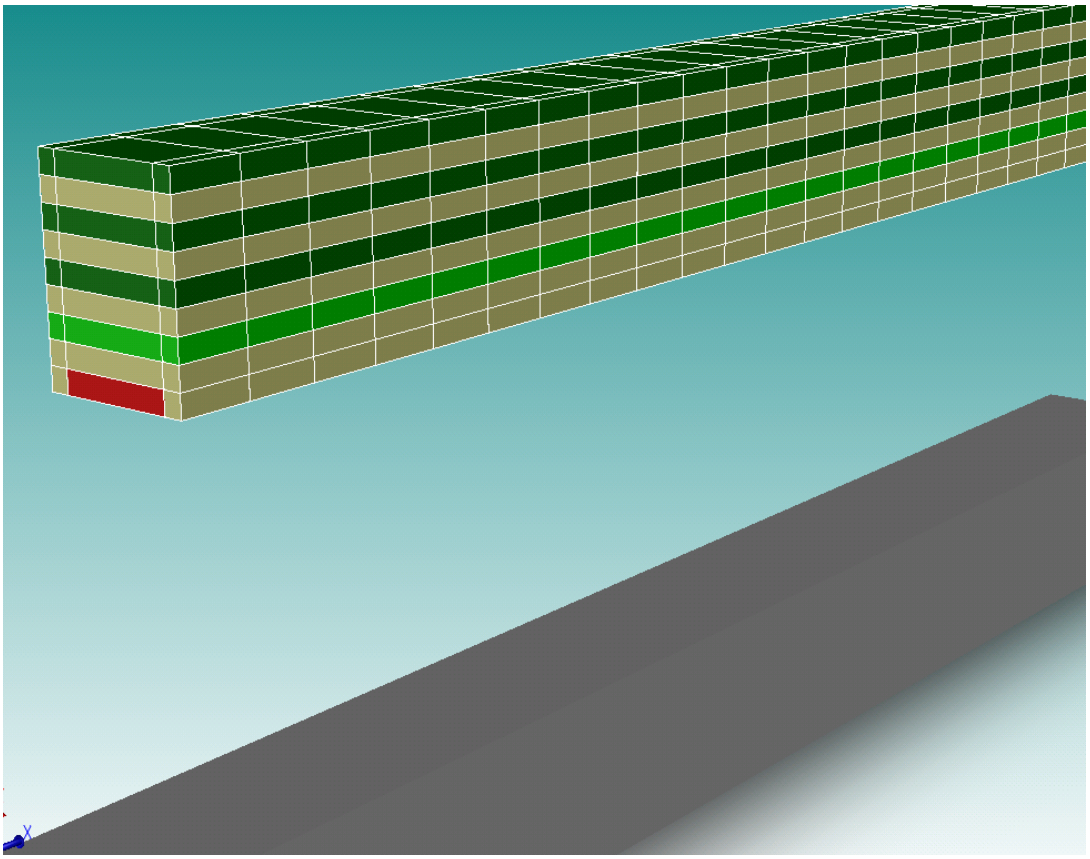

List of Figures

List of Tables

Bibliography

[1] Stephen D. Senturia, "Microsystem Design", Kluwer Academic Publishers, 2001.

[2] A second view of the mite approaching the gear chain, Sandia National Laboratories, <http://mems.sandia.gov/gallery/images_bugs_on_mems.html>, 2008

[3] Gary K. Fedder, “CMOS-based sensors”, *Pro. IEEE,* 2005

[4] O. Soeraasen and J. Ramstad, “From MEMS devices to smart integrated systems,” in Journal of Microsystem Technologies, vol. 14, pp. 895–901, Springer Verlag, 2008.

[5] Hongwei Qu, “Development of DRIE CMOS-MEMS process and integrated accelerometers”, Ph.D. thesis, University of Florida, 2006

[6] T.-H. Lin, W. J. Kaiser, and G. J. Pottie, "Integrated low-power communication system design for wireless sensor networks," *IEEE Communications Magazine*, vol. 42, no. 12, pp. 142-150, 2004.

[7] Wireless sensor network, Wikipedia <http://en.wikipedia.org/wiki/Wireless_sensor_network>, 2007

[8] David Culler, Deborah Estrin, Mani Srivastava, “Overview of Sensor Networks”, *IEEE Computer Society*, pp. 41-49, Aug 2004.

[9] Kay Römer, Friedemann Mattern, “The Design Space of Wireless Sensor Networks”, *IEEE Wireless Communications*, Dec. 2004

[10] J. Ramstad, K. Kjelgaard, B. Nordboe, and O. Soeraasen, “Rf mems front-end resonator, filters, varactors and a switch using a cmos-mems process,” in DTIP of MEMS and MOEMS, pp. 170–175, April 2009.

[11] Nadim Maluf and Kirt Williams, “An Introduction to MicroElectroMechanical Systems Engineering, second edition”, Boston, Artech House, 2004.

[12] O.Brand, G.K.Fedder, ”CMOS - MEMS”, Advanced Micro & Nanosystems, vol. 2, Weinheim, Wiley-VCH. 2004

[13]J. M. Bustillo, R. T. Howe, R. S. Muller, “Surface micromachining for microelectro- mechanical systems.” Proc. IEEE, 1998, 86, 1552-1574.

[14]T.A. Core, W.K. Tsang, S.J. Sherman, “Fabrication technology for an integrated surface micromachined sensor.” Solid State Technol. 1993, 39-47.

[15]Soumik Ghosh and Magdy Bayoumi, “On Integrated CMOS-MEMS System-on-Chip”, IEEE-NEWCAS Conference, 2005

[16]G. Fedder, S. Santhanam, M. Reed, S. Eagle, D. Guillou, M. Lu, and L. Carley, “Laminated high-aspect-ratio microstructures in a conventional CMOS process,” in Proceedings of the IEEE Micro Electro Mechanical Systems Workshop, pp. 13–18, February 1996.

[17]H. Luo, et. al., “A 1 mG Lateral CMOS-MEMS Accelerometer,” IEEE MEMS ‘00, Japan.

[18]Hao Luo, Gang Zhang, L. Richard Carley, Fellow, IEEE, Gary. K. Fedder, “A post-CMOS micromachined lateral accelerometer”, pro. IEEE, 2002

[19]A. P. Pisano and Y. H. Cho, “Mechanical design issues in laterally-driven microstructures,” In Technical Digest, 5th Inter. Conf. on Solid-State Sensors and Actuators (Transducers ’89), Montreux, Switzerland, June 1989, pp. 1060-1064.

[20]M. W. Judy, ”Micromechanisms using sidewall beams,” PhD thesis, Dept. of Electrical Engineering and Computer Sciences, University of California at Berkeley, May 1994.

[21]Gary Keith Fedder, “Simulation of MicroElectroMechanical Systems,” Ph.D. Thesis, UC Berkeley, 1994.

[22]W. Young and R. Budynas, ”Roark’s Formulas for Stress and Strain,” 7th ed. McGraw-Hill, 2002

[23]Ville Kaajakari, “*Practical MEMS”*, Louisiana Tech University, Small Gear Publishing, 2009

[24]Mark Lemkin, Bernhard E. Boser, “A Three-Axis Micromachined Accelerometer with a CMOS Position-Sense Interface and Digital Offset-Trim Electronics”, IEEE Journal of solid-state circuits, vol. 34, no. 4, April 1999

[25]W. Kuehnel, "Modeling of the mechanical behavior of a differential capacitor acceleration sensor," *Sensors and Actuators A: Physical*, vol. 48, 1995, pp. 101-108.

[26] Boser B.E., Howe R.T., ”Surface Micromachined Accelerometers”, IEEE Custom Integrated Circuits Conference, 1995. Pp. 337-344.

[27] Nordbø, Bård Eirik, “Two lateral RF MEMS varactors and an experimental switch made using a CMOS-MEMS process”, Master thesis, University of Oslo, 2009

[28] H. Xie, G.K. Fedder, ”Vertical comb-finger capacitive actuation and sensing for CMOS-MEMS.” Sens. Actuators A 2002, 95, 212-221.

[29] Kjelgård, Kristian Gjertsen, “Out-of-plane CMOS-MEMS variable capacitor”, Master thesis, University of Oslo, 2009

[30] M.S-C.Lun, X.Zhu and G.K.Fedder, ”Mechanical Property Measurement of 0.5μm CMOS Microstructures,” in Proc. Of the Material Research Society (MRS) 1998 Spring Meeting, Symposium on MicroElectroMechanical Structures for Materials Research, San Francisco, CA, Apr. 13-17, 1998.

[31] Gang Zhang, Huikai Xie, Lauren E. de Rosset and Gary. K. Fedder, “A lateral capacitive accelerometer with structural curl compensation”, *Proceedings of The 12th IEEE International Conference on Micro Electro Mechanical Systems (MEMS '99)*, January, 1999, pp. 606 - 611.

[32] Gang Zhang, ”Design and simulation of a CMOS-MEMS accelerometer”, Project Report, Carnegie Mellon University, May, 1998

[33] V. Gupta and T. Mukherjee, “Layout synthesis of CMOS MEMS accelerometers,” *MSM 2000*, pages 150 – 153

[34] T. Lee, “The design of CMOS radio-frequency integrated circuit,” Cambridge university press, 1998.

[35] Sun C-M, Wang C-W and Fang W, “On the sensitivity improvement of CMOS capacitive accelerometer,” Sensors and Actuators A, 141, 2008, pages 347–352

[36] C-L Dai, ”In situ electrostatic microactuators for measuring the Young’s modulus of CMOS thin films,” J. Micromech. Microeng., v. 13. No.5.2003.pp.563-7.

[37] O. Paul, D. Westberg, M.Hornung, V. Ziebart, H. Baltes, ”Sacrificial aluminum etching for CMOS microstructures,” In: Proc. IEEE MEMS ’97; 1997, pp. 523-528

[38] O. Paul, H. Baltes, Sens. Actuat. A 46 (1995) 143–146.

[39] D. Westberg, O. Paul, G.I. Andersson, H. Batles, Sens. Actuat. A 73 (1999)

243–251.

[40]T-mote sky datasheet, Moteiv Corporations, <http://www.snm.ethz.ch/pub/uploads/Projects/tmote_sky_datasheet.pdf >,2006

[41]“Smart Dust”, UH ISRC Technology Briefing, <http://www.uhisrc.com/FTB/Smart%20Dust/Smart%20Dust.pdf> March 2005

[42]C.-L. Dai and M.-C. Liu, “A wet etching post-process for CMOS-MEMS RF switches,” in 2nd IEEE International Conference on Nano/Micro Engineered and Molecular Systems, pp. 968–971, January 2007.

[43]Ching-Liang Dai, “A maskless wet etching silicon dioxide post-CMOS process and its application,” Microelectronic Engineering 83 (2006) 2543–2550

[44]Huikai Xie, Lars Erdmann, Xu Zhu, Kaigham J. Gabriel and Gary K. Fedder, “Post-CMOS processing for High-aspect-ratio integrated silicon microstructures,” Journal of MicroElectroMechanical systems, Vol. 11 No.2 Apr. 2002.

[45]Gary K. Fedder, ”CMOS MEMS Co-design,” Lecture at IMEC, Dec. 8-9 2008

[46]B. E. Boser, "Surface Micromachining–An IC-Compatible Sensor Technology," HOTCHIPS-VIII, Stanford, CA, 1996, pp.

[47]P. W. Barth, F. Pourahmadi, R. Mayer, J. Poydock, and K. Petersen, "A monolithic silicon accelerometer with integral air damping and overrange protection," IEEESolid-State Sensor and Actuator Workshop 1988, Hilton Head Island, SC, 1988, pp. 35-38.

[48]D. L. DeVoe and A. P. Pisano, "Surface micromachined piezoelectric accelerometers (PiXLs)," *Journal of Microelectromechanical System*, vol. 10, 2001, pp. 180-186.

[49]Amy Wung, “CMOS-MEMS High Gee Capacitive Accelerometers,” Master of science in Electrical and Computer Engineering at Carnegie Mellon University, December 23, 2007